2023

Optimal Sizing and Safe Management of Lithium-Ion Batteries in High Voltage Power Systems

Hayden Lee Atchison

OPTIMAL SIZING AND SAFE MANAGEMENT
OF LITHIUM-ION BATTERIES IN HIGH
VOLTAGE POWER SYSTEMS

by

HAYDEN ATCHISON

DISSERTATION

Submitted in Partial Fulfillment of the
Requirements for the degree of Doctor of
Philosophy at The University of Texas at Arlington

August, 2023

Arlington, Texas

Supervising Committee:

David Wetz, Committee Chair

Rasool Kenarangui

Wei-Jen Lee

DEDICATION

I dedicate this work to my father, Brian Atchison, who supported me through my education but was not able to see me graduate.

ACKNOWLEDGMENTS

ABSTRACT

OPTIMAL SIZING AND SAFE MANAGEMENT
OF LITHIUM-ION BATTERIES IN HIGH
VOLTAGE POWER SYSTEMS

Hayden Atchison, Ph.D.

The University of Texas at Arlington, 2023

Supervising Professor: David Wetz

Lithium-ion batteries have gained widespread use in various applications, but safety challenges persist due to errors in assembly and faulty electronics management. Ensuring safety and reliable operation in large batteries containing numerous series/parallel cells demand innovative monitoring technologies. Elevated temperatures resulting from normal or abnormal operation are a major cause of battery failure, necessitating effective temperature monitoring techniques. Similarly, abnormal stress/strain signatures offer valuable diagnostic information. In the study discussed here, the application of a Optical Distributed Sensor Interrogator (ODiSI) employing high-definition fiber optic sensors (HD-FOS) for measuring surface temperature and case deformation of 18650 cells under normal and abnormal conditions, respectively, has been shown. The FOS replaces multiple discrete thermocouples or strain gauges and provides measurements with millimeter resolution along the fiber length, ensuring early detection and identification of abnormal cell operation on individual cells assembled within large batteries. The unique and repeatable results this measurement delivers for effective lithium-ion cell monitoring has been demonstrated through the development and employment of a novel data acquisition system that is interfaced with the ODiSI and a system level controller.

In addition to the sensor work performed, this report documents the design and implementation of a novel battery sizing tool developed in the MATLAB programming

environment. As power demands grow in civilian and defense applications, intelligent power system architectures with properly sized energy storage becomes critical. Sizing energy storage accurately is challenging due to impedance and capacity variations under different operating conditions. To address this, the MATLAB-based energy storage sizing tool uses comprehensive databases derived from empirical data collected from various energy storage cells. This tool aids power system engineers in optimally sizing energy storage to meet voltage and load requirements, considering each cell's characteristics within the database.

Together, these studies present innovative approaches to address safety challenges, monitor individual cells, and properly size energy storage in lithium-ion batteries, offering promising solutions for safer and more reliable battery operation in diverse applications.

TABLE OF CONTENTS

LIST OF FIGURES

CHAPTER 1: INTRODUCTION

As described in the abstract, this dissertation discusses two overlapping topics related to the safe monitoring, operation, and sizing of energy storage technologies. A new monitoring technique employing a Luna Innovations Optical Distributed Sensor Interrogator (ODiSI) has been demonstrated using 18650 cells as they are cycled in normal and abnormal operating conditions. This work has been documented and published in three peer reviewed journal articles and those three papers have been employed as a dissertation substitute. They make up Chapters 2 through 4 of this dissertation. Each of the three paper describes the employment of a Luna ODiSI with a different lithium-ion battery configuration under different experimental conditions. The ODiSI utilizes high-definition fiber optic sensors (HD-FOS) to measure surface temperature or strain, but not both simultaneously. The results have shown the ability of the ODiSI to measure the temperature or strain on individual cells as well as on individual cells assembled within an array of cells assembled with potentials as high as 1000 VDC. A custom data acquisition system has been designed to interface between the ODiSI, the battery management system (BMS), and the overarching system level controller. The Luna ODiSI is an expensive measurement device that may not be viable for employment in all battery applications but there are countless applications where it does make sense and it can offer benefits not obtainable any other way. The aim of this work is to provide the energy storage community with a new approach for measuring and monitoring cells assembled within large battery configurations.

In addition to documentation of the novel monitoring of lithium-ion temperature and strain, this dissertation presents a new MATLAB-based energy storage sizing tool that has been designed to optimize the parallel/series combination of batteries being constructed for use in elevated power applications. Though batteries are employed in countless applications every day, most of them are

employed at low to moderate power rates, largely because operation at higher rates induces undesirable accelerated aging. In limited instances, accelerated aging is acceptable because the battery must supply high power in as small a package as possible. Though battery aging is not considered here, the methods used to minimize the size of a battery supplying high power is. Because there is a lack of demand for employing batteries under high continuous loading conditions, there is a lack of information available on manufacturer data sheets that battery designs can use to safely size a battery using the minimum number of cells. The UTA Pulsed Power & Energy Laboratory (PPEL) has a long history of studying energy storage at high elevated rates and the broad database collected from many different cells over the years has been employed here to build a sizing tool that can be used to size a battery against the user's load profile. The tool considers the user's power, operation time, weight, and volume, among other properties. A data import tool has also been developed such that a user can seamlessly expand the database as to include additional cells of interest. While energy storage sizing tools exist, none are documented that use empirically collected data in a MATLAB software environment. The design of both the data import tool and the sizing tool are discussed in Chapter 5. This one-of-a-kind tool is being widely employed by many PPEL customers and it is presently being expanded in support of a few different ongoing funded research grants.

CHAPTER 2: FIBER OPTIC BASED THERMAL AND STRAIN SENSING OF LITHIUM-ION BATTERIES AT THE INDIVIDUAL CELL LEVEL

2.1 MANUSCRIPT 1: BACKGROUND

The rapid proliferation of lithium-ion batteries since their inception in the 1980s has revolutionized energy storage across a broad spectrum of civilian and military applications. These batteries have offered extended lifetimes, superior energy and power densities, and reduced environmental footprints, thereby becoming integral to modern life. However, the surge in their use has raised concerns about their safety, primarily rooted in occasional errors during assembly and electronic management, sparking public awareness and apprehension. A particular challenge lies in the comprehensive monitoring of individual cells within large operational batteries composed of numerous series and parallel cells. This intricacy has underscored the demand for novel, non-invasive sensing technologies to alleviate these safety uncertainties. Of these concerns, elevated temperatures due to normal and abnormal operation emerge as a leading cause of failure. Conventional thermal sensing technologies permit monitoring at a few localized spots within a vast battery setup, leading to potential lapses in temperature measurement and inadequate protection against hazards. Additionally, the expansion and contraction of a cell's casing during abnormal conditions offer a detectable stress/strain signature that holds diagnostic potential. Addressing these challenges, this manuscript explores the capabilities of an Optical Distributed Sensor Interrogator (ODiSI) in gauging the surface temperature and case deformation of 18650 lithium-ion cells under normal and abnormal operating conditions. A series of experiments underscore the unique and repeatable results achieved by ODiSI, offering promising avenues for enhanced monitoring of lithium-ion cells, thus contributing to safer battery technologies.

2.1.1 MODIFICATIONS TO MANUSCRIPT FOR INCLUSION IN DISSERTATION

2.2 ABSTRACT

A few safety challenges with lithium-ion batteries, stemming mostly from errors in assembly or from faulty electronics managing them, have created visibility and public concern. The ability to monitor all individual cells within large operational batteries containing many series/parallel cells, respectively, is challenging, and there is growing demand to identify new, non-invasive sensing technologies. Elevated temperatures, induced by either normal or abnormal operation, is a leading cause of failure. With traditional thermal sensing technology, it's feasible to monitor a few spots within a large battery, introducing a high probability that elevated temperatures will not be measured by the management system(s) intended to protect them. When abnormal conditions occur, a cell's case expands and contracts in a measurable way. Detection of an abnormal stress/strain signature is another diagnostic that has great potential. The present study demonstrates the ability of an Optical Distributed Sensor Interrogator (ODiSI) to measure the

surface temperature and case deformation of 18650 cells under normal and abnormal conditions, respectively. Multiple experiments have been performed to demonstrate the abilities of the ODiSI to measure temperature and stress/strain changes, respectively, and they show that the results are unique and repeatable making this a promising technique for monitoring lithium-ion cells.

Keywords: lithium-ion battery; high density fiber optic sensor; strain; temperature

2.3 INTRODUCTION

The advent of lithium-ion batteries in the 1980s created a disruptive technology that infiltrated the battery marketplace and now they account for a significant fraction of the energy storage devices used in civilian and military applications today. Although this battery technology promises extended lifetime, higher specific energy and power, and less environmental impact, there is still a concern over the safe application of this technology [1, 2]. The impact these devices have on everyday life requires that these batteries be continuously monitored for safety in the areas of thermal stress or mechanical strain, respectively, induced by overuse, over-charge, or over-discharge. Traditional techniques use thermocouples for the measurement of temperature and strain gauges for the measurement of strain; however, these traditional measurement devices can be limited by the environment where they are deployed or only acquire measurements at a single location of deployment [3]. In large batteries where there are a high number of cells assembled in series and/or parallel, a few of these single point measurements are not enough to always ensure safe operation. Therefore, it is imperative that alternative interrogative techniques be developed and employed to monitor a change in temperature and strain throughout these battery technologies to maintain proper safety protocols.

Recent advances have led to the introduction of fiber optic sensing to replace the traditional methods of temperature and strain measurement. High Definition – Fiber Optic Sensing (HD-FOS) uses Optical Frequency Domain Reflectometry (OFDR) to make very high-resolution strain or temperature measurements within an optical fiber. OFDR employs swept laser interferometry to produce these measurements vs. sensor length using Rayleigh scatter as the source signal [4]. The change in the Rayleigh signal from the fiber's reference state can then be correlated to either a change in temperature or a change in strain, but not at the same time, presently [5]. The benefit of this technique is that the optical fiber is typically a standard, relatively inexpensive telecom-grade fiber [6]. It is lightweight and small allowing for deployment in a wide range of applications, it is immune to electromagnetic interference (EMI), and it is electrically insulated. The inherent nature of the fiber optic cable allows for it to be either short, < 1 m, or longer in length, up to 50 m, making it very versatile. The maximum data acquisition rate, as high as 250 Hz, and the distance between discrete measurements, less than 1 mm, is dependent upon the length of the fiber [5]. A single dielectrically insulated fiber can replace thousands of thermocouples using a single channel data acquisition system, dramatically simplifying thermal measurement and increasing safety monitoring.

In this study, a Luna HD-FOS coupled with an ODiSI data acquisition system has been used to measure the surface temperature of single 18650 lithium-ion cells when they are operated normally as well as when they are short circuited and over-charged in a controlled manner. The temperature measured by the HD-FOS has been verified against thermocouple data measured simultaneously. In addition to surface temperature, the strain deformation induced in the same type of 18650 lithium-ion cell has been measured when they are over-charged and short circuited in the same controlled way. Techniques were developed to measure the cylindrical case strain along the

6

axial length of the cell during abnormal events, and the strain measurements obtained by the HD-FOS were compared to strain measurements made using a laser interferometer to verify the efficacy of this interrogation technique. The HD-FOS technology, the fiber integration onto 18650 cells, the experimental procedures developed, and the results obtained at the cell level in each type of experiment will be documented here.

2.3.1 HD-FOS SENSING TECHNOLOGY

HD-FOS is achieved using OFDR which allows thousands of sensing points with overlapping spectra in a single optical fiber to be read with sub-millimeter spatial resolution [7]. When interrogated by a laser light source, the Rayleigh backscatter of an optical fiber produces a random and stable spectral pattern, unique to each specific fiber, which is then recorded by the instrument. Just as with a fiber Bragg grating (FBG), applied temperature or strain causes shifts in the reflected spectrum of the scatter in the fiber at the location it is applied. Finding the frequency shift of the scatter spectrum is accomplished by performing a cross-correlation of the scatter spectrum from a measurement data set with that from a reference data set taken with the same fiber sensor in a known, nominal temperature or strain state. The correlation peak is shifted from center by a frequency shift resulting from either a change in strain or temperature [8].

The frequency shift of the Rayleigh pattern under applied strain, as compared to the reference state, is found at every point along the length of the fiber. Distributed measurements of strain are made by first determining a gage length, which is typically on the order of a millimeter but can be larger or smaller. The average spectral shift for each gage length is determined. This shift is then converted to measured strain using known calibration coefficients appropriate to the fiber type. Using this procedure, temperature, or strain, respectively, as a function of distance, can

be found along the entire length of the optical fiber. This technique has been successfully implemented for health monitoring for a variety of applications including composite wind turbine blades [9], and inflatable space habitats [10], among others.

2.4 PROCEDURE

Multiple experiments have been performed to measure both the change in temperature (dT/dt) and the change in strain (dS/dt) of individual 18650 cells. As mentioned earlier, the sensor technology is not able to measure temperature and strain simultaneously, so experiments have been performed in which each is measured independently under similar experimental conditions. A series of normal, short circuit, and over-charge experiments were performed to display and verify the repeatability of the measurements.

2.4.1 THERMAL AND/OR STRAIN CALIBRATION OF THE HD-FOS

Sensors are calibrated by the manufacturer, Luna Innovations, prior to shipping and a data key is provided with the sensor that is used by the ODiSI for correct scaling of the data. UT Arlington's Pulsed Power and Energy Laboratory (PPEL) is collaborating with Luna on this project and the information provided here on calibration is provided by them. The fiber sensors are made using Corning SMF-28 fiber and the strain is calibrated using the setup shown in Figure 2.1. For each spool of fiber, they use this setup to obtain calibration coefficients for the first and last few meters of fiber on the spool, respectively. They have found that by measuring these sections of each spool, the coefficients they obtain are representative for the spool's full length of fiber. The calibration device is housed in a temperature-controlled aluminum box which allows for decoupling of the strain and temperature measurements. Each end of the fiber is secured with a

clamp with one end held stationary while the other end is secured to a linear translational stage affixed to a rail with an adjustable micrometer actuator for adjusting the tension within the fiber. The fiber is stepped through multiple linear displacements and the resulting strain is calculated using Equation (2.1):

$$\varepsilon = \frac{\Delta L}{L} \tag{2.1}$$

where ε is the strain, ΔL is the change in fiber length due to movement of the translational stage, and L is the fiber length between clamps prior to test.

In addition to measurement of fiber displacement, the resulting Rayleigh frequency shift is also recorded where the strain can then be related to this frequency shift using a least square fit quadratic equation given by Equation (2.2):

$$\varepsilon = \gamma_0 + \gamma_1 \Delta v + \gamma_2 \Delta v^2 \tag{2.2}$$

where γ_x are the strain gauge factors obtained from the least squares fit of the strain to the shift in frequency, and Δv is the Rayleigh frequency shift. Sampling, ΔL, was set as one full rotation of the micrometer dial and measurements were taken, after the fiber was pre-strained, ramping from low strain to high strain then returning to low strain. The calculated strain and recorded frequency shift at each measurement point were collected and used to calculate the strain gauge factors in Equation (2.2) which establishes the scaled calibration of the ODiSI device and the fiber under test. A sample of the shifted Rayleigh scatter spectra that is measured when a sensor is put under stress/strain or when it is heated up, respectively, is shown in Figure 2.1. A reminder that scatter is induced by both mechanical and thermal stress so decoupling of one is required for the accurate measurement of the other. In Figure 2.2, the delta is correlated to a temperature change, but a similar shift can be related to a change in strain if that is the measurement of interest. Figure 2.3

9

shows a sample of the software interface that is used to interpolate the measured data and create a calibration key for each location down the length of the fiber.
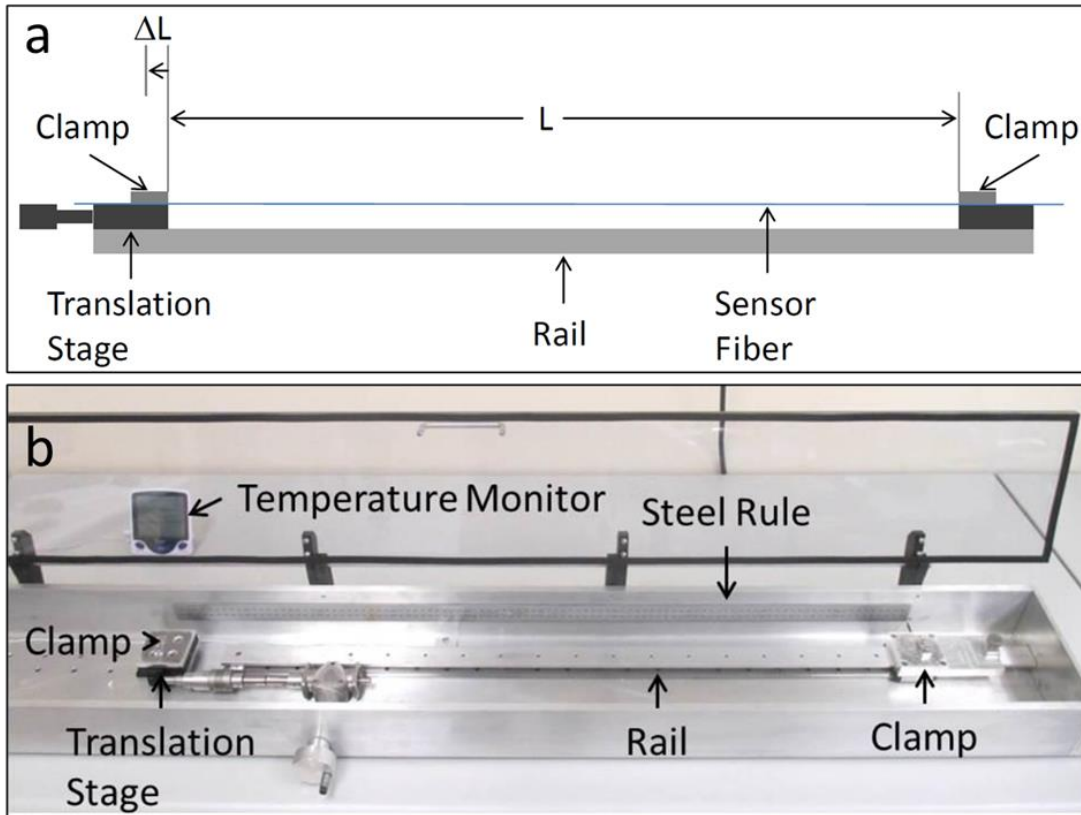
Figure 2.1. Calibration of a Fiber Sensor and ODiSI Unit for Strain Measurement Detection. A thermally-controlled aluminum case with a transparent lid was designed for calibration of a fiber sensor and ODiSI unit for strain measurement detection. (a) A schematic shows that the unit consisted of two clamps for positioning the fiber with one clamp held stationary and the other being adjustable through the use of a micrometer actuator attached to a translational stage. Measurements were made after the translational stage was moved one full revolution of the actuator. (b) The setup of the device shows that the unit is fully enclosed with an aluminum box and the temperature of the rail is monitored to ensure that the strain measurement is decoupled from temperature.
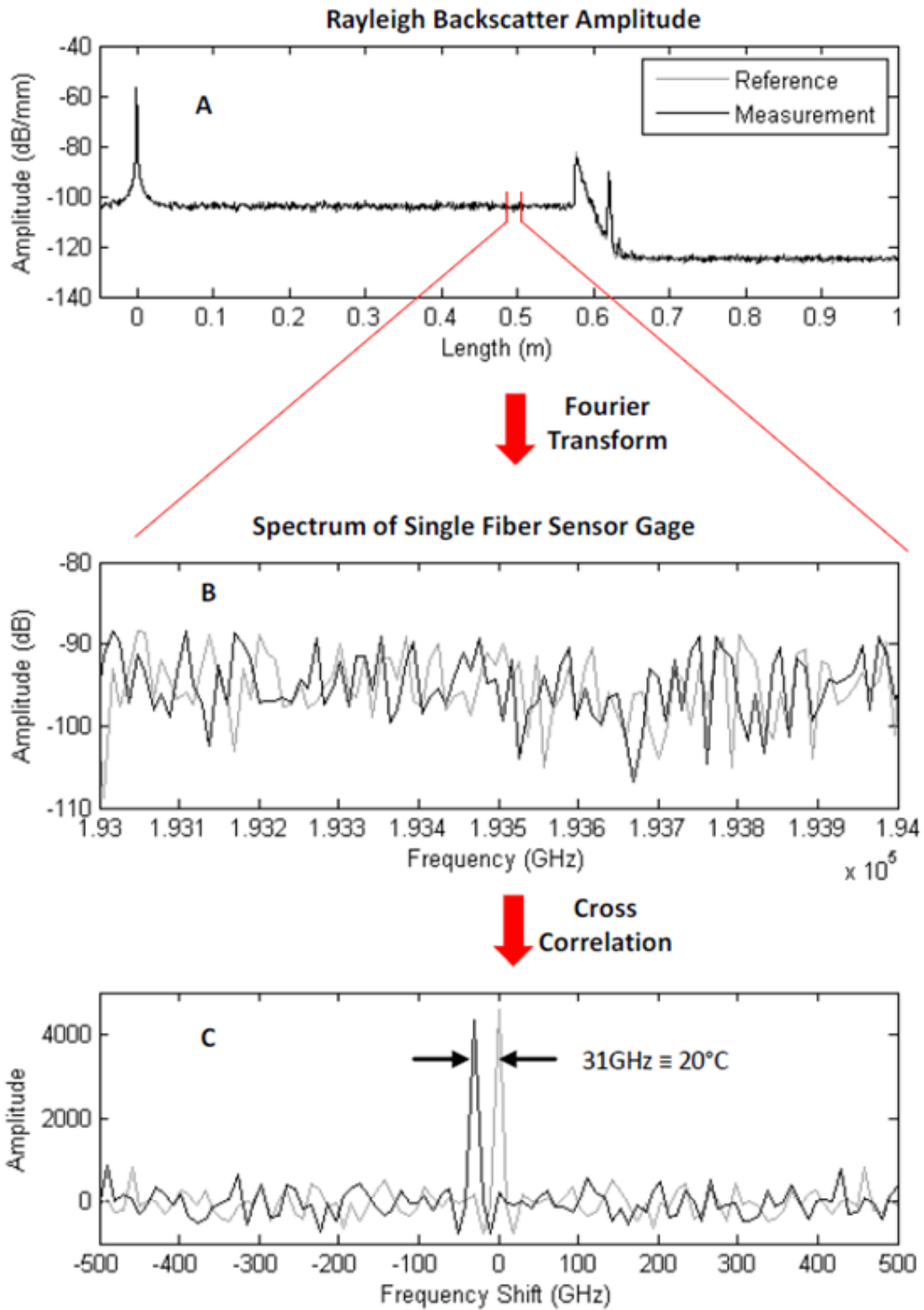
Figure 2.2. Rayleigh Scatter Spectra Measured Along Segment of Fiber. (a) Rayleigh backscatter along optical path. (b) Spectrum of single fiber sensor gage. (c) Cross correlation of reference and measurement spectra.

11
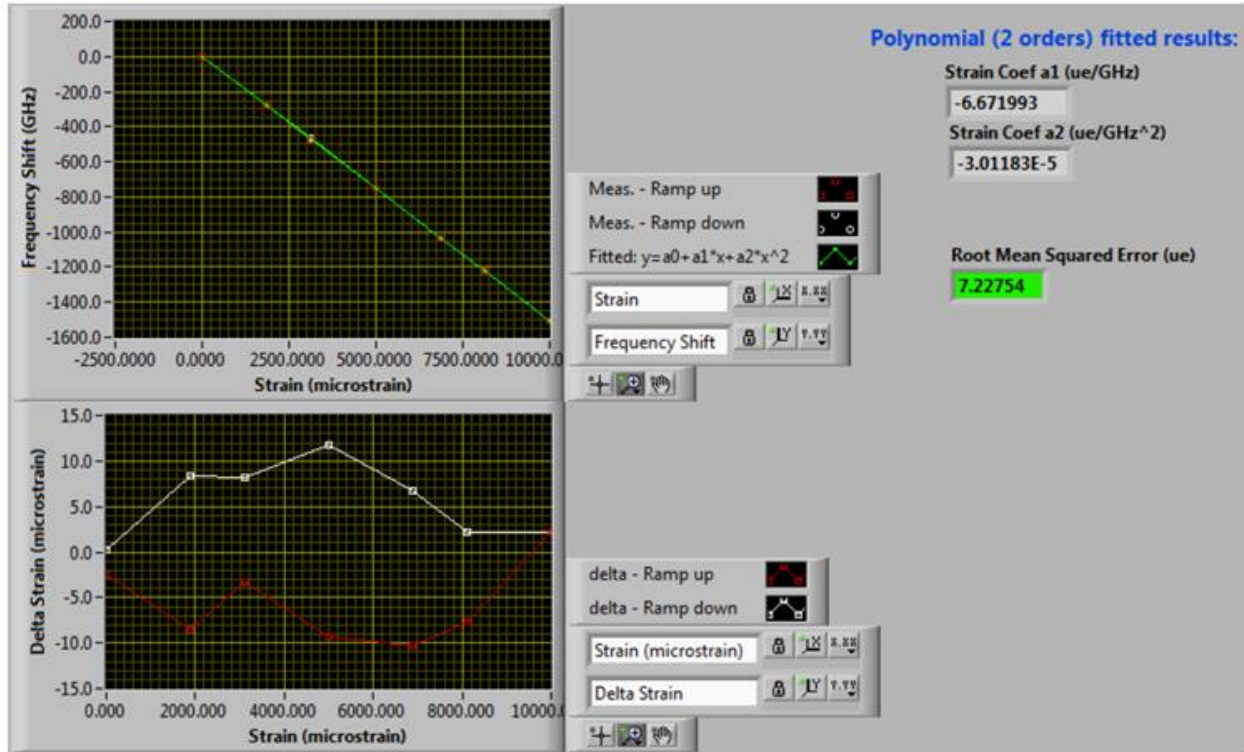
Figure 2.3. Calibration Tool Used to Create a Sensor Data Key. (a) Top graph is a least-squares fit to optical frequency shift vs. strain data and (b) Bottom graph shows the fit residuals that are typically ≤ 0.1% of the full strain range.

As with thermocouples, the coefficients used to relate the spectra shift to a change in temperature are based off repeatable, historical data collected using unique techniques at low, Figure 2.4, and high, Figure 2.5, temperatures, respectively. As seen in Figure 2.4, calibration from -40°C to 200°C is performed in an enclosure that is machined out of solid aluminum to house the optical fibers during temperature testing. The mass of the enclosure ensures that the temperature distribution within the enclosure cavity is uniform throughout the test and desiccant packs are used within the enclosure to limit humidity variation. Temperature uniformity within the enclosure cavity is verified in a pre-test with multiple fiber passes. Six calibrated platinum resistance temperature detectors (RTDs) are used as the temperature measurement standard against which

12

the fiber measurements are compared. The fiber is cycled through the -40°C to 200°C range at a ramp rate of 5°C per hour with 5-hour dwells at each respective temperature. Measurements of fiber frequency shift against RTD temperature were fit with both a linear and 4th order polynomial (quartic) fit using MATLAB's polyfit function, in order to obtain temperature coefficients for each fiber type.
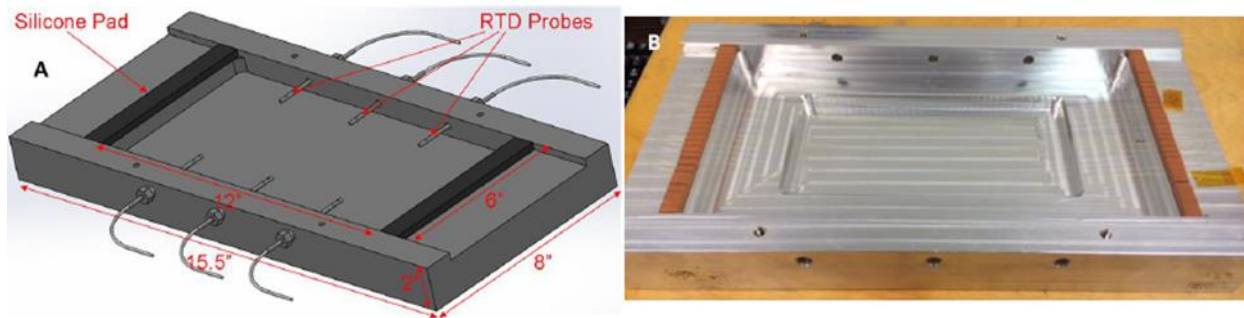
Figure 2.4. Aluminum Enclosure Used to Obtain Temperature Coefficients from -40°C to 200°C. (a) Aluminum enclosure. (b) Fiber layout within enclosure.

Calibration at temperatures higher than 200°C is accomplished using the setup in Figure 2.5 where the sensor is placed into a small box furnace capable of 1000°C. In addition to the fiber optic sensor, 4 K-Type thermocouples were placed at locations L = 0.34 m, 0.46 m, 0.52 m, and 0.59 m along the fiber. The furnace temperature was increased such that the sensors are held at a steady temperature and data was sampled repeatedly each day over a five-month period using Luna's Optical Backscatter Reflectometer (OBR) system. Measurements are post processed with a gage length of 0.5 cm and a sensor spacing of 0.1 cm. The fiber sensors are taken through a thermal cycle and compared to the K-Type thermocouple measurements and for each location, a

curve fit is obtained to relate the spectral shift to the applied temperature. The coefficients at each point are then averaged to provide a curve for the sensor.

Figure 2.5. Furnace And Experimental Setup for Determining High Temperature Coefficients.

2.4.2 THERMAL MEASUREMENT ON SINGLE CELLS USING A FOS

The first set of experiments were focused on measuring the thermal rise along the surface of a single 18650 cell during normal charge/discharge operation. Additionally, experiments were performed where cells were short circuited and over-charged, respectively, in a controlled manner. A single 18650 cell was instrumented using a 1 m long HD-FOS that was taped at each end axially

down the length of the cell. The tape creates a good thermal connection but a weak mechanical connection to the cell. The cell was cycled using a constant current charge (2.6 A)/discharge (5.2 A) profile and thermal measurements were made using the FOS taped to the surface and the ODiSI-B system, as seen in Figure 2.6.

Figure 2.6. Experimental Setup Showing the Fiber Optic Sensor Taped Axially Down the Length of the 18650 Cell Under Test. ODiSI-B System Not Shown.

Short circuit experiments were performed in which the temperature was identically measured down the length of an 18650 cell while it was being intentionally short circuited. The short circuit was made using a high current relay manufactured by Ross Engineering. When ready to begin the experiment, the relay was actuated closed and held closed for 30 seconds. In most cases, the cell's own current interrupt device (CID) actuated before the 30 second window was over. A DCT200-10B-24-S DC current transducer was used to measure the cell's short circuit current and a B&K Precision PR-60 differential voltage probe was used to measure the cell's voltage. An NI-9239 BNC voltage acquisition card was used at a sampling rate of 5 Hz to measure the voltage probe's output. A software algorithm was implemented using a National Instruments LabVIEW Virtual Instrument (VI) panel and the data was streamed into the VI from the ODiSI system. On the front panel, the user can manually input the starting location where the fiber first

contacts the cell and 60 temperature measurements are then taken beyond the initial location at discrete lengths of roughly 1 mm each. The algorithm measures the rate of temperature change, dT/dt, on the HD-FOS and when it exceeds a threshold for a required amount of time, both of which are adjustable by the user, then it sets a notification indicating that an abnormal short circuit event is occurring. Multiple experiments were performed to measure repeatability.

Over-charge experiments were performed in which the temperature was identically measured down the length of an 18650 cell while it was being intentionally over-charged. A 5 V power supply sources the cell's maximum charge current of 2.6 A to the cell under test. A 1 m HD-FOS was taped axially down the length of the cell, the same as it was in the normal operation and short circuit experiments, respectively, and the same B&K Precision PR-60 differential voltage probe was used to measure the cell's voltage. As was done with the short circuit experiments, an early detection algorithm was developed to detect the rapid rise in temperature, dT/dt, that occurs during this abnormal operating condition. As will be shown, the rate of temperature change measured during the over-charge is slightly different than that measured during short circuit so both algorithms can run in parallel to detect either form of abnormal operation. The cell under test was charged until the cells own current interrupt device (CID) engaged and multiple over-charge experiments were performed to measure repeatability.

2.4.3 STRAIN MEASUREMENT ON SINGLE CELLS USING A FOS

A second identical series of short circuit and over-charge experiments were performed, with the only difference being the way in which the fiber was affixed to the cell under test, to measure the stress/strain signature of the cylindrical cell's case under these abnormal conditions. Because a sharp thermal rise is induced during these events, the sensor must be thermally isolated.

This is achieved by encasing the sensor within a bead of hot glue applied axially down the side of the cell. This manually ties the sensor to the cell but keeps it from being in direct contact with the cell's outer wall. In the initial series of experiments, a signature was measured but the hot glue became too flimsy when heated. As will be shown in the results, JB Weld and Silicone bonding adhesives were evaluated in some of the short circuit experiments and the results will be shown. The other side of the cell had a different section of the same FOS taped directly to the cell's wall to measure the difference between the two different application methods simultaneously, shown in Figure 2.7 (a).

A laser interferometer (rangefinder) was used as validation of the case's deflection during the over-charge and short circuit conditions, respectively. The data collected from the rangefinder was compared against that measured by the FOS. Due to the sensitivity of this device, a stand was modeled and constructed using a 3D printer to fasten both the interferometer and 18650 cell during testing. This part of the experimental setup is shown in Figure 2.7 (b).

A LabVIEW virtual instrument (VI) was developed, shown in Figure 2.7 (c), to control timing for all the short-circuit and over-charge experiments, respectively. The short circuit experiment was automated by the VI using a pre-written recipe consisting of an initial 10 s rest followed by a 35 s short circuit and then concluded with a 45 s data recording period. In order for these results to be accurate, the introduction and release of the short circuit needed to be automated, which was done using a solid-state relay triggered by the VI that then sends a trigger to a larger Ross relay that initiates the short-circuit. This process was also used during the over-charge experiments to initiate and stop charging of the 18650 cells. During the overcharge, the VI was provided a recipe consisting of a 10 s initial rest and a 0.5C charge until CID engagement at which point the user must interact with the front panel of the VI to end the overcharge, and the test is

concluded with a 10 s rest. Multiple short-circuit and over-charge experiments were performed with each type of adhesive to measure repeatability.
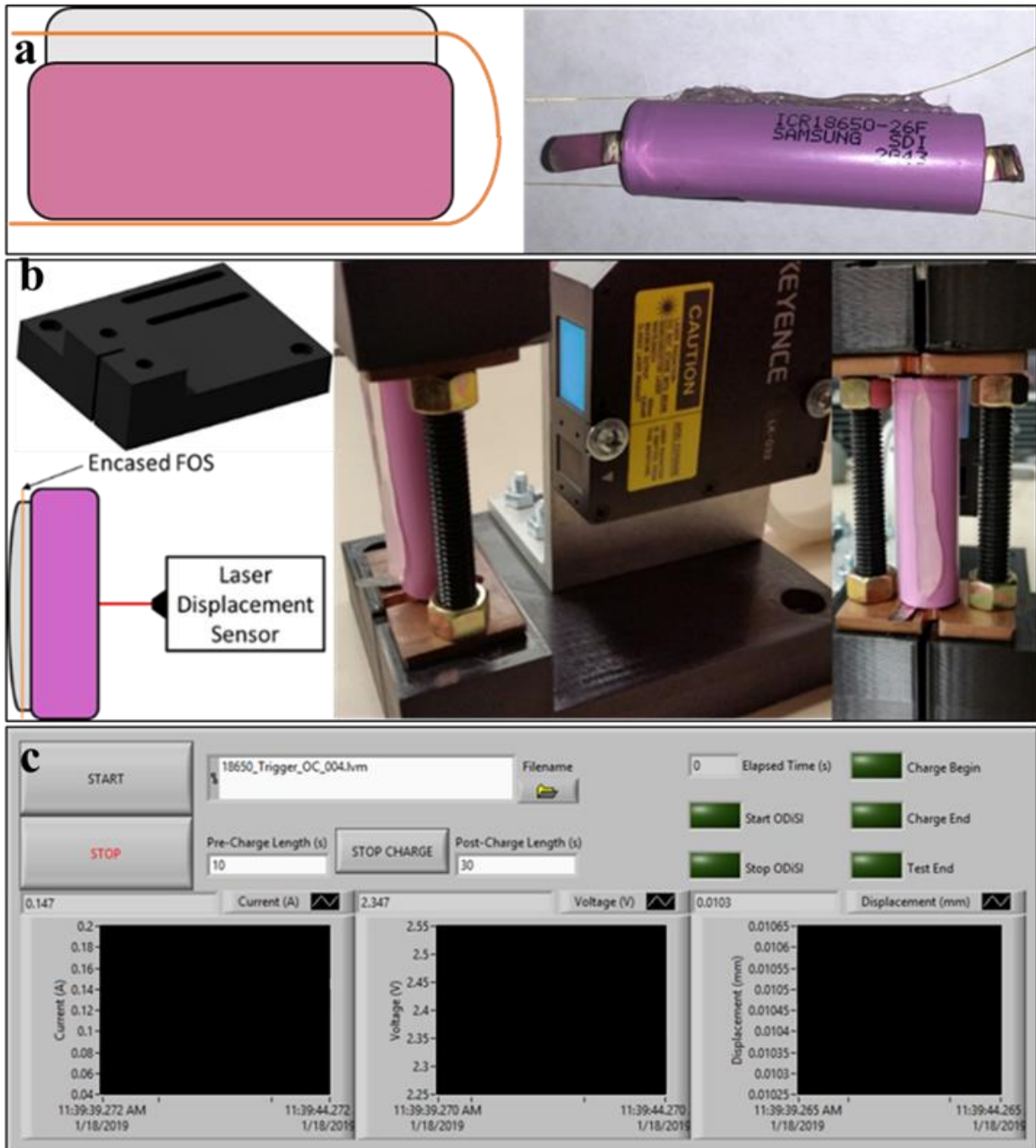
Figure 2.7. Experimental setup and control program used during short circuit and over-charge experiments. (a) FOS integration onto a single 18650 cell for strain analysis. The FOS was encased in hot glue on one side of the cell and then taped directly onto the cell on the

opposite side. This configuration was intended to decouple the strain and temperature measurement during a short circuit or over-charge experiment. (b) Stand designed to secure the laser rangefinder and 18650 cell. A slot was added to relieve strain and allow for a larger bend radius of the FOS. Additionally, mounting points were added to the stand to help with stability. (c) LabVIEW VI used for automated timing of short-circuit and over-charge testing. The parameters for the short-circuit and over-charge applications are nearly identical except for the configurable delays, such as the duration of the short-circuit and the time to wait before and after short/charge.

2.5 RESULTS AND DISCUSSION

2.5.1 THERMAL MEASUREMENT ON SINGLE CELLS USING A FOS

A single HD-FOS replaces multiple thermocouples and offers flexibility of taking temperature measurements with a resolution as small as 1 mm. Initially, an 18650 cell was instrumented with a single fiber taped axially along the cell body, shown earlier in Figure 2.6, and was then cycled at normal operating charge/discharge conditions. The results of this experiment, shown in Figure 2.8, indicate that a uniform increase in temperature is measured down the width of the cell and a maximum temperature of 53°C was measured at the end of each discharge step. During each 2.6 A charge, the temperature decreased from 53°C to a steady 26°C. The largest temperature change was calculated to be a maximum of 0.1°C/s during the 5.2 A discharge.
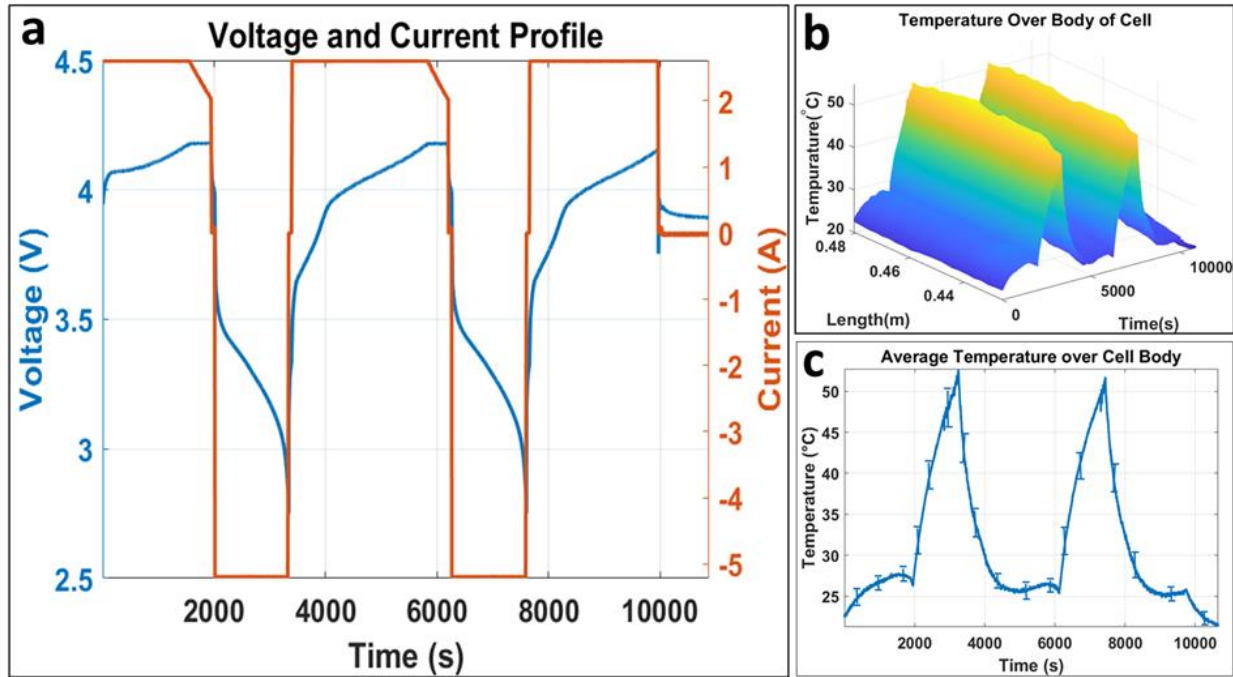
Figure 2.8. Thermal Sensing Using a FOS During Normal Operations. (a) An 18650 cell was cycled through charge/discharge cycles within normal operational parameters of the cell. (b) The temperature observed along the axial length of the cell over time was recorded by an FOS and then the (c) average temperature value was calculated during this cycling event to determine the average rise in temperature. A variation of ±1°C was observed, with larger variations of ±2°C observed during discharges.

At the conclusion of the normal operation experiments, the same 18650 cell was short circuited in a controlled manner and the temperature and current during the event were charted as shown in Figure 2.9 (a). The data demonstrates that there are three well defined regions. As the short is applied, the temperature rises rapidly on the surface of the cell and the rate is much faster than anything observed during normal operation. This rapid rise in temperature causes the CID, which consists of a positive temperature coefficient (PTC) thermistor in series with the cell, to

increase its resistance due to a thermal trip set-point of 35°C. Once the CID engages the temperature starts to taper off and eventually it starts to decrease at a steady rate. The quick rate of temperature rise, dT/dt, in the first region is repeatable and as stated, it is not observed during normal operation. This means that when it is measured using a tailored algorithm, it can be used to autonomously identify that this abnormal mode of operation is occurring. Ideally, the control system can be notified of the abnormal operation and the battery can be disconnected from the power supply before a catastrophic failure occurs, however this may not always be possible. A flow chart describing this process is shown in Figure 2.9 (b) as it was incorporated into the LabVIEW monitoring system. A thermal rise of 2°C/s rate of change was measured after the short was applied; therefore, the value of the failure detection set-point, ϵ, was set to 1.8°C/s within the control algorithm as the change in temperature set-point at which the system detects that a short circuit condition has occurred. This set point must be maintained for 1 s for the system to identify a fault. Then, another identical short-circuit test was performed utilizing this control algorithm and the short was detected ~4 seconds after it was applied, which is illustrated in Figure 2.9 (c) and (d). This is an improvement of 26 seconds before the CID engages. It is not guaranteed that detecting this type of event can always prevent thermal runaway but it certainly increases the probability of preventing failure in most cases.
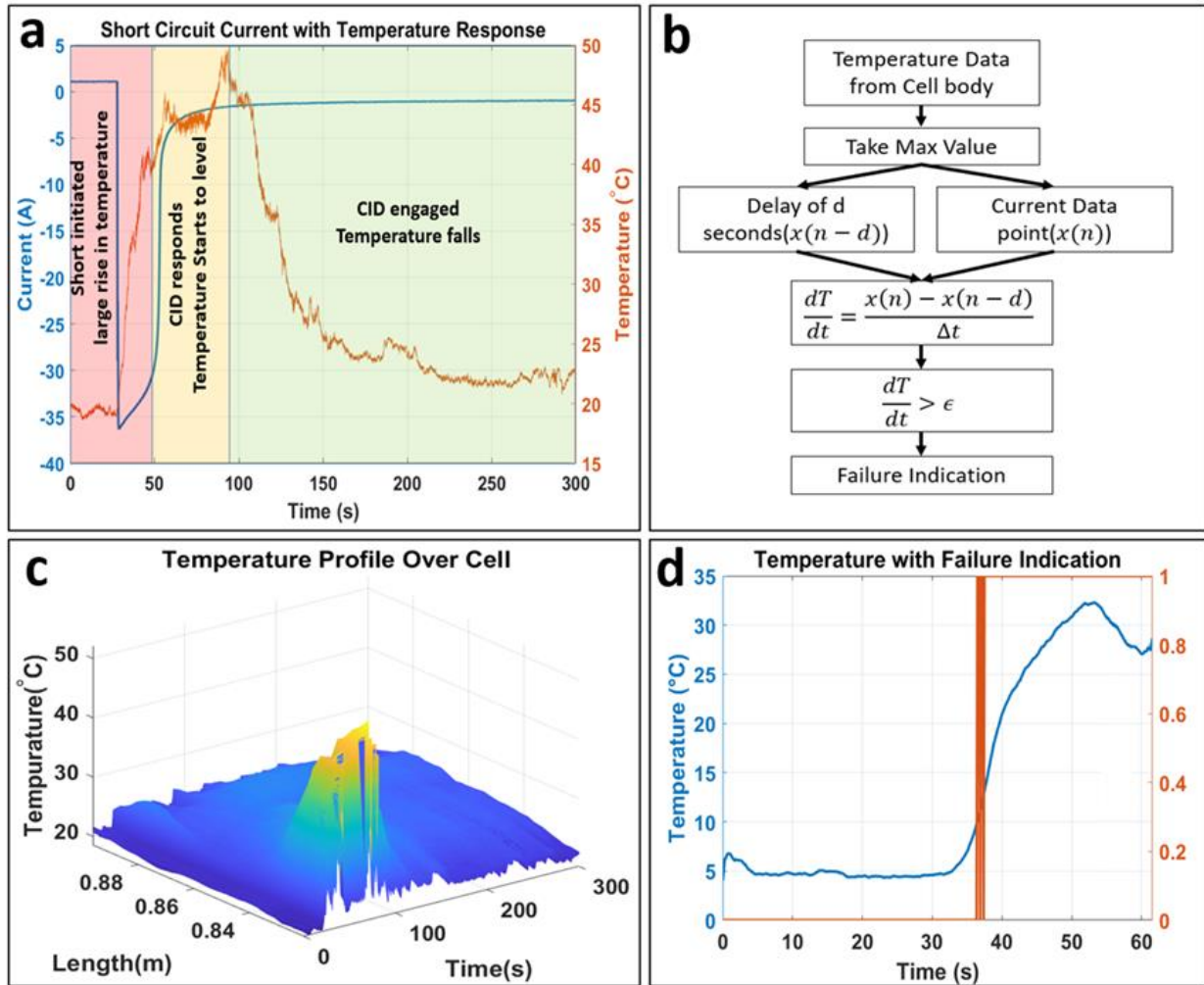
Figure 2.9. Thermal Detection of a Short-Circuit Event Within an 18650 Cell. (a) A short-circuit event was initiated within an 18650 cell and the temperature and voltage characteristics were tracked during this period of abnormal operation. The characteristics observed during this event were used to design an (b) algorithm within LabVIEW that could be used to identify a short-circuit condition and place the cell into a safe state. This algorithm was tested in an 18650 cell subjected to a short-circuit and the (c) temperature as a function of fiber length and time was recorded. (d) The average temperature over time was calculated to show that the algorithm

correctly identified the short-circuit event and placed the cell into a safe condition where the temperature would return to a safe condition instead of continuing to escalate.

Another identical 18650 cell, like Figure 2.6, was over-charged and the temperature and voltage characteristics were measured during this time, shown in Figure 2.10 (a). As in the short circuit experiments, the data demonstrates three well defined regions. At first, the temperature rises in the same way it does during a normal recharge. Once the maximum cell over-charge is reached, there is a sharp decrease in temperature followed by a rapid rise in temperature. Finally, there is a period of rapid temperature decline caused by the CID engaging and the cell no longer accepting any charge. The quick rate of temperature rise, dT/dt, in the second region is repeatable and is also not observed during normal operation. Using a similar algorithm to the one displayed in Figure 2.9 (b), this abnormal operation can be autonomously identified and a host control system can be notified of the abnormal operation and the battery can be disconnected from the power supply before a catastrophic failure occurs, however this may not always be possible. A flow chart describing this process is shown in Figure 2.10 (b) as it was incorporated into the LabVIEW monitoring system. A thermal rise of 1°C/s rate of change was measured after the short was applied; therefore, the value of the failure detection set-point, ϵ, was set to 0.8°C/s within the control algorithm as the change in temperature set-point at which the system detects that an over-charge condition has occurred. To observe repeatability, a second 18650 cell was instrumented with an HD-FOS identical to the previous experiment and was subjected to the same over-charge experiment. The results of the experiment are shown in Figure 2.10 (c) and (d). In Figure 2.10 (d), it should be noticed that there is one false positive measured during the experiment, seen by the red vertical line just shy of 3000 s, but it is a result of measurement noise. Since its duration was

shorter than the threshold of 1 s required for positive detection, it was ignored, and the experiment continued. At approximately 5100 seconds into the charge, a dT/dt temperature rate representing an overcharge event is measured. Because the experiment was setup to measure rate of change only and not isolate the cell upon detection, the experiment ran for an additional 286 seconds before the charge was stopped by the operator. During this time, the CID never engaged but the maximum temperature for the cell was not exceeded. This experiment shows how the fiber sensor can be utilized to detect failure conditions and prevent potentially hazardous operating conditions due to temperature fluctuations before a cell's own internal protection circuit even engages. The data from only two experiments are presented here but it should be noted that this was repeated many more times and the measurements were found to be repeatable.
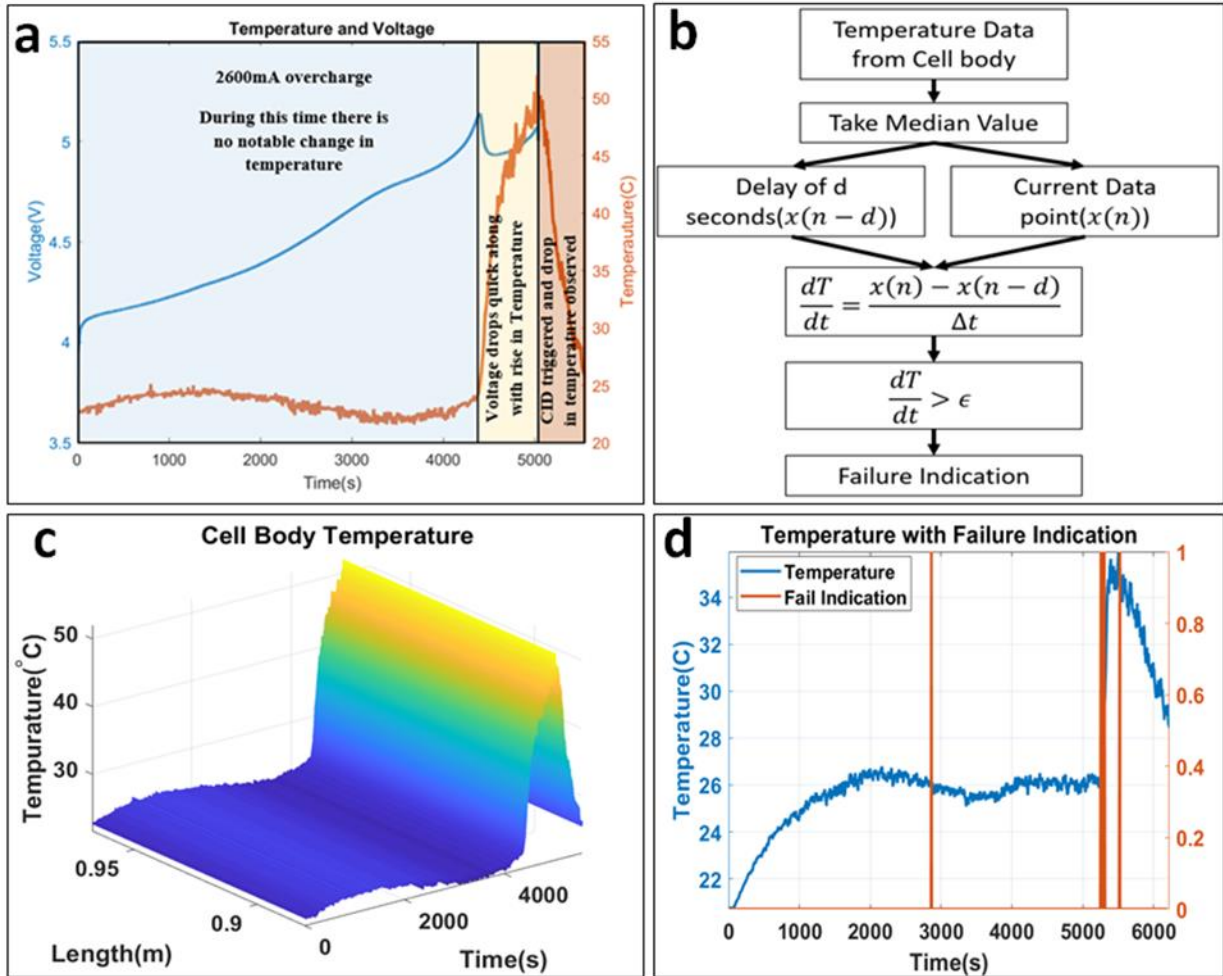
Figure 2.10. Thermal Detection of an Over-Charge Event of an 18650 Cell. (a) An over-charge event was initiated within an 18650 cell and the temperature and voltage characteristics were tracked during this period of abnormal operation. The characteristics observed during this event were used to design an (b) algorithm within LabVIEW that could be used to identify an over-charge condition and place the cell into a safe state. This algorithm was tested in an 18650 cell subjected to an over-charge and the (c) temperature as a function of fiber length and time was recorded. (d) The average temperature over time was calculated to show that the algorithm

correctly identified the over-charge event and placed the cell into a safe condition where the temperature would return to a safe condition instead of continuing to escalate.

2.5.2 STRAIN MEASUREMENT ON SINGLE CELLS USING A FOS

A second set of abnormal operation experiments were performed, very similar to those just presented, in which the fiber optic sensor was mechanically coupled to the cell and thermally isolated using three different adhesives to measure the induced stress/strain on the case. The identical 18650 cells were affixed with an HD-FOS using either hot glue, JB Weld, or Silicone as the adhesive and the cells were subjected to the same short circuit conditions previously described. The results presented in Figure 2.11 (a) show the recorded strain data from the HD-FOS and Figure 2.11 (b) shows the measured displacement from the laser rangefinder during the short circuit experiment. The short circuit initiates ~5 seconds into the experiment and the CID responds approximately 13 seconds after the short circuit initiates to open the cell electrically and a maximum current of 33 A was measured during the short circuit event. A representative comparison of the results seen with hot glue, JB Weld, and Silicone are shown in Figure 2.11 (d), (e), and (f), respectively. As seen in Figure 2.11 (d), the slope of the HD-FOS is clearly lagging that of the laser rangefinder which is believed to be the result of poor thermal conductivity of hot glue when used as an adhesive. Conversely, a comparison of strain and displacement in Figure 2.11 (e) and (f) show a strong correlation when JB Weld and Silicone are used indicating that these adhesives exhibit better thermal insulating properties required to prevent conductive heat transfer between the battery and the fiber during a short circuit event. An algorithm, similar to Figure 2.9 (b), was established for the detection of a short-circuit event where the detection set-point, ϵ, was set to 200 $\mu\epsilon$/s guaranteeing that the VI correctly identifies the adverse event, which is shown in

Figure 2.11 (c). Taken together, this data suggests that an HD-FOS coupled with the proper adhesive can be used to detect eminent failures using strain modes of measurement in a similar way that it was shown to measure steep changes in temperature earlier.
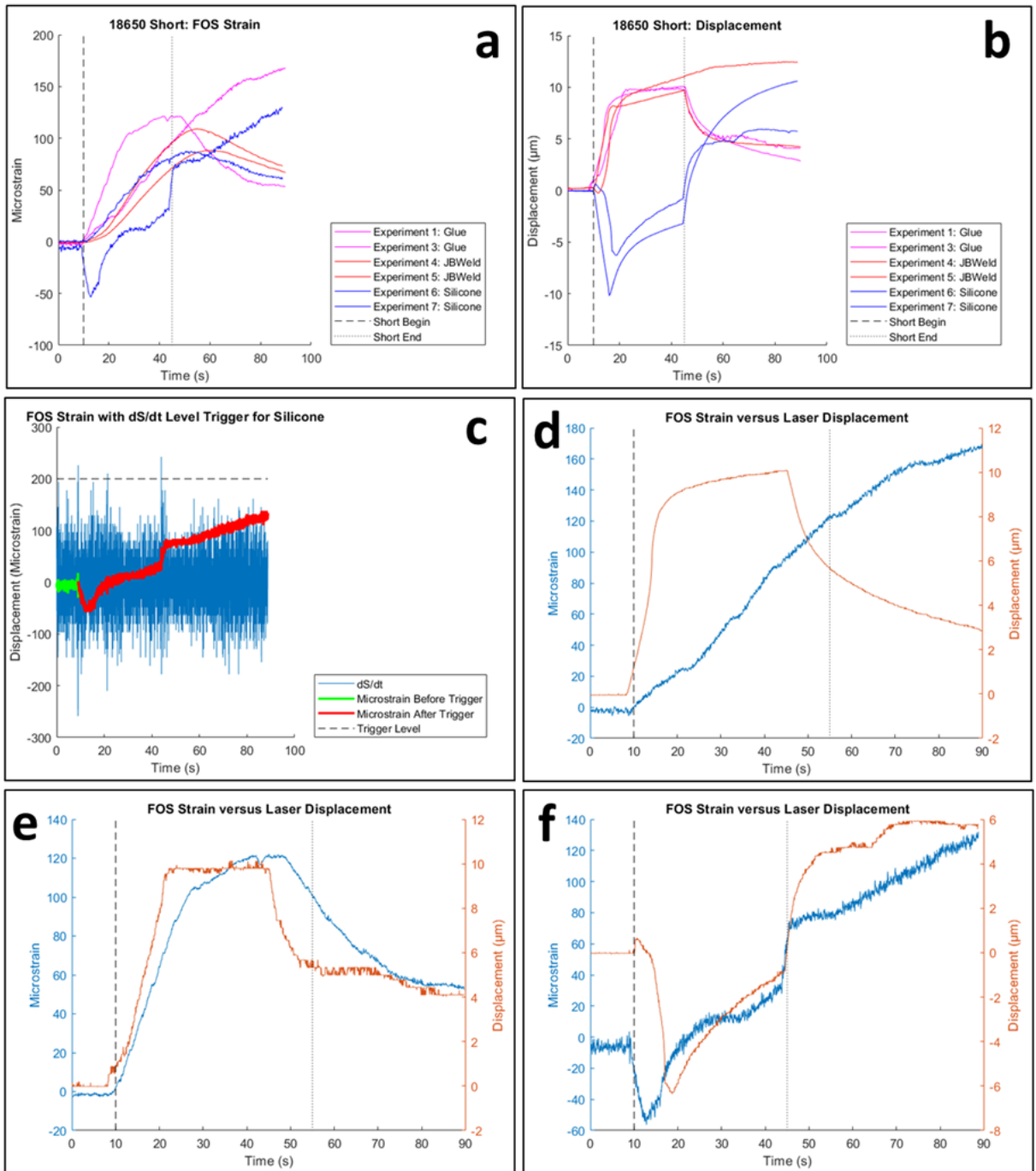
Figure 2.11. Short Circuit Test for Failure Validation Using an FOS to Measure Strain. A short circuit is initiated on an 18650 cell with a peak current of ~33A. The CID initiates ~13 seconds into the test and creates an open circuit on the cell. (a) The strain was measured during the short circuit using an HD-FOS attached to 18650 cells with three separate adhesives and

compared to the (b) displacement obtained using a laser rangefinder. (c) Based on testing, a measurement of greater than 200 µϵ/s was determined to be the point at which the system detects a short-circuit; therefore, the detection setpoint for the VI was set to this value. Representative results from each adhesive were plotted to show the correlation between the strain measured with the FOS and the laser rangefinder for (d) hot glue, (e) JB Weld, and (f) Silicone. (Dashed line indicates the start of the short, dotted line indicates the end of the short.)

Like the short circuit experiments, additional 18650 cells had an HD-FOS attached to one side of the cell using the same adhesives (hot glue, JB Weld, and Silicone) and were then subjected to the over-charge conditions presented earlier. Figure 2.12 (a) shows the voltage and current profile for these overcharge tests. Though the CID engages at different times, the over-charge experiments average about 4600 seconds until the internal CID protection engages and the cells accept approximately 2200 mAh over their rated capacity during these experiments. The strain was measured with the HD-FOS and the displacement was measured with the laser rangefinder during multiple tests using the three previously mentioned adhesives. In all tests, there is the same sharp repeatable rise in strain once the over-charge reaches a critical level. This sharp dS/dt is easily detectable by the LabVIEW VI which is intended to detect abnormal operation and it triggers an isolation event each time. Representative results from each of the three adhesives are shown in Figure 2.12 (c), (d), and (e) for hot glue, JB Weld, and Silicone, respectively. Similar to the short circuit testing, quick observation shows that there is a strong correlation between the FOS strain measurement and the displacement measured with the rangefinder for Silicone and JB Weld and little correlation observed when hot glue was used as the adhesive. An algorithm, similar to Figure 2.10 (b), was established for the detection of an overcharge event where the detection set-point, ϵ,

29

was also set to 200 µϵ/s which guarantees that the VI correctly identifies the event, which is shown

in Figure 2.12 (b). Again, this suggests that the thermal insulating properties of Silicone and JB

Weld are more effective at removing the effects of temperature observed by the FOS and more

accurately measure the strain effects alone by using the same detection set-point for the system to

detect both short-circuit and overcharge conditions.
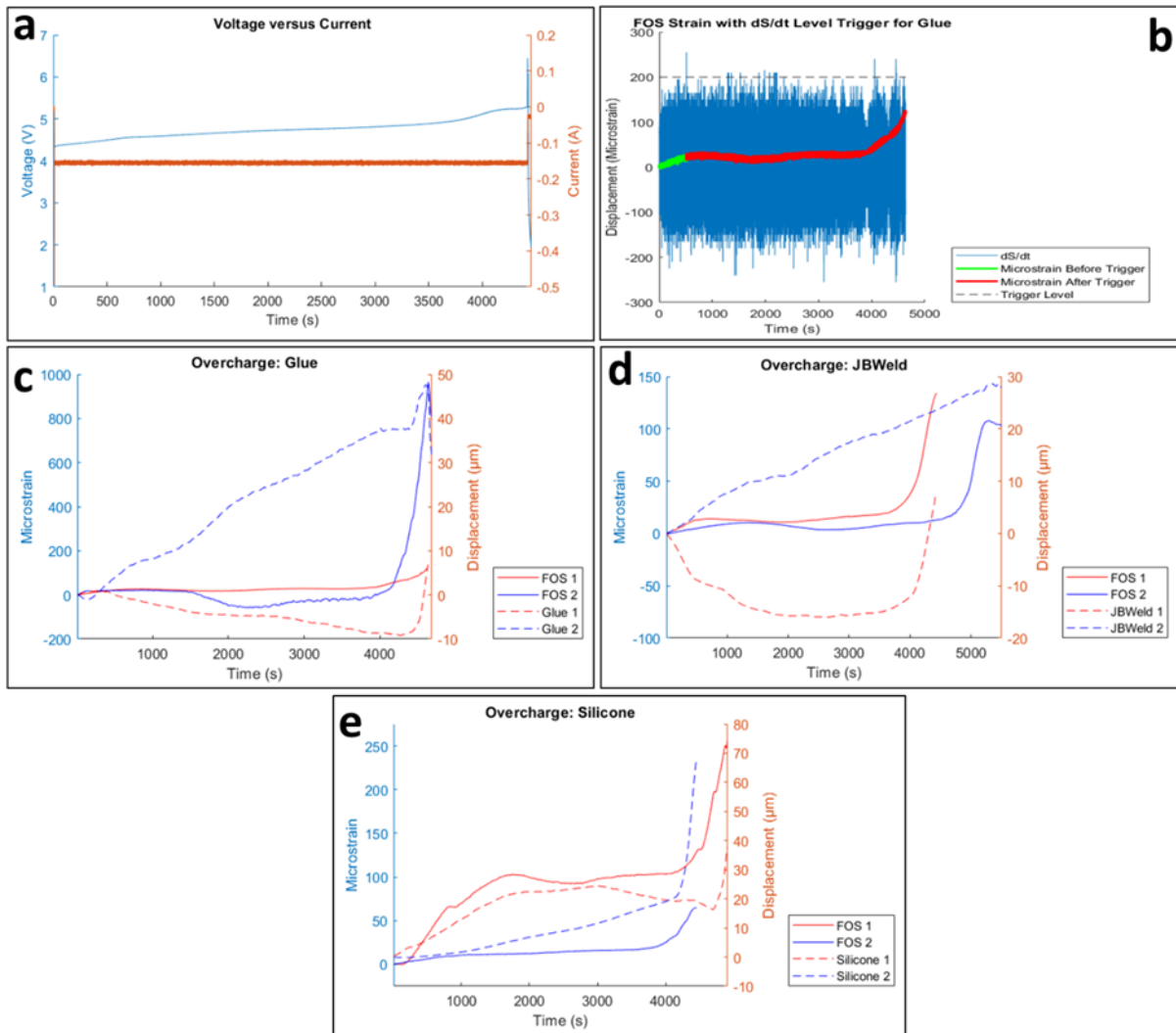
Figure 2.12. Over-Charge Test for Failure Validation Using an FOS to Measure Strain. (a)

Current and voltage profile for multiple over-charge experiments with 18650 cells using either

hot glue, JB Weld, or Silicone as the adhesive. (b) Based on testing, a measurement of greater

than 200 µε/s was determined to be the point at which the system detects an overcharge event; therefore, the detection setpoint for the VI was set to this value. Results from each adhesive were plotted to show the correlation between the strain measured with the FOS and the laser rangefinder for (c) hot glue, (d) JB Weld, and (e) Silicone. (The time stamp differs between each adhesive due to the point at which the CID engaged and disconnected the cell from the power source.)

The results in Figure 2.11 and Figure 2.12 verify that JB Weld and Silicone can both be used as an alternative adhesive for application of an FOS to the body of a cell. However, based on these results, sensors that are held in place by Silicone yield a stronger correlation to the results obtained using the displacement measured with a laser rangefinder and are determined to have the ability to measure a larger strain difference while still being thermally insulative. This observation was apparent during both short circuit and overcharge experiments and, when compared to hot glue experiments, the ease of application, repeatable results, flexibility, and temperature isolation of Silicone make it a good adhesive for fiber optic sensor application.

2.6 CONCLUSION

A Luna ODiSI and FOS can be used to measure either the temperature or strain within a battery, but cannot measure both simultaneously. It is known that temperature and strain increase during transient operating conditions, such as an overcharge or short circuit event. Therefore, systems that monitor battery operation for safety must be able to detect sudden increases in temperature and/or strain indicative of the onset of adverse conditions. An algorithm was developed that interfaced with the Luna ODiSI system with the capability of detecting a sudden

31

rise in temperature, dT/dt, with a rate of change set-point of 1.8°C/s for detection of an overcharge and a rate of change set-point of 0.8°C/s for detection of a short circuit. The purpose of these two separate set-points allow for the user to distinguish between whether an overcharge or short circuit event is occurring within a battery system on the cell level.

It was also shown that an insulating material can be used to adhere a fiber to the body of the cell and effectively decouple the temperature measurement from the stain measurement. Three adhesives were tested for their efficacy in this application with Silicone showing the highest performance as an adhesive and thermal insulator. An algorithm similar to the detection algorithm for rate of change of temperature was developed to measure a rate of change in strain. It was determined that a rate of change set-point of 200 µϵ/s accurately predicts the onset of both an overcharge and short-circuit event. Although this algorithm cannot differentiate between the two events based on which set-point is reached first, it does provide adequate monitoring of the change in strain during adverse operating conditions where the measurements made by an FOS closely follow the strain measurements obtained by a laser rangefinder.

This study shows that a Luna ODiSI FOS interfaced with a detection algorithm can measure either a rise in temperature or rise in strain on an individual cylindrical cell, but additional studies would need to be conducted to show the feasibility of this technique when applied to cells of other form factors or to modules consisting of multiple cells.

2.7 ACKNOWLEDGMENTS

expressed in this material are those of the author(s) and do not necessarily reflect the views of the Naval Air Warfare Center Aircraft Division (NAVSEA).

2.8 REFERENCES

[1] Y. Nishi, Lithium-ion secondary batteries; past 10 years and the future, J. Power Sources 100 (2001) 101-106.

[2] P.J. Bugrynieca, J.N. Davidson, D.J. Cumming, et al., Pursuing safer batteries: thermal abuse of LiFePO$_4$ cells, J. Power Sources 414 (2019) 557-568.

[3] Arhant, M., Meek, N., Penumadu, D., Davies, P., Garg, N. "Residual Strains using Integrated Continuous Fiber Optic Sensing in Thermoplastic Composites and Structural Health Monitoring." Experimental Mechanics, pp. 167-176, September 14, 2017.

[4] Stephen T. Kreger, Nur Aida Abdul Rahim, Naman Garg, Sandra M. Klute, Daniel R. Metrey, Noah Beaty, James W. Jeans, Robert Gamber, "Optical frequency domain reflectometry: principles and applications in fiber optic sensing," Proc. SPIE 9852, Fiber Optic Sensors and Applications XIII, 98520T (12 May 2016); https://doi.org/10.1117/12.2229057.

[5] Kreger, S., Rahim, N., Garg, N., Klute, S., Metrey, D., et al. "Optical frequency domain reflectometry: principles and applications in fiber optic sensing." *Proceedings of SPIE*, pp. 83-84. May 12, 2016.

[6] Kreger, S., Gifford, D., Froggatt, M., Sang, A., Duncan, R., et al. "High-resolution extended distance distributed fiber-optic sensing using Rayleigh backscatter." *Proceedings of SPIE*, pp. 1-12, April 10, 2007.

[7] Duncan, R., Childers, B., Gifford, D., Petit, D., Hickson, A., Jackson, A., Duke, J., Brown, T., "Use of a Fiber-Optic Distributed Sensing System for Nondestructive testing of Aerospace Structures," *Materials Evaluation* 61, 838 (2003).

[8] Kreger, S. T., Gifford, D. K., Froggatt, M. E., Soller, B. J., & Wolfe, M. S., "High resolution distributed strain or temperature measurements in single-and multi-mode fiber using swept-wavelength interferometry". In Optical Fiber Sensors p. ThE42 (2006).

[9] Pedrazzani, J.R., Klute, S. M., Gifford, D. K., Sang, A. K., and Froggatt, M. K., "Embedded and surface mounted fiber optic sensors detect manufacturing defects and accumulated damage as a wind turbine blade is cycled to failure," Proc. 2012 SAMPE Technical Conference, Baltimore, MD, May 21-24, (2012).

[10] Osgar John Ohanian III, Naman Garg, and Matthew A. Castellucci "Integrated fiber optic structural health sensors for inflatable space habitats", Proc. SPIE 10172, A Tribute Conference Honoring Daniel Inman, 101720B (10 April 2017);

https://doi.org/10.1117/12.2260106.

CHAPTER 3: FIBER OPTIC BASED THERMAL SENSING OF LITHIUM-ION CELLS AT THE MODULE LEVEL

3.1 MANUSCRIPT 2: BACKGROUND

Lithium-ion batteries have become integral to both consumer and industrial sectors due to attributes such as extended lifespan, higher energy densities, and reduced environmental impact. Despite these advantages, lithium-ion batteries are not immune to failures arising from abnormal conditions, poor management, mechanical stress, or design flaws. Thermal runaway, often accompanying battery failures, underscores the significance of battery monitoring systems that can detect changes in the battery's thermal state to predict and prevent issues. While current battery management systems (BMSs) monitor individual cell voltages and limited temperature points, there is a growing need for more comprehensive monitoring techniques as batteries become larger and more intricate. This article addresses this challenge by demonstrating the utilization of a high-definition fiber optic sensor (HD-FOS) to monitor temperature deviations in individual cells within a multi-cell battery module during cycling. Traditional temperature measurement methods, like thermistors and thermocouples, can be limited by their practicality in monitoring numerous cells. In contrast, HD-FOS presents a promising solution using swept-wavelength interferometry (SWI) to achieve high-resolution temperature measurements. By enclosing the battery module with a sinusoidally oriented fiber optic cable, the HD-FOS can detect minute shifts in optical spectra, correlating to temperature or strain fluctuations. This article presents experimental evidence of how the HD-FOS can identify anomalies within battery modules. The research also showcases a real-time detection algorithm that can alert a host controller to isolate the module in the event of abnormal thermal deviations, aiming to prevent thermal runaway and ensure safe battery operation.

3.1.1 MODIFICATIONS TO MANUSCRIPT FOR INCLUSION IN DISSERTATION

3.2 ABSTRACT

Battery modules are made up of many individual cells connected in series/parallel to meet an application's voltage, power, and energy requirements. Regardless of how big the battery is, its users assume it will always work safely. Wide scale deployment and the high cell count in modules bring about demand for new techniques to monitor individual cells and reduce the probability of an undetected catastrophic failure. A primary indication of a problem within a module is a significant rise in temperature and/or strain of one or more cells. Battery management systems (BMSs) monitor individual cell voltages and typically no more than a few temperatures. This introduces the possibility that cells may heat up without detection. This study demonstrates how a high-definition fiber optic sensor (HD-FOS) can be used to measure temperature deviations on each cell within a module consisting of multiple 18650 cells while it is being cycled. Controlled over-charge and short-circuit testing of cells within the module have been performed to show how

the sensing system can detect anomalies and report them back to a host controller. **Keywords**: lithium-ion battery; fiber optic sensor; temperature; high-definition fiber optic sensor.

3.3 INTRODUCTION

Lithium-ion batteries are increasingly ubiquitous throughout the consumer and industrial marketplace. Their rise in usage is due to the promise of longer lifespans, higher energy densities, lower self-discharge rate, and less impact on the environment compared to other conventional battery chemistries [1]. Unfortunately, this technology is not immune to potential catastrophic failures because of abnormal operating conditions, improper management, mechanical abuse, or inherent design flaws [2, 3]. It is known that battery failures are usually accompanied by thermal runaway [4, 5]; therefore, effective battery monitoring systems should closely interrogate the change in thermal state [4, 6-11] or induced strain [7, 12] because of thermal expansion within a system to predict and prohibit potential issues before they arise.

Potential problems within a lithium-ion battery may be detected by a battery management system (BMS) monitoring individual cell voltages in real time and no more than a few temperatures observed at a few strategic locations. Temperature measurements are usually made using thermistors or thermocouples that may be electrically conductive and difficult to manage if more than a few are used. Optical fiber sensing techniques show promising results for monitoring temperature, strain, relative humidity, and even radiation levels [13, 16-19]. These fibers are especially useful in battery monitoring for the measurement of temperature aberrations on cells within a battery module [1, 6-7, 19]. Initially, the technique employed in the fibers was based on multiplexing fiber Bragg gratings [17, 20]. However, this technique produces limitations to the spatial resolution that can be obtained [21]. Alternatively, swept-wavelength interferometry (SWI)

37

is a method of high-definition fiber optic sensing (HD-FOS) that is a more recent development and has improved the resolution of fiber optic sensors to less than 1 mm instead of 0.1 to 1 m, as seen in previous methods [14, 22-23].

Monitoring a battery module using a fiber optic cable requires encasing the module with a fiber sensor oriented in a sinusoidal pattern [24]. The HD-FOS technique utilizes a tunable laser source that passes light through the optical fiber attached to the battery in addition to a reference path [14]. Since each optical fiber has non-homogeneities that are an inherent result of the construction of the fiber, these non-homogeneities produce a random pattern of reflections which are then compared to a reference path within the optical system to create an interferometer [25]. The collected data is broken into small sections and a Fourier transform is performed to generate an optical spectrum. Shifts in this spectrum compared to the initial state of the sensor indicate a change in temperature within the material [7, 12, 18-19, 26-27]. Either temperature or strain can be measured, but not both simultaneously and measurement of temperature requires the fiber to be mechanically de-coupled and vice versa if strain is measured. For these experiments, temperature is measured using both a FOS with strain decoupled, in addition to thermocouples for measurement validation. It has been previously shown by the authors at the cell level that both thermal and strain sensing are valid measurements for the prediction of lithium-ion battery failure [19].

Since it is known that monitoring temperature is an effective means of determining whether a battery is entering a potentially catastrophic operating condition, much effort has been taken to test lithium-ion batteries at various cycling rates to create datasets that can then be used to model and simulate their thermal properties [5, 28]. This includes modeling and simulation of batteries at various environmental temperatures [10, 29-30] and creating empirical models based on the principles of energy balance within the battery [31]. These results and models, combined with

advanced Kalman filtering techniques, can then be used to provide an estimate of the state of charge (SOC) of a battery [32-34]. The ability to detect when a battery is deviating from expected conditions is critical for safe operation. Although these previous efforts provide a method for simulation and prediction of battery behavior, they do not always describe the use of real-time detection to protect a system from operating during a transient event. Further, when using conventional thermal measurement techniques, it is not feasible to measure the temperatures of more than a few cells within a multi-cell module. Though the sensors are strategically placed, the probability is high that a cell experiencing abnormal conditions will not be directly monitored. The ability to monitor the temperature of every single cell within a module in real time, something an HD-FOS can do, significantly improves safety. This is the focus of the work presented here.

In this study, an inexpensive telecom-grade fiber optic cable is used to measure the thermal change, dT/dt, on all cells within a multi-cell module while they are cycled in normal conditions and while select cells within the modules are abnormally charged and discharged. Thermocouples are attached to the module and a comparison between the thermocouple temperature measurements and the fiber optic measurements show close alignment between the two techniques. A real-time detection algorithm has been developed to sense abnormal thermal deviations in real-time and report back to a host controller that will attempt to isolate the module before thermal runaway occurs.

3.4 PROCEDURE, MATERIALS AND METHODS

The research performed here employs a commercially available Luna Optical Distributed Sensor Interrogator (ODiSI) and HD-FOSs to measure the change in temperature (dT/dt) within a battery module consisting of multiple 18650 cells arranged in series. The sensors are positioned

such that every cell body is sensed simultaneously. A series of normal, over-charge, and short-circuit experiments are performed to evaluate the efficacy of an HD-FOS monitoring system as an effective method for measuring normal operation as well as detecting and locating abnormal operation quickly.

3.4.1 CONSTRUCTION OF BATTERY MODULES WITH ATTACHED FOS AND MONITORING SOFTWARE

There are many ways to install an HD-FOS into a module. One method found to work well is to encase the fiber between two strips of polyimide tape [19]. Within the tape, the FOS follows a near sinusoidal pattern relieving strain in the bends while still allowing it to vertically contact each 18650 cell assembled in a multiple cell module. A photograph of a sensor encased in polyimide tape and an illustration demonstrating the sinusoidal pattern of the FOS on multiple cells within a module is shown in Figure 3.1 (a). As shown in Figure 3.1 (b), the sinusoidal pattern is properly spaced to measure the axial length of each 18650 cell within the module array that is constructed using interlocking blocks. Though any arrangement is feasible, the cells are laid out as either two rows of five cells to make a 10S/1P module or two rows of three cells to make a 6S/1P module in the modules studied here. The encased FOS is wrapped around these modules, as shown in Figure 3.1 (c) and (d), such that each cell is contacted. When measuring temperature, the sensor should be very loosely mechanically coupled to the cell. Encasing the fiber in tape as shown in Figure 3.1 (a) is a proven method for achieving this. Another involves placing the fiber into a Teflon tube. The Teflon tube can be tightly coupled to the device under test while the fiber is decoupled inside. Thermal heat transfer through the tape or Teflon tube should be considered but in most cases is negligible.
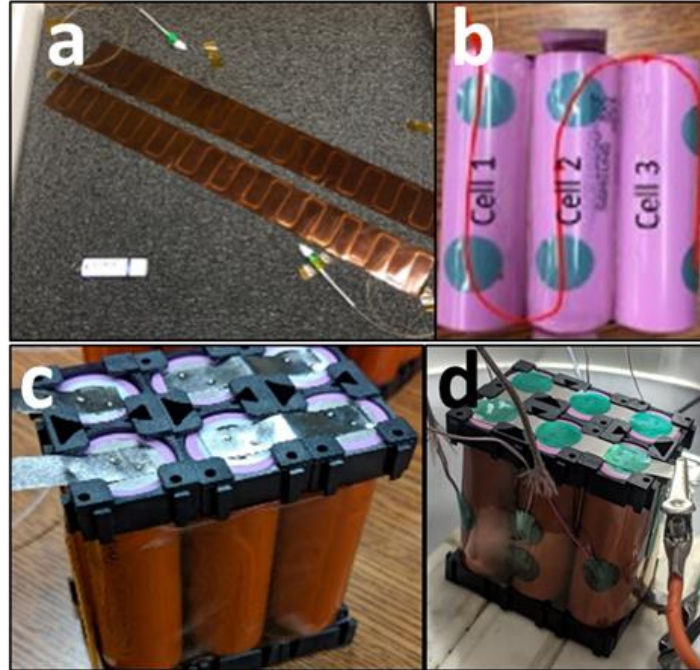
Figure 3.1. Construction of Battery Modules. (a) An FOS encased between two polyimide tape strips and module construction with a sketch showing the sinusoidal arrangement of the FOS across the cells within the module. (b) Sample construction of a battery module using modular connecting blocks. The terminals of the cells within the module were electrically connected using spot welded nickel strips. This modular design was used to construct a (b) 10S/1P module consisting of two rows of five Samsung 18650 cells and two 6S/1P modules consisting of two rows of three 18650 cells using (c) taped fiber and (d) taped fiber in addition to thermocouples placed on the sides of each cell.

Fibers as long as 50 m can be used but that length is not needed here. Data is collected in roughly 1.3 mm increments along the full length of the roughly 1.5 – 2 m long FOS but only the data collected along the length of each individual cell is of interest. Identification of the points of interest along the fiber length can be achieved in a few different ways. Using the simplest method, the FOS is placed onto the module under test in an open-air environment where the points of

interest are identified by hand using the touch to locate feature integrated into the ODiSI software. When the sensor is integrated into commercially produced modules, the ability to access the FOS and identify points of interest becomes much more difficult. To mitigate this challenge, a custom LabVIEW Virtual Instrument (VI), operated in tandem with MATLAB, was developed to automatically identify points of interest (POI) along the fiber in each of the modules. It identifies the location of the body of each cell without the need for programming their locations by hand. This technique is demonstrated to be useful with individual modules in this research effort and it becomes increasingly more valuable as the number of cells and modules assembled in a battery increase. Figure 3.2 (a) displays the front-panel of the VI that has been developed and it displays a plot of the temperature versus length of the FOS recorded during a low C discharge cycle. Figure 3.2 (b) provides an example of the VI identifying two points of interest along a fiber. Prior to cycling, the user defines a threshold over which data will be considered. The two peaks in Figure 3.2 (b) correspond to the terminals of a cell while the points between are those measured axially on the cell body. Once the points of interest have been determined, a battery module can then be subjected to a charge/discharge cycle and the VI will identify the body of each cell within the module for temperature sensing.
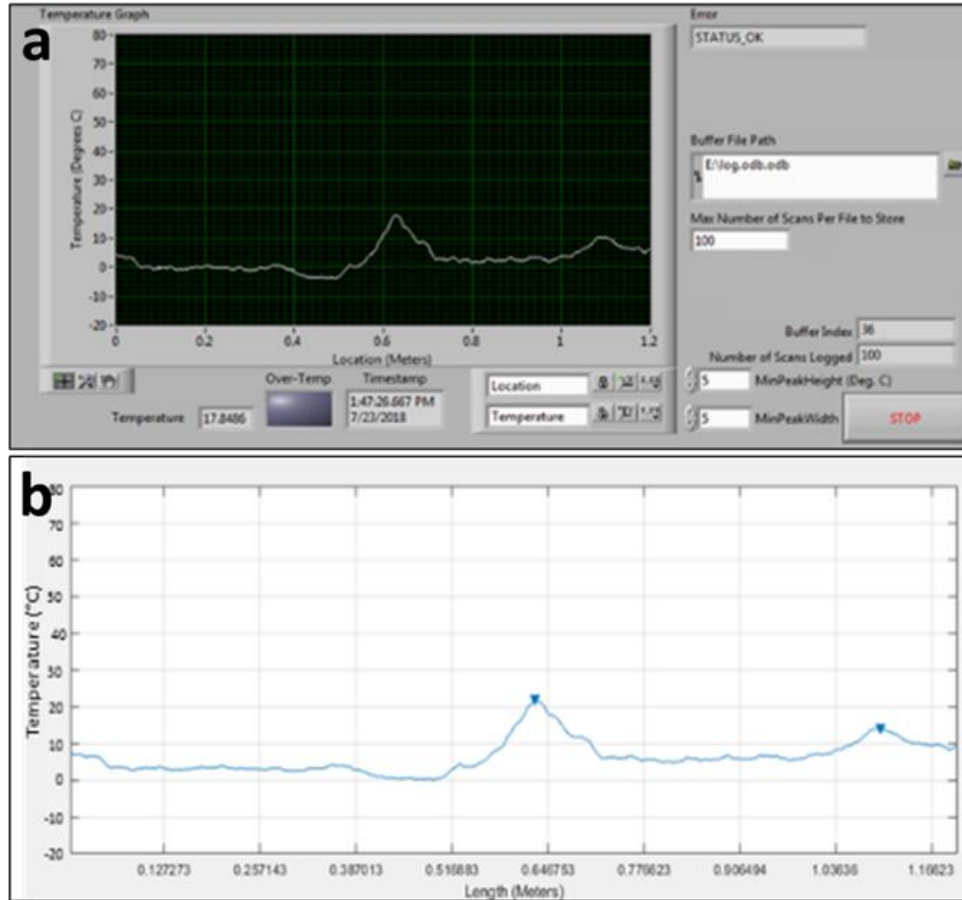
Figure 3.2. HD-FOS Data Collection Software. (a) The thermal characteristics within each module are monitored using a custom LabVIEW VI. This VI was designed to monitor temperature fluctuations within the cells in a module and (b) identify points of interest along the FOS (i.e., cell terminal locations). Other features of this VI include the ability to buffer the amount of data stored. In the event of a failure, the data collected by the FOS system will be saved for analysis to determine what failure occurred and where.

3.4.2 THERMAL EVALUATION OF MULTI-CELL MODULES WITH A FOS

Multiple experiments will be presented here in which an HD-FOS has been used to measure temperature along all cell bodies within a lithium-ion module operated under normal and abnormal

conditions. During normal operation, it will be shown how the fiber measures each individual cell temperature and how it correlates with a standard thermocouple measurement. During abnormal operation it will be shown how there is a rapid rise in temperature, dT/dt, measured at the start of each respective abnormal event. When the dT/dt measured exceeds a pre-set software threshold, the sensing system indicates that an abnormal event is occurring which can then be sent back to a host controller, where action can be taken to hopefully prevent further escalation. Any tests in which temperature is measured were performed with a rest period of one hour after each one to ensure that any residual temperature had time to decrease between experiments. Due to the destructive nature of overcharge experiments, these were only performed once per module.

3.4.2.1 NORMAL CYCLING

It has been previously shown that a cell's thermal change can be detected in real-time using a FOS attached directly to a battery cell [5, 10, 19]. Here, a 1S/6P module is assembled using modular connecting blocks and 18650 cells in accordance with the design outlined in Figure 3.1 (c). This configuration is arbitrarily chosen. The cycling procedure described below is used to charge and discharge the module for point of interest (POI) identification along the fiber and for thermal evaluation. The 18650 cells are lithium cobalt oxide (LCO) chemistry, have a capacity of 2.6 Ah, and have a maximum discharge rating of 2C.

1. Apply a 1C constant current/constant voltage (CC/CV) charge to 4.2 V with a 0.1C cutoff (15.6 A charge with 1.56 A cutoff)

2. Apply a 1C constant current (CC) discharge down to 2.7 V

3. Recharge at 1C CC to 4.2 V

4. Discharge at 1C CC to 2.7

3.4.2.2 THERMAL EVALUATION OF BATTERY MODULES INTENTIONALLY OVER-CHARGED

Cells and modules experience rapid changes in temperature and strain when they are overcharged. In the work performed here, three overcharge tests were performed to demonstrate the FOS's ability to autonomously detect this fast rate of change from cells contained within a 6S/1P module. From our previous research with single-cell overcharge [19], we observed a dT/dt of around 1°C/s. Due to the parallel configuration of the module, we expected that the rate of temperature change would be less than that for a single cell, due to the increased time to overcharge the module. In the first test, a single cell within a 6S/1P module is overcharged to 5 V with a current limit of 2.6 A (1C). The second experiment consisted of overcharging a 1S/6P module with a voltage limit of 10 V and a current limit of 31.2 A (2C). In the third experiment, four cells within a 6S/1P module were overcharged while the remaining two cells were present but electrically disconnected. They were overcharged with a voltage limit of 16.8 V and current limit of 2.6 A (1C). Thermal data was collected from the fiber and was compared with a recording produced with a thermal imaging camera. In each of these experiments, it is demonstrated how the fiber optic sensor can measure the temperature change on each cell and how the cells experiencing overcharge are quickly identified.

3.4.2.3 THERMAL EVALUATION OF BATTERY MODULES INTENTIONALLY SHORT-CIRCUITED

When lithium-ion cells are short-circuited, a similar rapid rate of temperature change occurs. Our previous research with single cell short-circuits showed a dT/dt rate of around 2°C/s

[19]. In this set of experiments, cell(s) within a six-cell module were short-circuited in a controlled manner to demonstrate the use of a FOS to detect the rate of change autonomously and rapidly. The short-circuit is achieved by connecting the module to a high current mechanical relay made by Ross Engineering. The module rests for ten seconds, the relay is held closed for 30 seconds, and then the relay opens and the cell rests while data is collected for an additional 50 seconds. In most cases, one or more cells' positive temperature coefficient (PTC) device engages due to a high enough thermal rise within the cell but not always. Three short-circuit experiments were performed. In the first experiment, only a single cell was short-circuited within a 6S/1P module. In the second experiment, the entire 1S/6P module was short circuited and finally in the third experiment, a 6S/1P module was short circuited. Thermal data was collected from the fiber and was compared with results from an infrared camera. In each of these experiments, it is demonstrated how the fiber optic sensor can measure the temperature change on each cell and how the cells experiencing abnormal discharge conditions are quickly identified.

3.5 RESULTS AND DISCUSSION

3.5.1 NORMAL CYCLING

The thermal results collected during steps 1 through 4 of the procedure documented earlier are shown in Figure 3.3. The temperature change measured on each cells' surface using the FOS as well as from a thermocouple placed on each one is shown. Since this is a low C rate procedure, the temperature rise expected is minimal, but it is clearly still visible. While the cell is being charged and discharged at 1C, the temperature rises but as soon as the CV portion of the charge begins, the temperature of each cell starts to fall as anticipated. As seen in the data, the measurements from both the FOS and thermocouple agree well during the cycle procedure. There

46

is some variation between the two measurements and that is expected since the FOS data is data averaged across all the points measured axially along the cell while the thermocouple is only a single point measurement. Figure 3.3 (b) shows voltage and current measurements made during the experiment. The data shows how a single, non-invasive FOS works to easily measure every cell in a multi-cell battery and this improves overall system monitoring and safety over traditionally limited single point thermocouple measurements. While not shown in Figure 3.3, it should be noted that the dT/dt rate during normal cycling peaked around 0.3°C/s, which occurred prior to the CV portion of the charge.
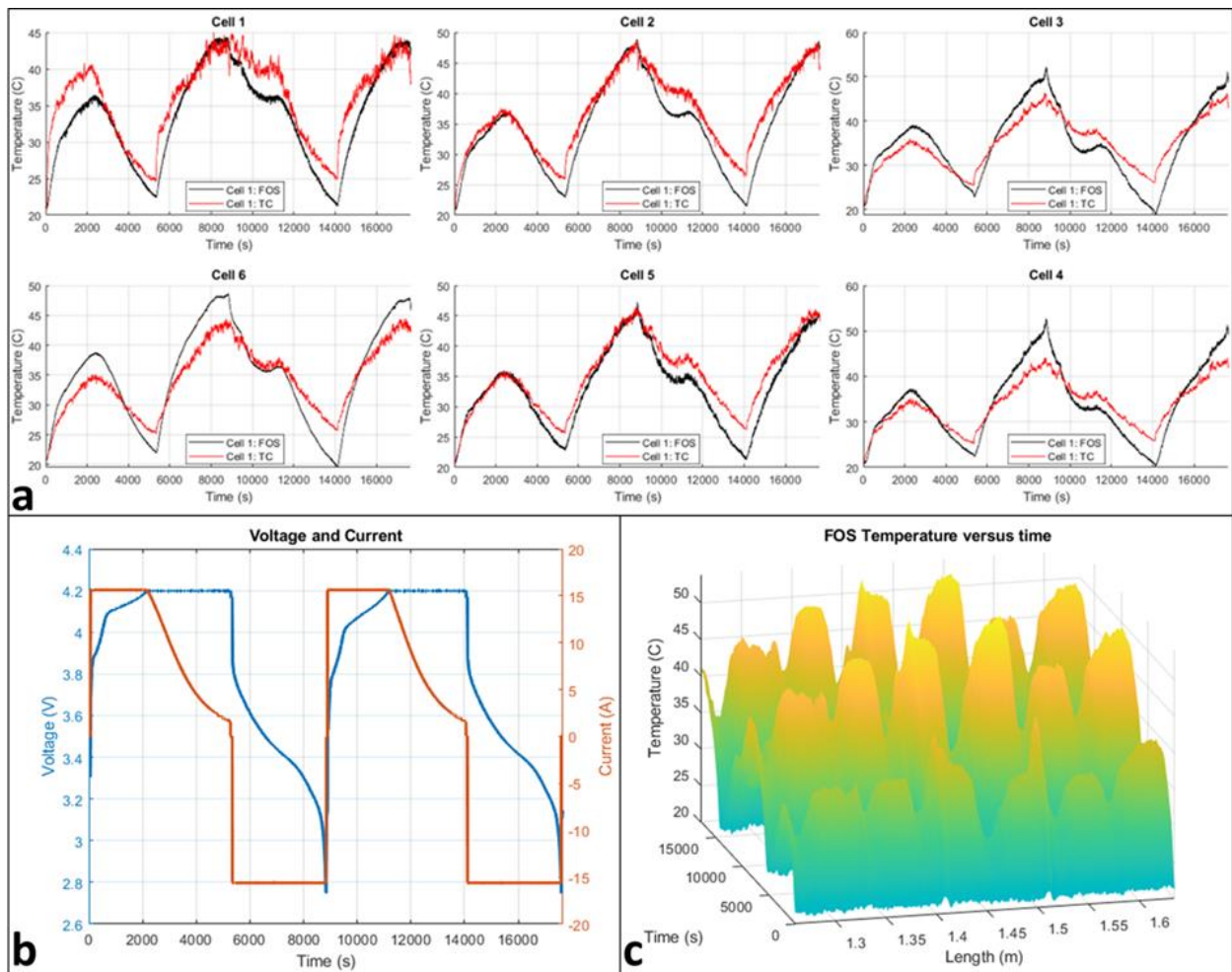
Figure 3.3. Temperature Response During Cycling of a 1S/6P Module. (a) A 1S/6P module is subject to two cycles of CC/CV charging/discharging. (b) The voltage (left axis) of this

47

module cycles between 4.2 V and 2.7 V and the current (right axis) cycles between 15.6 A maximum charge and 15.6 A maximum discharge. (c) 3-D temperature plot displaying the relation of the cell temperatures as a function of length of FOS and time. The temperature recorded during cycling shows a difference of approximately 10°C between temperatures measured along the side of the cells and the space between each cell.

3.5.2 THERMAL EVALUATION OF BATTERY MODULES INTENTIONALLY OVER-CHARGED

Multiple abnormal operation experiments have been performed in a controlled manner to demonstrate how clearly the cells behaving abnormally are quickly identified using a FOS. In the first, a single cell, cell 3, within the 6S/1P module shown in Figure 3.4 (a) is intentionally overcharged in an open-air environment by directly connecting a power supply across it that is set to 5 V with a current limit of 2.6 A. The thermal data recorded across each cell by the FOS is shown in Figure 3.4 (b). As expected, cells 1,2, and 4 – 6 remain at nearly the same temperature, though cell 4's temperature does increase slightly due to the radiated heat given off by cell 3. Cell 3 heats up steadily as expected due to power losses dissipated inside the cell during the overcharge event. Roughly 4500 seconds into the experiment, the temperature rapidly increases as the cell voltage approaches 5 V. This rapid rate of change is critical to identifying that something is going wrong. The VI monitoring the FOS data continuously calculates the rate of temperature change, dT/dt, across the segment(s) of fiber in contact with each cell. When the measured dT/dt exceeds the threshold, preset by the user, the VI sets a digital flag, seen in Figure 3.4 (c). Because the FOS data is changing quickly, there are many false flags set so the software checks to make sure the flag is not a false positive before it is physically put out on a digital output channel to the BMS or

48

other ancillary hardware. This is done by downsampling the data, which eliminates point-to-point differences with very high dT/dt measurements. Thus far, this has found to be a very reliable way of preventing false flags from stopping any operations. For this set of overcharge experiments, their long length required a larger downsampling to produce a reliable dT/dt trigger. The values used to downsample was one point every 1000 samples. Though it is not guaranteed that that FOS will always detect the rate of temperature change before the PTC engages, it was repeatable in the multiple similar experiments performed.

Although normal thermocouples can similarly detect this same type of event, the advantage here is that the FOS measurement system is able to monitor every cell using a single, dielectrically isolated sensor. Additionally, because the FOS is measuring multiple points along the axial length of the cell, redundancy is naturally integrated. It is clearly visible in the results shown in Figure 3.4 (b) that cell 3 is behaving much differently than the other five cells and the monitoring system can identify and locate this difference in real time. If the FOS was not monitoring every cell and instead only a single thermistor or thermocouple was positioned within the module away from cell 3, the safety of the module would rely only on the PTC within cell 3 engaging and the user would not know what caused the module to open circuit when it does. Further, if the PTC did not engage, the abnormal event could go undetected until the heat is propagated to where the sensor is located, or thermal runaway occurs.
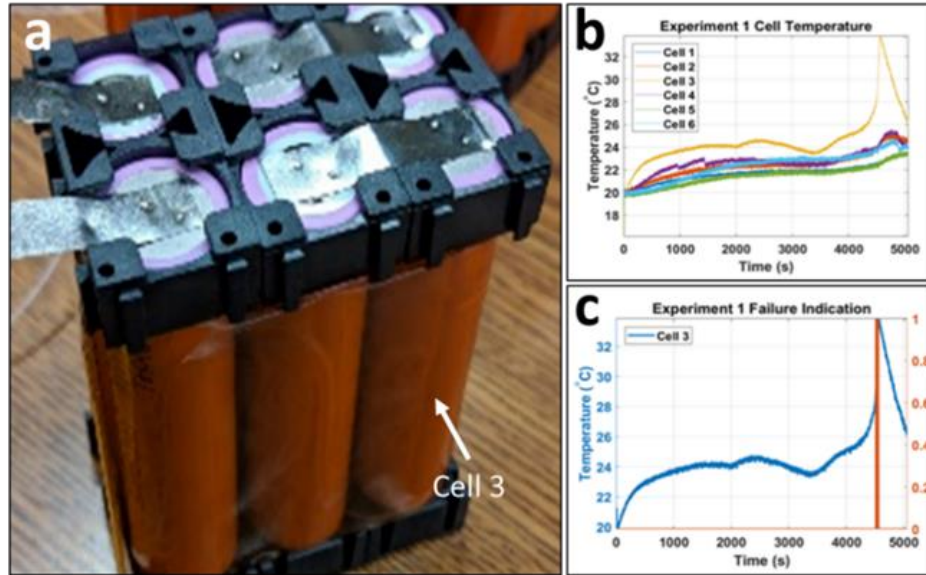
Figure 3.4. Overcharge of a Single Cell Within a 6S/1P Module Consisting of 18650 Cells.

(a) Cell 3 within the module was overcharged and the temperature fluctuation within (b) each cell was recorded and within the (c) overcharged cell throughout the entirety of the test. Cell 3 in the module was overcharged until a thermal signature was obtained and results from the overcharging of this cell shows the temperature at the point of failure, which occurred approximately 4500 seconds into the test.

In the second series of over-charge experiments, a 1S/6P module was overcharged across the module terminals using a power supply set to 10 V and 31.2 A. As with the previous module, this one was instrumented with an FOS taped onto the module, in addition to a thermocouple instrumented on each cell.

The FOS and thermocouple results collected during the experiment are shown in Figure 3.5 (a). There is some difference between the two types of measurements, as much as 8%, 5°C, on cell 1, but this is expected due to the thermocouple being located slightly away from the fiber and because of the averaging that occurs across the axial length of the fiber. The digital flag produced

by the dT/dt measurement of both the thermocouple and FOS has similar start locations in Figure 3.5 (d, e), but due to some unfiltered noise, the dT/dt from the FOS triggered earlier than that from the thermocouple. It should be noted that data for this figure needed noise reduction and downsampling to reduce false-positives. To generate reliable dT/dt trigger events, the raw data was sampled every 1000 samples, about 0.02Hz. While this does increase the accuracy of the trigger, it does delay the response time. This also has the effect of a lower dT/dt than would normally be seen, when compared to single-cell overcharge events [19]. The trigger events occurred around 9300s into the overcharge, at around 5.45 V, for a dT/dt limit of 0.5°C/s.
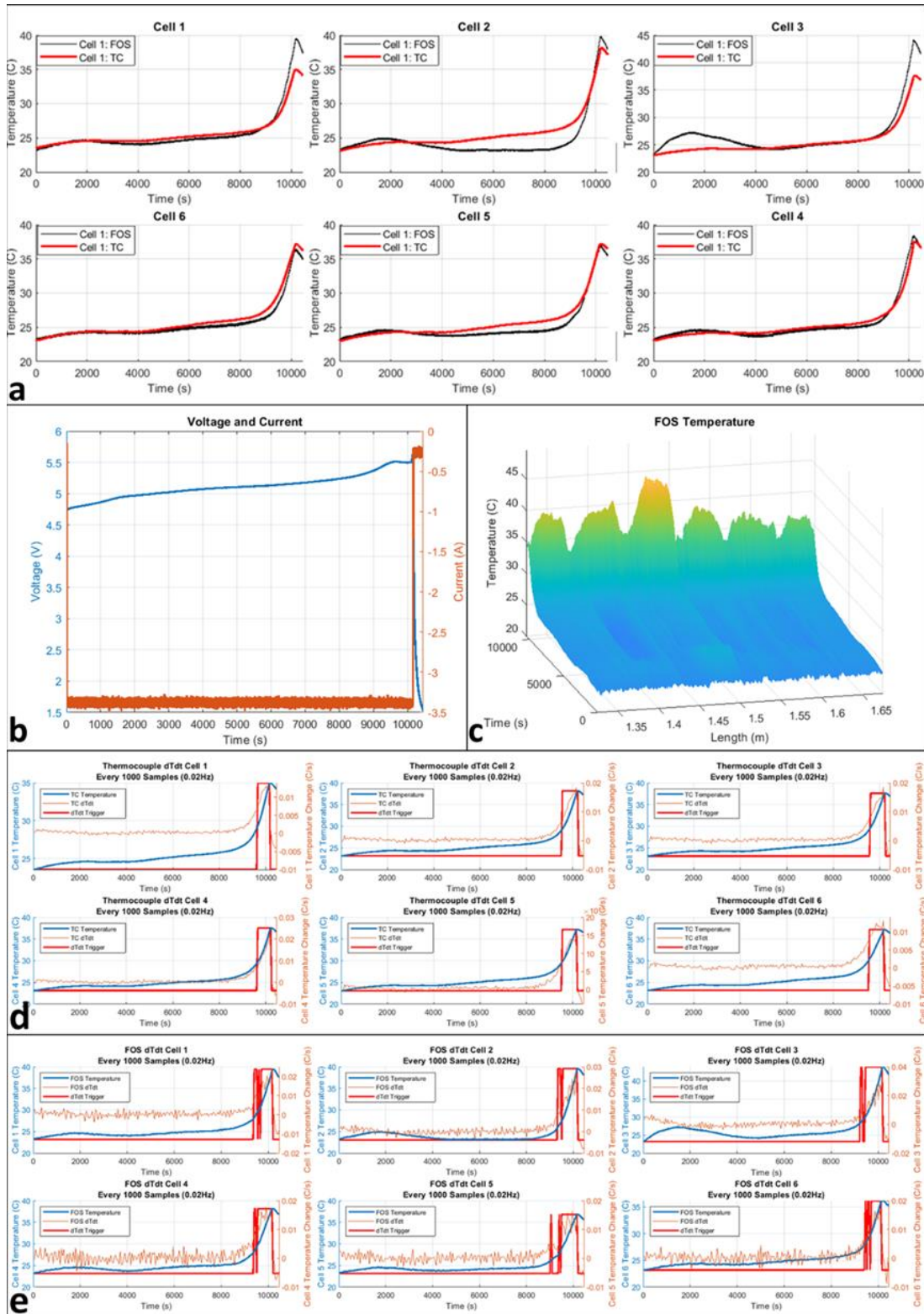
Figure 3.5. Overcharge Testing with a 1S/6P Module. (a) A 1S/6P module was constructed

and used for overcharge experimentation, and a thermocouple was placed on the side of each cell

52

in the module, shown in Figure 3.1(d). This also shows FOS data along the same section of the cell where the thermocouple is mounted. (b) Voltage and Current measurements during the overcharge were recorded, with the datasheet maximum voltage of 4.2 overcharged to 6 V before failure. (c) The temperature data from the HD-FOS for the overcharge test easily distinguishes the six cells within the module. (d) Thermocouple dT/dt data per-cell for the module, with an additional plot, shown in red, of a digital flag that can be sent to a BMS. (e) FOS dT/dt data per-cell for the module, and similarly to the TC dT/dt, a digital flag is added.

In the third set of overcharge experiments, four cells within a 6S/1P module are overcharged by connecting a power supply set to 16.8 V with a current limit of 2.6 A across them. The 6S/1P module was assembled and instrumented with an FOS. A photograph of the setup is shown in Figure 3.6 (a, c). Four of the six cells were electrically connected in series while the remaining two were electrically connected but not to the other four. This experiment further demonstrates the ability to identify the cell(s) that are having problems within a large array of cells in a module or battery. In addition to the FOS, the module's thermal change was measured using a FLIR infrared camera. Thermal results measured using the FOS and the FLIR camera are shown in Figure 3.6 (b), (d), and (e). During the overcharge experiment, a total of three PTC's were audibly heard activating. The thermal data recorded by both the HD-FOS and FLIR camera clearly show the four overcharged cells heating up and the correlate to each other. The thermal propagation to the two cells that were electrically disconnected from the 6S/1P module is apparent in the data recorded by the HD-FOS and verified by the infrared images shown in Figure 3.6 (b) and (d).

Figure 3.6. Over-Charge Testing of a 6S/1P Module Coupled with Infrared Imaging. (a) A 6S/1P module with a taped FOS was placed inside a chamber designed for destructive experimentation. (b) Infrared imaging during an overcharge test showed a clear distinction between the four overcharged cells and the two disconnected cells during the course of the test. This infrared imaging was recorded by a FLIR camera located within the (c) chamber, which also recorded the rise in temperature observed on the (d) terminal connections of each of the 18650 cells.

3.5.3 THERMAL EVALUATION OF BATTERY MODULES INTENTIONALLY SHORT-CIRCUITED

The first intentional short-circuit experiment was performed similarly to the first over-charge experiment. In it, a single cell, cell 5, within a 6S/1P module is shorted for 30 seconds. Shown below in Figure 3.7 (a), a large temperature change is detected immediately after the short circuit is applied. This large change in temperature is detected approximately 50 seconds prior to

the built-in cell protection. A significant temperature deviation across the cell is detected as well. Visible in Figure 3.7 (b), only one terminal of the cell experienced this rapid heating during the short circuit experiment, meaning that a thermocouple or thermistor on the body of the cell would not have captured this rate of change. It would have likely still detected a failure, but much later than the FOS.
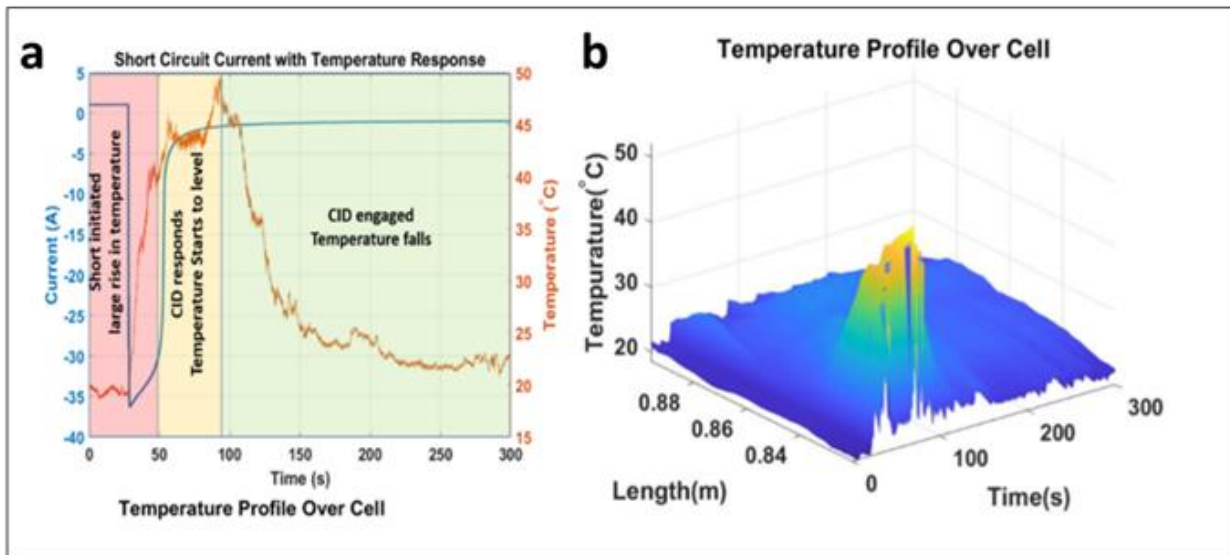
Figure 3.7. Temperature Measurements During Short-Circuit Testing of 6S/1P Module. (a) Thermal and voltage results collected when a single cell is shorted within a 6S/1P module. (b) Collected temperature data from the FOS. Cell 5 in the array is shorted and a thermal signature is obtained. Approximately 25 seconds into the experiment, cell 5 experienced a rapid rise in temperature on one terminal. The other cells in the battery had little thermal response to cell 5 being shorted.

In the second set of short circuit experiments, another 1S/6P module was constructed for evaluation under controlled short-circuit conditions. In this experiment, the entire 1S/6P module

is short-circuited for 30 seconds, preceded by a 10 second rest. The short-circuit is followed by a 50 second rest to collect additional data. Figure 3.8 below shows data collected from each of the cells within the module during the test using both a FOS axially mounted to each cell and a thermocouple mounted on the side of each cell, like Figure 3.1 (d). As expected, each cell experiences a similar rapid rise in temperature induced by the ohmic heating the high short circuit current induces. The dT/dt flag is quickly thrown for all thermocouple and FOS measurements. The advantage to the FOS is again the ability to monitor every cell simultaneously rather than relying on lucky placement of a thermocouple on or near the cell(s) experiencing the short. Due to signal noise from both the thermocouple and FOS, downsampling was used to reduce false-positives, with one in every 50 samples used for rate calculation. Though downsampled, the faster duration of the short-circuit allowed more samples to be incorporated than with the overcharge experiments. This showed better agreement with our previous experimentation [19].
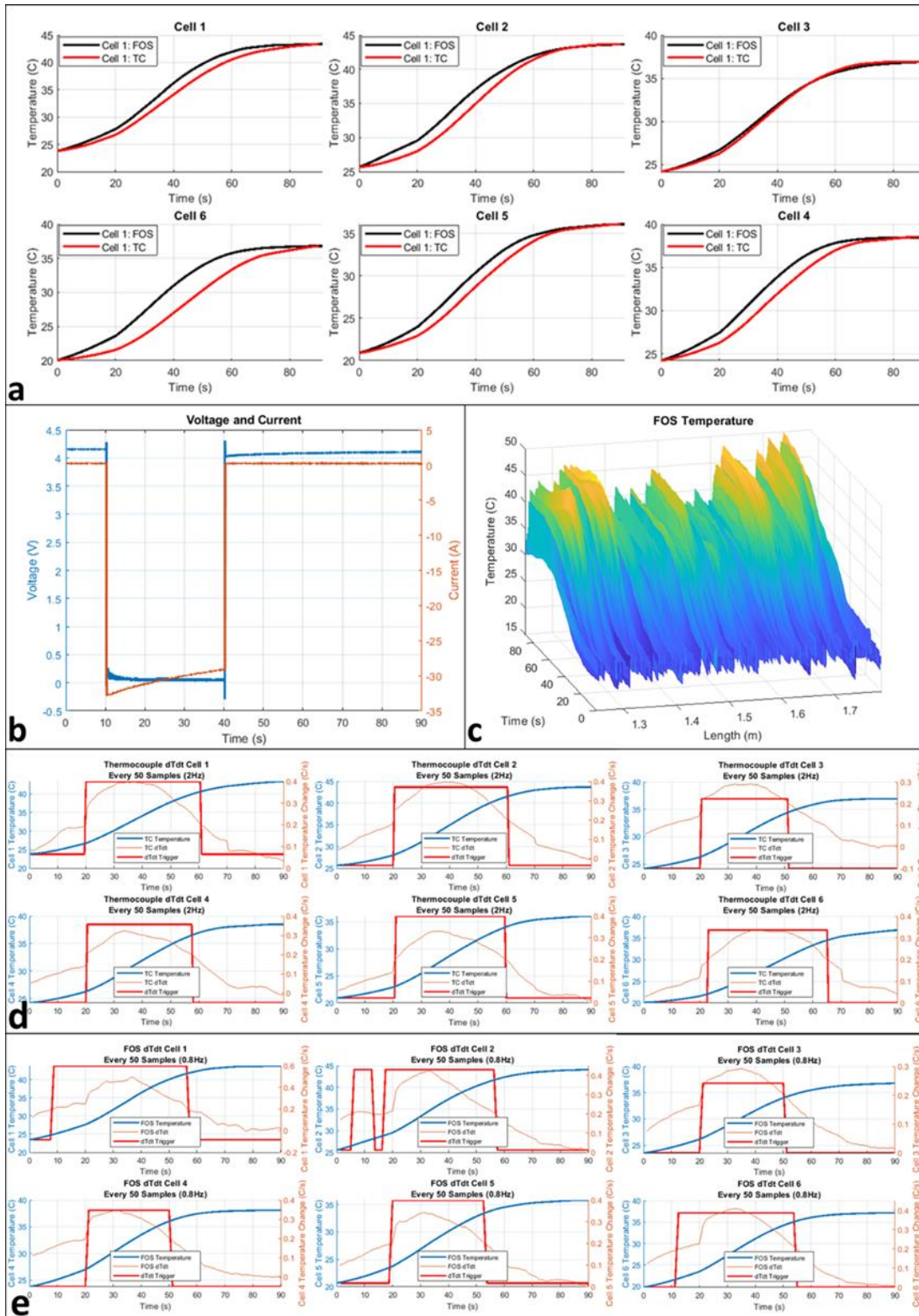
Figure 3.8. Temperature Measurements During Short-Circuit Testing with 1S/6P Modules.

(a) The recorded temperature during the first short circuit event (a) from both the FOS across

57

each cell and a thermocouple placed on the side of each cell within a 6S/1P module. (b) Voltage and current measurements obtained during the experiment. (c) 3-D plot showing the temperature measured across the full length of the FOS versus time. (d) Thermocouple dT/dt and digital flag for each cell within the module. The trigger was set at 0.075°C/s for both the FOS and thermocouple dT/dt. The dT/dt for all six cells measured by the thermocouple hit the trigger rate at around 10 seconds into the short-circuit. (e) FOS dT/dt for each cell within the module. There was slightly more variance for the initial trigger time of the digital flag, averaging about 5-10 seconds into the short circuit.

In the last experiment presented, a 6S/1P module was short-circuited while the temperature rise is recorded by the FOS and a FLIR camera, with an identical procedure to the previous short-circuit. A ten second rest is followed by a 30 second short, concluded with a 50 second rest for data collection. The experimental setup and associated recording equipment can be seen in Figure 3.9 (a) and (c). During the test, all the cells' terminals exhibit an increase in temperature. Cell 4 shows the highest temperature rise, observed in Figure 3.9 (b) and (d). These temperatures then decrease as the cells internal protection activates, limiting the short-circuit current. In Figure 3.9 (e) below, the temperature deviation from room temperature, 20C, for cell 4 is about 15C, and the temperature measured by the FLIR camera on cell 4 also read around 35C, confirming the temperature recorded by the FOS.
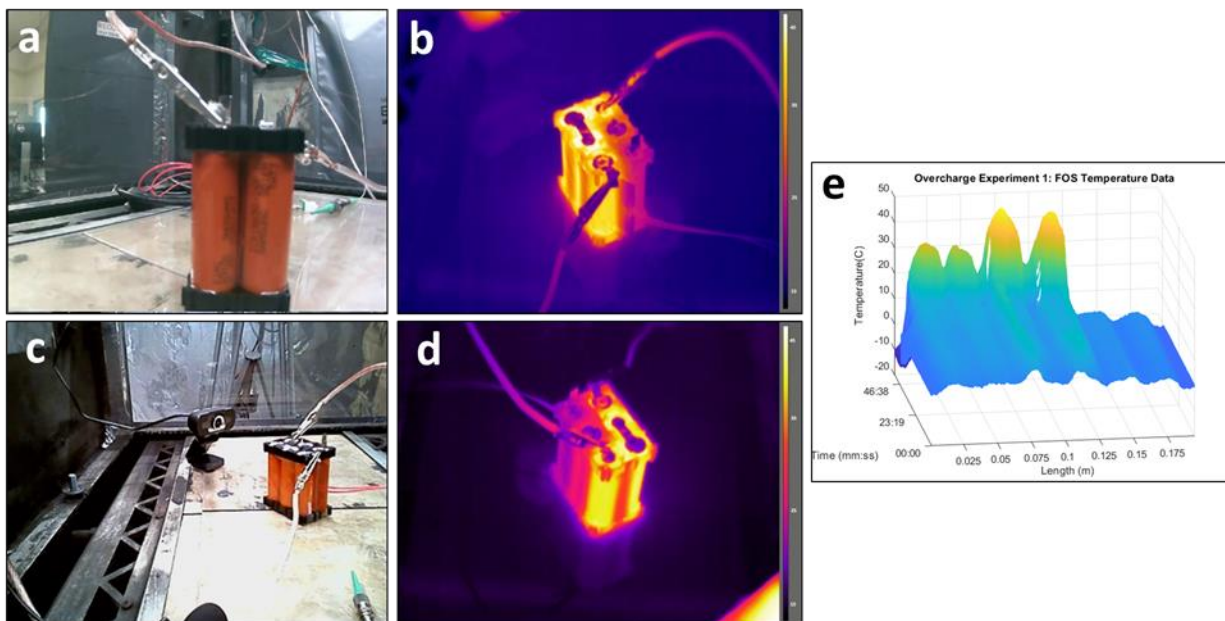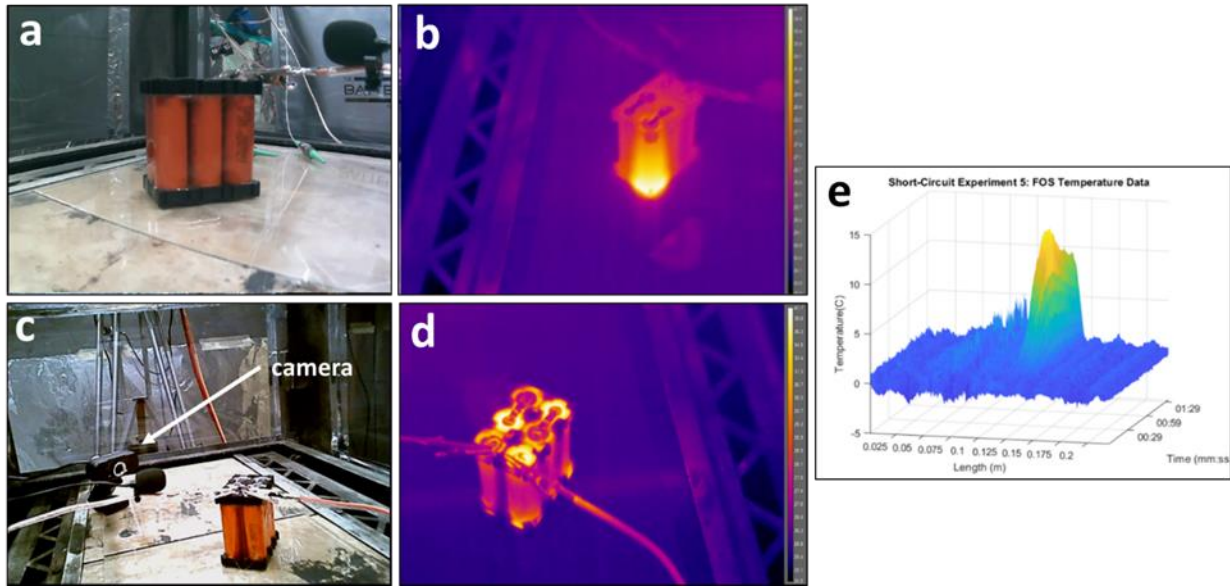
Figure 3.9. Short-Circuit Testing of a 6S/1P Module Coupled with Infrared Imaging. (a) A 6S/1P module with a taped FOS was placed inside a chamber designed for destructive experimentation. (b) Infrared imaging during a short-circuit test showed a single cell significantly increase in temperature during the course of the test. This infrared imaging was recorded by a FLIR camera located within the (c) chamber, which also recorded the rise in temperature observed on the (d) terminal connections of each of the 18650 cells.

3.6 CONCLUSIONS

Thermocouples are the traditional method for sensing temperature fluctuations within materials. However, some applications require a substantial number of thermocouples to be deployed for accurate sensing. Introducing multiple thermocouples is difficult. Multiple wires are difficult to manage, the data acquisition channels become expensive, and the conductive nature of thermocouples make them tough to insulate, especially in high voltage batteries. It has been demonstrated that a commercially available HD-FOS produces accurate and reliable thermal sensing data when applied to electrical applications and verified against thermocouples and FLIR

imaging. It has been demonstrated here that when an FOS is attached to battery modules containing multiple cells, the HD-FOS is able to sense a thermal rise within individual cells and even near the cell terminals during normal, short-circuit, and overcharge conditions. Although an FOS can be used to sense strain or temperature, only temperature results have been shown here. The fiber is cost effective, easy to install in the module, aesthetically pleasing, and is dielectrically insulated. The ability to push a digital flag to a BMS or other higher level control system has been shown, demonstrating the ability to potentially stop prevent further damage when any cell within a battery is experiencing unexpected conditions. The ability to easily identify where problems are occurring based off location-based sensing has been shown. As monitoring systems begin moving toward an Internet of Things (IoT) approach, this method of real-time data acquisition can potentially be an important addition as collected data is pushed into cloud-based systems [35].

3.7 ACKNOWLEDGMENTS

3.8 REFERENCES

[1] Nishi Y, Lithium-ion secondary batteries; past 10 years and the future, *J. Power Sources*, 100 (2001) 101-106.

[2] Bugrynieca, P., Davidson, J., Cumming, D., Brown, S., "Pursuing safer batteries: thermal abuse of LiFePO$_4$ cells," *J. Power Sources*, 414 (2019) 557-568.

[3] Z. Zhang, P. Ramadass, W. Fang, "Safety of Lithium-ion Batteries." *Lithium-Ion Batteries: Advances and Applications*, 2014.

[4] M. Sheikh, A. Elmarakbi, S. Rehman, "A combined experimental and simulation approach for short circuit prediction of 18650 lithium-ion battery under mechanical abuse conditions." *Journal of Energy Storage*, 32 (2020).

[5] P. Wang, X. Zhang, L. Yang, X. Zhang, M. Yang, H. Chen, D. Fang, "Real-time monitoring of internal temperature evolution of the lithium-ion coin cell battery during the charge and discharge process." *Extreme Mechanics Letters*, 9 (2016).

[6] Y. Gang, C. Leitao, Y. Li, J. Pinto, X. Jiang. "Real-time temperature measurement with fiber Bragg sensors in lithium batteries for safety usage." *Measurement*, pp. 3166-3172. May 14, 2013.

[7] M. Nascimento, S. Novais, M.S. Ding, M.S. Ferreira, S. Koch, S. Passerini, J.L. Pinto. "Internal strain and temperature discrimination with optical fiber hybrid sensors in Li-ion batteries." *J. Power Sources*, 410-411 (2019) 1-9.

[8] M. Nascimento, M.S. Ferreira, J.L. Pinto, "Real time thermal monitoring of lithium batteries with fiber sensors and thermocouples: A comparative study." *Measurement*, 111 (2017).

[9] G-H. Kim, A. Pesaran, "Battery Thermal Management Design Modeling." *The World Electric Vehicle Association Journal*, 1 (2007).

[10] S. Panchal, I. Dincer, M. Agelin-Chaab, R. Fraser, M. Fowler, "Experimental temperature distributions in a prismatic lithium-ion battery at varying conditions." *International Communications in Heat and Mass Transfer*, 71 (2016).

[11] H. Popp, M. Koller, M. Jahn, A. Bergmann, "Mechanical methods for state determination of Lithium-Ion secondary batteries: A review." *Journal of Energy Storage*, 32 (2020).

[12] L.W. Sommer, P. Kiesel, A. Ganguli, A. Lochbaum, B. Saha, J. Schwartz, C-J. Bae, M. Alamgir, A. Raghavan, "Fast and slow ion diffusion processes in lithium ion pouch cells during cycling observed with fiber optic strain sensors." *Journal of Power Sources*, 296 (2015).

[13] M. Arhant, N. Meek, D. Penumadu, P. Davies, N. Garg, "Residual Strains using Integrated Continuous Fiber Optic Sensing in Thermoplastic Composites and Structural Health Monitoring." *Experimental Mechanics*, pp. 167-176, September 14, 2017.

[14] S. Kreger, N. Rahim, N. Garg, S. Klute, D. Metrey, N. Beaty, J.W. Jeans, R. Gamber. "Optical frequency domain reflectometry: principles and applications in fiber optic sensing." *Proceedings of SPIE*, pp. 83-84. May 12, 2016.

[15] T. Bandhauer, S. Garimella, T.F. Fuller, "A Critical Review of Thermal Issues in Lithium-Ion Batteries." *Journal of The Electrochemical Society*, 158 (2011).

[16] E. Vergori, Y. Yu, "Monitoring of Li-ion cells with distributed fibre optic sensors." *Procedia Structural Integrity*, 24 (2019).

[17] B. Gu, M. Yin, A.P. Zhang, J. Qian, S. He, "Optical fiber relative humidity sensor based on FBG incorporated thin-core fiber modal interferometer." *Optics Express*, 19 (2011).

[18] M. Nascimento, M.S. Ferreira, J.L. Pinto, "Temperature fiber sensing of Li-ion batteries under different environmental and operating conditions." *Applied Thermal Engineering*, 149 (2019).

[19] H.L. Atchison, Z.R. Bailey, D.A. Wetz, M. Davis, and J.M. Heinzel, 'Fiber Optic Based Thermal and Strain Sensing of Lithium-Ion Batteries at the Individual Cell Level,' Journal of The Electrochemical Society, 2021 168 040535.

[20] S. Novais, M. Nascimento, L. Grande, M.F. Domingues, P. Antunes, N. Alberto, C. Leitao, R. Oliveira, S. Koch, G.T. Kim, S. Passerini, J. Pinto, "Internal and External Temperature Monitoring of a Li-Ion Battery with Fiber Bragg Grating Sensors." *Sensors*, 16 (2016).

[21] Kreger, S., Gifford, D., Froggatt, M., Sang, A., Duncan, R., Wolfe M., Soller B. "High-resolution extended distance distributed fiber-optic sensing using Rayleigh backscatter." *Proceedings of SPIE*, pp. 1-12, April 10, 2007.

[22] K. Feng, J. Cui, Y. Jin, X. Sun, D. Jiang, H. Dang, Y. Niu, J. Tan, "Enhancement of the Performance and Data Processing Rate of an Optical Frequency Domain Reflectometer Distributed Sensing System Using a Limited Swept Wavelength Range." *Sensors*, 18 (2018).

[23] S.Young, D. Penumadu, D. Foster, H. Maeser, B. Balijepalli, J. Reese, D. Bank, J. Dahl, P. Blanchard, "Smart Adhesive Joint with High-Definition Fiber-Optic Sensing for Automotive Applications." *Sensors*, 20 (2020).

[24] V. Raman, M. Drissi-Habti, P. Limje, A. Khadour. "Finber SHM-Coverage of Inter-Plies and Bondings in Smart Composite by Dual Sinusoidal Placed Distributed Optical Fiber Sensors." *Sensors*, 742 (2019).

[25] N.A.A. Rahim, M.A. Davis, L. Routhier, B. Chang, J. Chevalier, J.J. Bos, S.T. Kreger, E.E. Sanborn. "Accuracy and Survivability of Distributed Fiber Optic Temperature Sensors." *AIAA SciTech Forum*, 53rd AIAA Aerospace Sciences Meeting, January 5-9, 2015.

[26] L. Palmieri, L. Schenato, "Distributed Optical Fiber Sensing Based on Rayleigh Scattering." *The Open Optics Journal*, 7 (2013).

[27] J. Meyer, A. Nedjalkov, A. Doering, M. Angelmahr, W. Schade, "Fiber optical sensors for enhanced battery safety." *Proceedings of SPIE, Fiber Optic Sensors and Applications XII*, 2015.

[28] M. Yildiz, H. Karakoc, I. Dincer, "Modeling and validation of temperature changes in a pouch lithium-ion battery at various discharge rates." *International Communications in Heat and Mass Transfer*, 75 (2016).

[29] J. Yi, U.S. Kim, C.B. Shin, T. Han, S. Park, "Modeling the temperature dependence of the discharge behavior of a lithium-ion battery in low environmental temperature." *Journal of Power Sources*, 244 (2013).

[30] A.A. Andreev, A.G. Vozmilov, V.A. Kalmakov, "Simulation of lithium battery operation under severe temperature conditions." *Procedia Engineering*, 129 (2015).

[31] D. Bernardi, E. Pawlikowski, J. Newman, "A General Energy Balance for Battery Systems." *Journal of the Electrochemical Society*, 132 (1985).

[32] C. Campestrini, T. Heil, S. Kosch, A. Jossen, "A comparative study and review of different Kalman filters by applying an enhanced validation method." *Journal of Energy Storage*, 8 (2016).

[33] S. Zhang, X. Guo, X. Zhang, "An improved adaptive unscented kalman filtering for state of charge online estimation of lithium-ion battery." *Journal of Energy Storage*, 32 (2020).

[34] Y. Xu, M. Hu, A. Zhou, Y. Li, S. Li, C. Fu, C. Gong, "State of charge estimation for lithium-ion batteries based on adaptive dual Kalman filter." *Applied Mathematical Modelling*, 77 (2020).

[35] R. Fitzgerald, V. Karanassios, "The Internet of Things (IoT) for a Smartphone-enabled Optical Spectrometer and its use On-site and (potentially) for Industry 4.0." *Proceedings of SPIE, Next-Generation Spectroscopic Technologies XI*, 2018.

CHAPTER 4: THERMAL MONITORING OF SERIES AND PARALLEL CONNECTED

LITHIUM-ION BATTERY MODULES USING FIBER OPTIC SENSORS

4.1 MANUSCRIPT 3: BACKGROUND

The widespread deployment of lithium-ion batteries in various consumer and industrial applications has spurred the need for continuous monitoring to prevent potentially catastrophic outcomes caused by thermal runaway or external factors. Traditional methods of using thermocouples and thermistors to monitor temperature are limited in use since temperature is only recorded from discrete points in the battery system. Implementing more points of measurement creates a more complete picture of temperature data but at a higher cost of implementation and the requirement for additional measurement channels. Technologies, such as fiber optic sensors, have been proposed for replacing thermocouples or expanding measurement channels without the downside of decreased data throughput. These fiber sensors measure both the temperature and applied stresses to the glass fiber whether it be through heat or strain from an attached surface. One fiber can represent multiple thermocouples or strain gauges and can provide multiple measurement points. This approach enables precise monitoring along the length of the fiber creating a space of data much larger than what could be achieved with traditional electrical measurements. Additionally, this fiber can be daisy chained wherein the total length of one sensor can replace all thermocouples used for a battery management system. Moreover, these fiber sensors in combination with microphones can correlate and determine the onset of fault conditions with rudimentary data fusion. The application studied here explores the capabilities of monitoring thermal data of battery systems, which presents an advancement in ensuring the safe and effective operation of energy storage.

4.1.1 MODIFICATIONS TO MANUSCRIPT FOR INCLUSION IN DISSERTATION

4.2 ABSTRACT

Lithium-ion batteries are widely deployed in commercial and industrial applications. Continuous monitoring is necessary to prevent destructive results that can occur due to thermal runaway. Thermocouples and thermistors are traditional sensors used for thermally monitoring cells, modules, and batteries, but they only sense changes at the physical point where they are deployed. A high density of these sensors within a module or battery is desirable but also impractical. The study documented here shows that a commercial grade fiber optic sensor can be used as a practical replacement for multiple discrete thermocouples or strain gauges for battery, to monitor a cell, module, or battery at millimeter resolution along the fiber length. It is shown here that multiple fiber optic sensors can be series connected to allow for monitoring of a battery consisting of more than one module. In addition, it is shown that the same type of fiber can also be used to identify the onset of fault conditions by correlating the response in a fiber optic sensor suspended close to the module with an audible signature detected by a microphone at the time of

66

failure. Early detection and identification of abnormal cell operation is demonstrated within batteries employing many cells.

4.3 INTRODUCTION

Since the original lithium-ion battery was developed by J.B. Goodenough in the 1980s [1], portable batteries have become widespread in countless consumer and industrial products. New technologies are being developed every day, and as a result there are many different battery form factors and chemistries employed commercially. Each form factor and chemistry offer its own advantages and disadvantages to the application it is intended to be used in. High energy density and power density is always desirable but is not without costs [2]. Noted failures, such as the Samsung Galaxy Note 7, demonstrate that lithium-ion batteries are susceptible to random catastrophic events and measures must be taken to prevent these occurrences [3].

Batteries experience a change in temperature and strain at the time of a failure [4]. Temperature measurements may be acquired using surface mounted or embedded thermocouples or thermistors. Strain measurements may be acquired using strain gauges [5]. These types of sensors are 'single point' measurements, intrusive, and are often electrically conductive, sometimes inhibiting high quality thermal and strain measurements from being made where they need to be. Promising results have recently been made using optical fibers to measure temperature and strain when applied to batteries and various other applications [3, 6-10, 15, 16]. High-density fiber optic sensors (HD-FOS) exploit Rayleigh backscatter along with the natural non-homogeneities inherent in the inception of the fiber to correlate either temperature or strain to areas within the fiber [4, 8]. The Luna Optical Distributed Sensor Interrogator (ODiSI) system can measure temperature or strain from HD-FOSs but not both simultaneously [15, 16]. Temperature

measurements are recorded by attaching the fiber to the cell(s) surface in a way such that it is thermally contacting the cell(s) but only loosely mechanically contacting the cell(s) being measured so that strain is decoupled. Encasing the fiber in a thin Teflon tube or in tape like that seen in Figure 4.1 (a), discussed later, have provided successful results. Strain measurements are recorded by attaching the fiber to the cell(s) surface in a way such that it is mechanically contacting the cell(s) but only loosely thermally contacting the cell(s) so that it is thermally decoupled.

Advancements in this technology have allowed users to measure with a spatial resolution of less than 1 mm for fiber lengths as long as 50 m [4, 11, 12]. When used in a battery application made up of many modules connected in series/parallel, it is not feasible to use one long fiber or to use a dedicated fiber and data sensing channel for each module. Instead, it is proposed that the optical fibers be kept at manageable lengths, installed in each individual module, and then coupled together externally to create a single, longer fiber that can be measured using a single data channel. Each optical coupler introduces some signal loss and it is critical that this be well characterized and understood to ensure that data reflected from modules further down the length of the fiber is accurate. Measurements performed here have shown that the loss is manageable for an excess of ten fiber couplers before it becomes concerning.

In addition to a change in temperature and strain, batteries also produce a pressure gradient at the time of failure due to the ventilation of gasses from the cell. When this occurs, there are usually several audible signals attributed to the destruction of the integrity of the cell. As will be shown here, this audible signal can be detected by a microphone and correlated to a change in strain detected by a closely suspended FOS occurring at the time of failure, providing further indication and prediction of potential failure by a battery monitoring system [13, 14].

In this study, a Luna ODiSI system coupled with an HD-FOS is used to measure the thermal change induced in multiple battery modules, each of which is instrumented with its own optical fiber, that are coupled together using optical connections. Thermocouples are also used as a comparison to the fiber optic measurements. Because it has already been shown at the cell level, and because demonstration of successful thermal measurement from multiple modules implies that strain measurement will work as well, no experiments are performed here in which strain on individual cells is measured during normal or abnormal operation. In a few of the later experiments, a microphone is placed close to the battery to detect the occurrence of an audible signal and a fiber optic sensor is also placed nearby to detect vibration or movement caused by the acoustic waves. The signals detected from the microphone and fiber optic sensor are correlated with each other to determine the sequence of events and associated strain deformation happening at the time of battery failure. The result is a new, non-intrusive technique for making high density, real-time battery temperature measurements and for quickly identifying unexpected events more reliably than traditional techniques afford.

4.4 PROCEDURE

Previous experiments have shown the efficacy of FOSs as capable measurement devices in applications of thermal and strain sensing [15, 16]. Previous experiments studying their use in battery sensing has utilized independent fibers on individual cells or modules consisting of six to ten cells [15, 16]. Expansion of previous work is performed here using arrangements of both four and ten individual modules electrically connected in series. Making a real-time thermal or strain measurement on every cell would require large numbers of thermocouples, thermistors, or stain gauges, respectively. This creates a wiring mess and requires a high data acquisition channel count

69

for each measurement type. Instead, a single, noninvasive FOS can be installed in each module such that it thermally or mechanically contacts each individual cell and optical couplers can be used to interconnect all the modules together forming a single fiber. A single optical data acquisition channel is required to measure the expanded fiber and every cell is monitored for temperature or strain, not both simultaneously on the same fiber, in a seamless manner. In the work documented here, the methods used to install the fiber onto the modules will be discussed, the method used to locate the segments of the fiber contacting each cell will be shown, the expected loss from introducing multiple fiber optic connectors will be shown, and the fiber optic measurements recorded during a series of normal and abnormal operational conditions will be presented. Noise introduced by multiple fiber optic connections is also discussed, with estimates on the number of modules that can be interconnected before the combined loss from connectors interferes with sensor detection.

4.4.1 MODULE DESIGN AND POINT OF INTEREST DETECTION

Figure 4.1 (a) shows the method of implementation for FOS temperature sensing using a single 1.25 m long fiber that touches each of the respective 18650 cells that make up the 1S/6P or 6S/1P module, oriented in a sinusoidal arrangement between two polyimide adhesive strips. Previous studies have shown that a fiber arranged in a sinusoidal pattern reduces overall strain on the fiber and allows every cell within the module to be sensed by the fiber along its longitudinal axis [16, 17]. Figure 4.1 (b) shows a FOS directly attached to a module, and Figure 4.1 (c) shows the application of the taped fiber from Figure 4.1 (a). Measurement of each individual modules' fiber requires either its own dedicated optical measurement channel or each subsequent fiber must be connected to the previous one to form one fiber that can be sensed using a single channel. The

70

latter method is being studied here by interconnecting many of these same module types in either series or parallel. A four-module setup is shown in Figure 4.1 (d), and a ten-module setup is shown in Figure 4.1 (e).
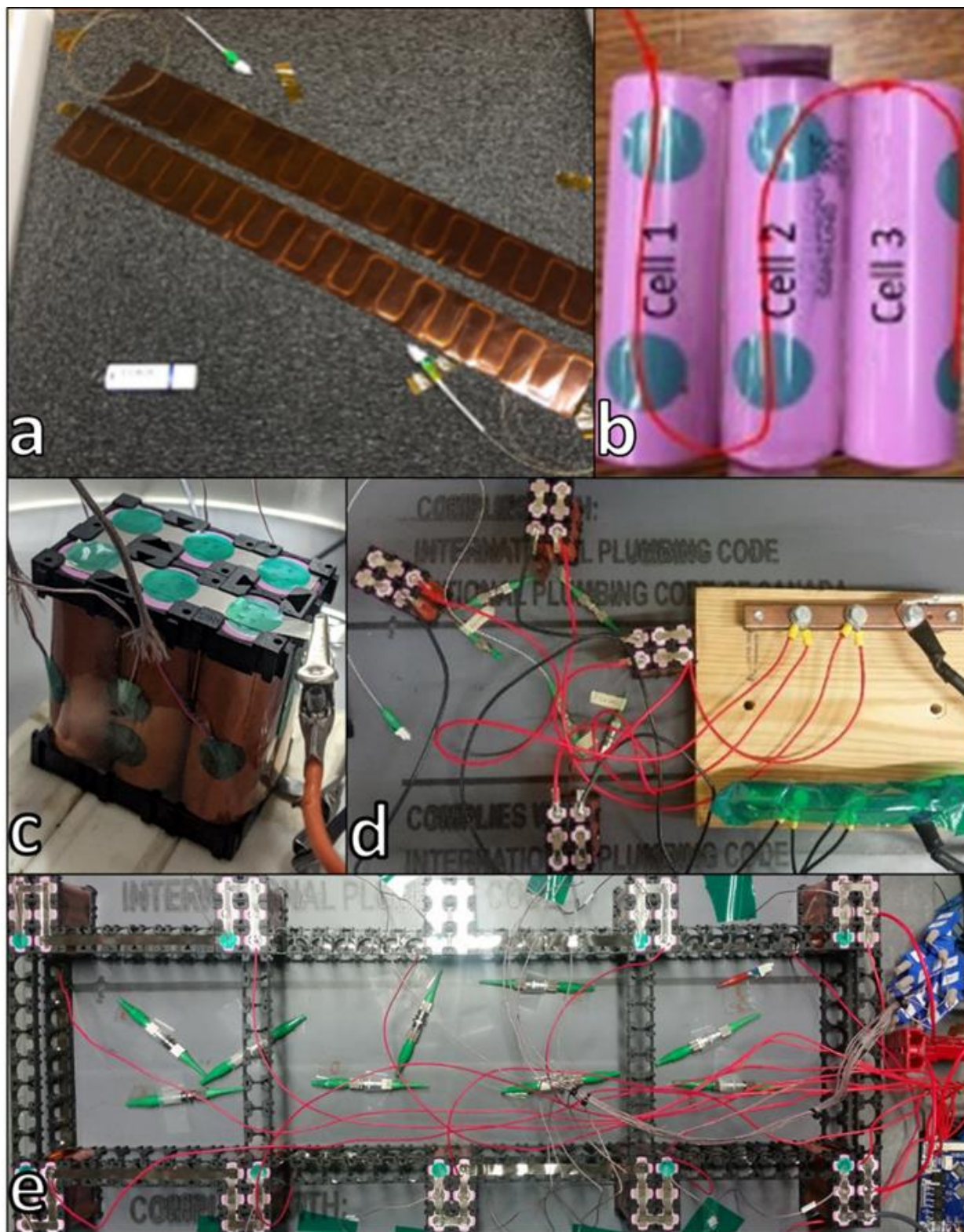
Figure 4.1. Photographs Describing the Setup of FOSs on Multiple 18650 Lithium-ion Battery Modules. In (a) a Luna FOS attached between two pieces of polyimide tape and it is

arranged in a sinusoidal pattern contacting each cell for strain reduction on the fiber as shown in

(b and c). In (d and e) multiple modules that each have their own FOSs interconnected are

shown.

The Luna data acquisition system can acquire thermal or strain data, but not both

simultaneously, from the fiber at sample rates as high as 250 Hz with spatial resolution as fine as

0.54 mm down the length of the fiber, with higher sampling frequencies possible at larger spatial

resolutions. The segments of fiber in contact with the axial length of each cell are of interest and

parsing that data out in real-time greatly simplifies the data collection and analysis process. Once

installed on the battery, the locations where the fiber optic sensors contact each respective cell

must be identified manually or by using some sort of automated process. As shown in Figure 4.1

(a), there are many segments on the fiber that are not contacting any portion of a cell and those

must be removed from the data array. Using the manual touch to identify feature would be very

time consuming and impractical on larger commercially procured batteries in which the fiber is

installed prior to procurement. Here, a custom NI Virtual Instrument (VI) has been written using

LabVIEW to autonomously detect the segments contacting each respective cell while the battery

is cycled at a low C rate. Once assembled, either individually or interconnected together, the

module(s) under test is discharged and recharged at a 0.5C rate while the custom VI is executed.

While the battery is cycled, the fiber optic sensor measures the thermal rise on each cell that stems

from its respective thermal losses and those appear as peaks in the data. The front-panel of the

custom VI is shown in Figure 4.2 (a) for a simple scenario of a single fiber on a single cell. Figure

4.2 (b) shows the data measured across the cell where the two terminals of the cell, the points

where the cell gets hottest, are autonomously identified. These locations are set as the bounds of

73

the cell and the data measured between those bounds is the valid data considered by the battery monitoring software. This same process is used to identify each cell in a multi-cell module or battery. Figure 4.2 (c) shows the same procedure applied to the 4S/6P module from Figure 4.1 (d), with 22 of the 24 cells identified, with the last two unable to be acquired due to an issue with the data file. This issue was resolved in Figure 4.2 (d), with all 60 cells successfully identified for the 10S/6P module shown in Figure 4.1 (e). This method can be utilized for a battery consisting of any arrangement of cells so long as the data loss across couplers is not significant, something better described later.
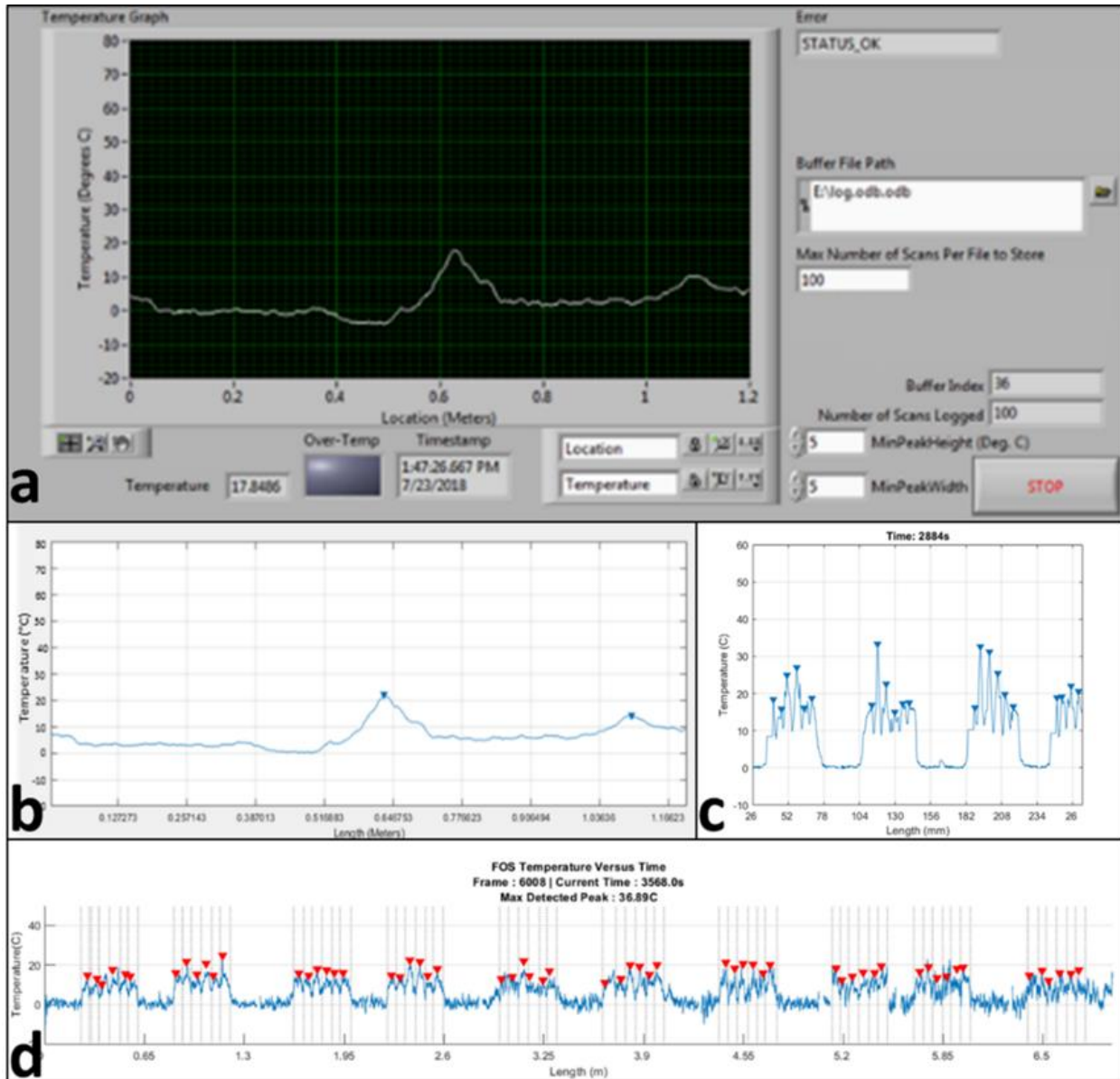
Figure 4.2. LabVIEW VI Used for Peak Detection. (a) Front panel of the LabVIEW VI used

to control the detection of peaks within a FOS connected to a battery module consisting of

multiple cell terminals. The peaks located on the temperature graph identify these terminal

locations. (b) Additionally, MATLAB was used for peak detection in real-time due to its superior

graphical features. The same battery module shown in the LabVIEW VI front panel is also

shown in the MATLAB live plot to demonstrate the ability of MATLAB to duplicate identical

results. (c) This was then applied to the 4S6P multiple module system consisting of multiple cells per module. (d) Procedure applied to the 10S6P module array.

4.4.2 MULTIPLE INTERCONNECTED MODULE COMMISSIONING EXPERIMENTS UNDER NORMAL OPERATION

It has been shown in previous work that the FOS technology discussed here can be used to measure cell temperature during normal cycling operation and that it can be used to detect abnormal operating conditions, such as short circuits and over-charge events [15, 16]. During these abnormal events, either high rates of temperature change, dT/dt, or high rates of strain change, dS/dt, can be measured and identified depending on how the fiber is coupled to the module. Of interest here is if that same type of detection can be made when multiple modules are connected in series and the FOSs on each of those modules are interconnected using couplers. Data loss across the couplers was of concern and something that needed to be measured and validated. To validate that this would even work under normal operation, an initial experiment was performed using four already made 1S/6P modules that had 1.25 m long FOS sensors installed on them. The modules were connected serially as seen in Figure 4.3, the fibers were interconnected using fiber optic couplers, and the single 4S/6P battery was cycled electrically while measuring the FOS data using a single ODiSI channel. A thermocouple was attached to one cell within each module and those were used to verify the accuracy of the FOS temperature data. The following electrical cycling procedure was performed:

1. 1C constant current/constant voltage (CC/CV) charge to 100% state of charge (SOC)
2. 1C constant current (CC) discharge down to 0% SOC
3. 1C CC/CV charge to 100% SOC

4. 2C CC discharge to 0% SOC (datasheet maximum recommended discharge rate)

5. 1C CC recharge to 100% SOC

In Figure 4.3 (a), a plot of the optical signal recorded across the four modules is plotted. The five high spikes are the optical distortion that occurs across the couplers used to interconnect the four modules together. Notice that the amplitude of the signal linearly decreases along the fiber length. This is the expected loss that needs to be characterized to understand the limits of how many fibers can be practically connected in a higher voltage battery. In the case of these four modules, the loss is roughly 5 dB which is well within the device's measurement tolerance. In Figure 4.3 (b), the thermal rise on each cell is clearly visible when cycled under the electrical conditions shown in Figure 4.3 (c).
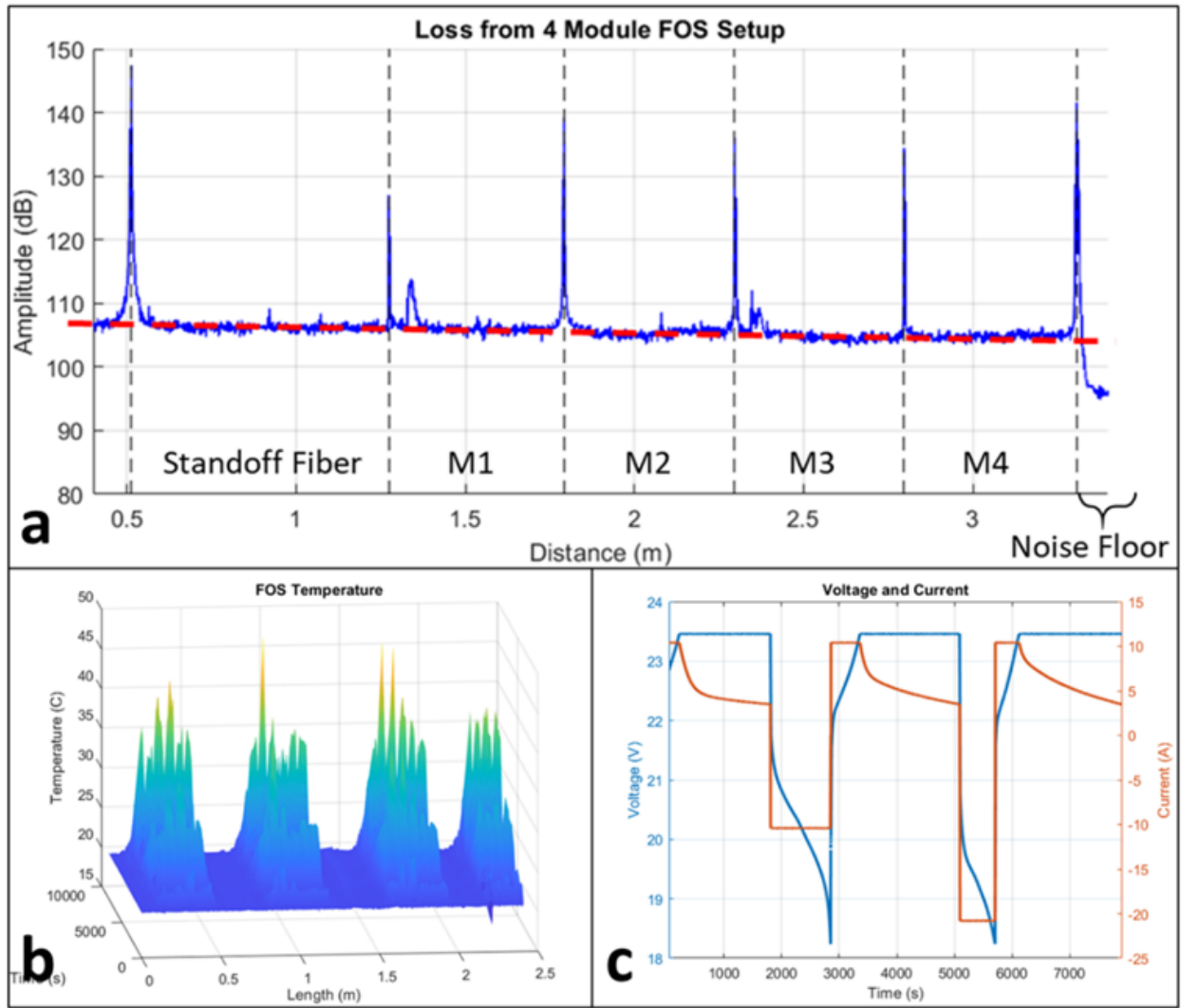
Figure 4.3. Four Module Loss and Temperature. (a) Noise loss versus distance along the FOS. Regions are identified by a peak in noise, caused due to added reflections from fiber optic connectors. (b) Isometric view of FOS data as a function of fiber Due to an issue with the sensor file, the last two cells of module 4 were unable to be plotted. (c) Plot of voltage and current from the outlined procedure.

Expanding upon the four-module design, a 10S/6P battery was constructed, previously shown in Figure 4.1 (e). A thermocouple is attached to one cell within each module, in addition to the FOS, and the temperature is recorded by the NI data acquisition system. Figure 4.4 (a) shows

the noise loss for the 10-module setup, with a noticeably steep trend like that in Figure 4.3 (a).

There is roughly 8 dB of loss dropped across the 10 modules, but the amplitude is still within the

tolerance of the data acquisition. It is expected that at least four additional connectors can be

introduced without reaching the noise floor, which would prevent the ODiSI device from properly

detecting the termination of the FOS. The main cause of additional noise was due to the multiple

fiber optic connectors, with the length of the fiber contributing much less to the overall noise in

the system. Figure 4.4 (b) shows raw data obtained from the ODiSI system, with noise clearly

visible around the fiber optic connection points. Figure 4.4 (c) shows the smoothed FOS data, with

regions around fiber optic connectors set to NaN for better identification of cell temperatures on

the surf plot. Figure 4.4 (d) shows individual module voltages reported from the BMS, while

Figure 4.4 (e) shows the total voltage and current reported by the charger/load. The following

electrical cycling procedure was performed:

1. 0.5C CC/CV charge to 100% SOC

2. 0.5C CC discharge down to 20% SOC

3. 0.5C CC/CV charge to 100% SOC

4. 1C CC discharge to 20% SOC

5. 0.5C CC recharge to 100% SOC
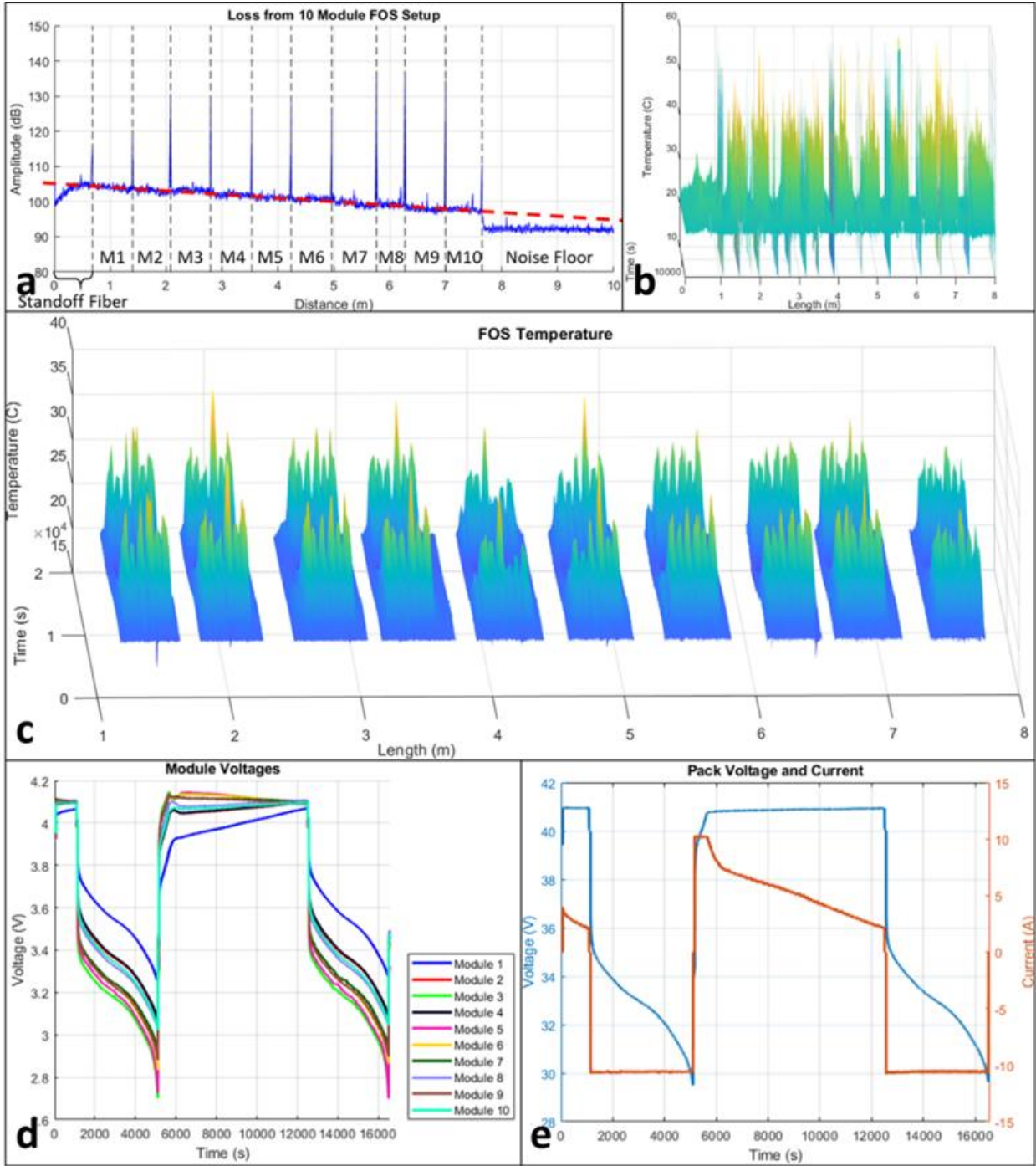
Figure 4.4. Ten Module Loss and Temperature. (a) Noise loss from ten module system. The trend is more pronounced than from the four-module system, with an estimated four additional modules able to be added before conflict with the noise floor, for a total of 14. (b) Isometric view of raw thermal data from the cycling of four connected modules. This had notably more noise

than the four module data and needed to be smoothed. (c) Isometric view of smoothed data, with data around fiber connections set to NaN for visibility. (d) Individual module voltages reported by the BMS. (e) Total voltage and current reported by the charger/load.

4.4.3 MULTIPLE INTERCONNECTED MODULE COMMISSIONING EXPERIMENTS UNDER ABNORMAL OPERATION

Temperature changes during normal operation of battery modules are typically predictable and differ greatly from abnormal events, such as an overcharge or short-circuit. A BMS can be connected so that it disconnects the battery from a charger or load if a fault condition is observed but if the density of thermal measurement is not high enough, an unexpected event can easily be missed. It is shown here that the HD-FOS can detect the rate of temperature change and act if it is higher than what is normally expected anywhere throughout the battery. Further, it is easy to identify where the unexpected measurement is occurring. In the experiment highlighted next, the 10S/6P battery was discharged at a 0.5C rate. Towards the end of the discharge, a controlled short-circuit is performed on only one module while the temperature is recorded using both thermocouples and the fiber-optic sensor. Figure 4.5 (a) shows the collected FOS data, with regions around fiber optic connectors set to NaN for better identification of cell temperatures on the surf plot. Figure 4.5 (b) shows the voltage and short-circuit current from module 6, which was the module that was shorted during the discharge. Figure 4.5 (c) shows the voltages reported by the BMS for all ten modules, and Figure 4.5 (d) shows the pack voltage and current reported by the BMS. Notice from the data in Figure 4.5 (a) that temperature deviations measured around the 5 m mark are very high relative to the rest of the module. This correlates to module 6 and this is easily detected by the LabVIEW VI.
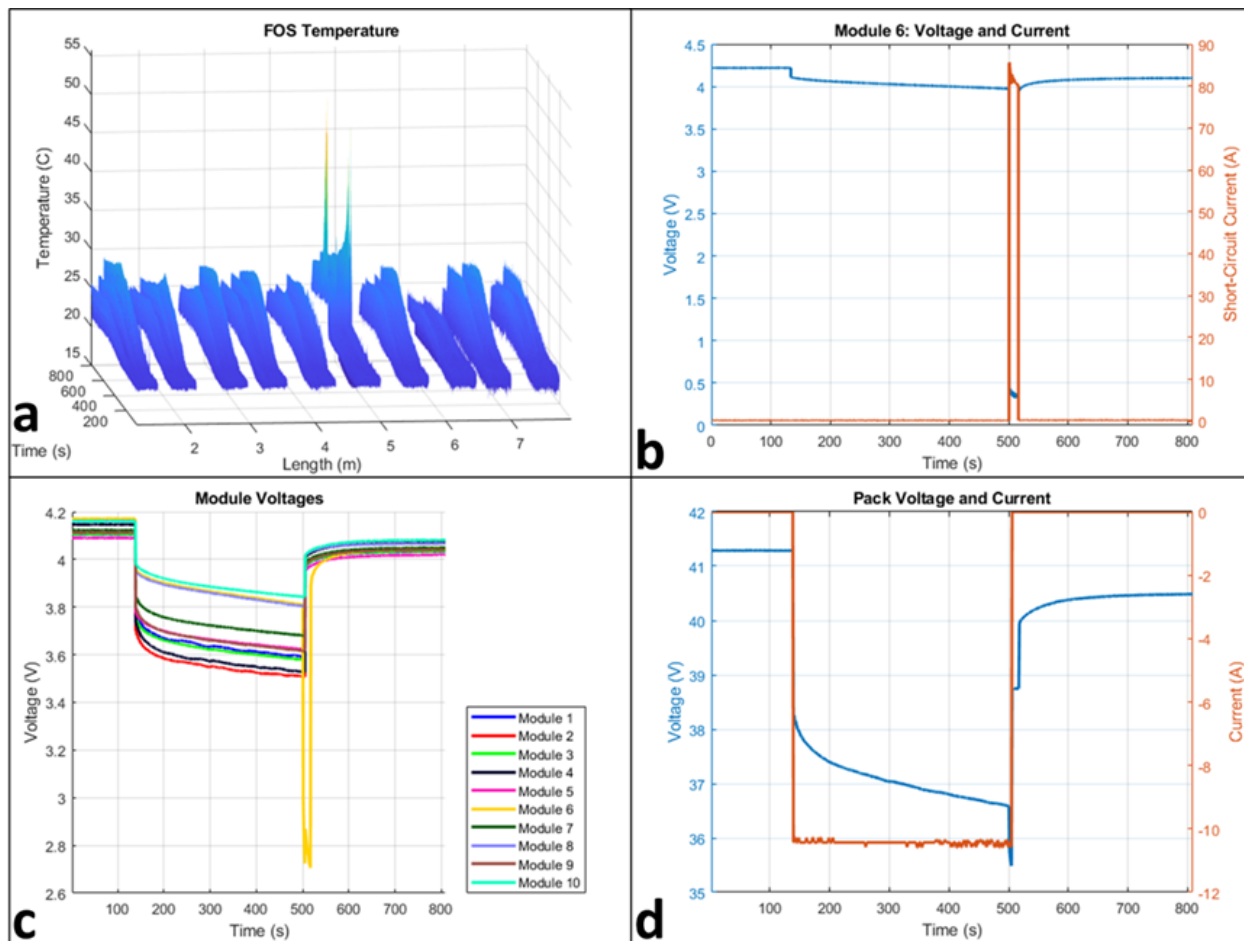
Figure 4.5. Single Module Short-Circuit in Ten Module System. (a) Isometric view of smoothed data, with data around fiber connections set to NaN for visibility. Sections of this data correspond to the module number (1-10), from left to right. (b) Voltage and short-circuit current measured from module 6, which was shorted during the discharge. (c) Individual module voltages reported by the BMS. (d) Total voltage and current reported by the charger/load.

4.4.4 ACOUSTIC MEASUREMENT USING A FOS

Along the way, the question arose as to whether a FOS would produce a measurable signature induced by the acoustic wave given off when a lithium-ion cell goes into thermal runaway. In this case, a fiber should be suspended close to the cell/module but not be in any contact

with it. To observe this, multiple experiments were devised to detect and verify the reaction from the FOS can be correlated to an acoustic signature. For the first experiment, an 18650 cell was instrumented with a FOS in three different configurations: taped to the body of the cell, glued to the body of the cell, and suspended a distance away from the cell as shown in Figure 4.6 (a) and (b). Following this, an overcharge is subjected to the cell, with the intent of triggering the CID, which typically has an audible "pop" sound. This first experiment did show variance in the different methods of strain measurement, but did not provide much of an indicator to the acoustic event. This was resolved by suspending the FOS at various heights with additional slack added. Additionally, JB-Weld is injected into the cap of the cell to prevent its own internal current interrupt device (CID) from engaging during the overcharge, in addition to a silicon heating pad wrapped around the cell to force thermal runaway. For the subsequent experiments, the cell and FOS are placed in a metallic drum during destructive testing along with a microphone and a remote video capture device (USB camera). The FOS is suspended above the cell in a few different passes as seen in the experimental setup illustrated in Figure 4.6 (c) and (d). To verify that strain changes in the suspended fiber are decoupled from the changing ambient temperature from the heated cell, a thermocouple is placed on the cell to record temperature data. LabVIEW is used to control the acquisition of the FOS data, voltage, and current measurements and Open Broadcaster Software (OBS) operating within the LabVIEW VI is used to record video from the USB camera. Video acquisition from the OBS is initiated and halted by keyboard strokes within LabVIEW to ensure the individual audio and video data are triggered at the same time. The LabVIEW VI is programmed to charge the cell at 3.2 A and power the patch heater until the cell is overcharged and thermal runaway failure is achieved.
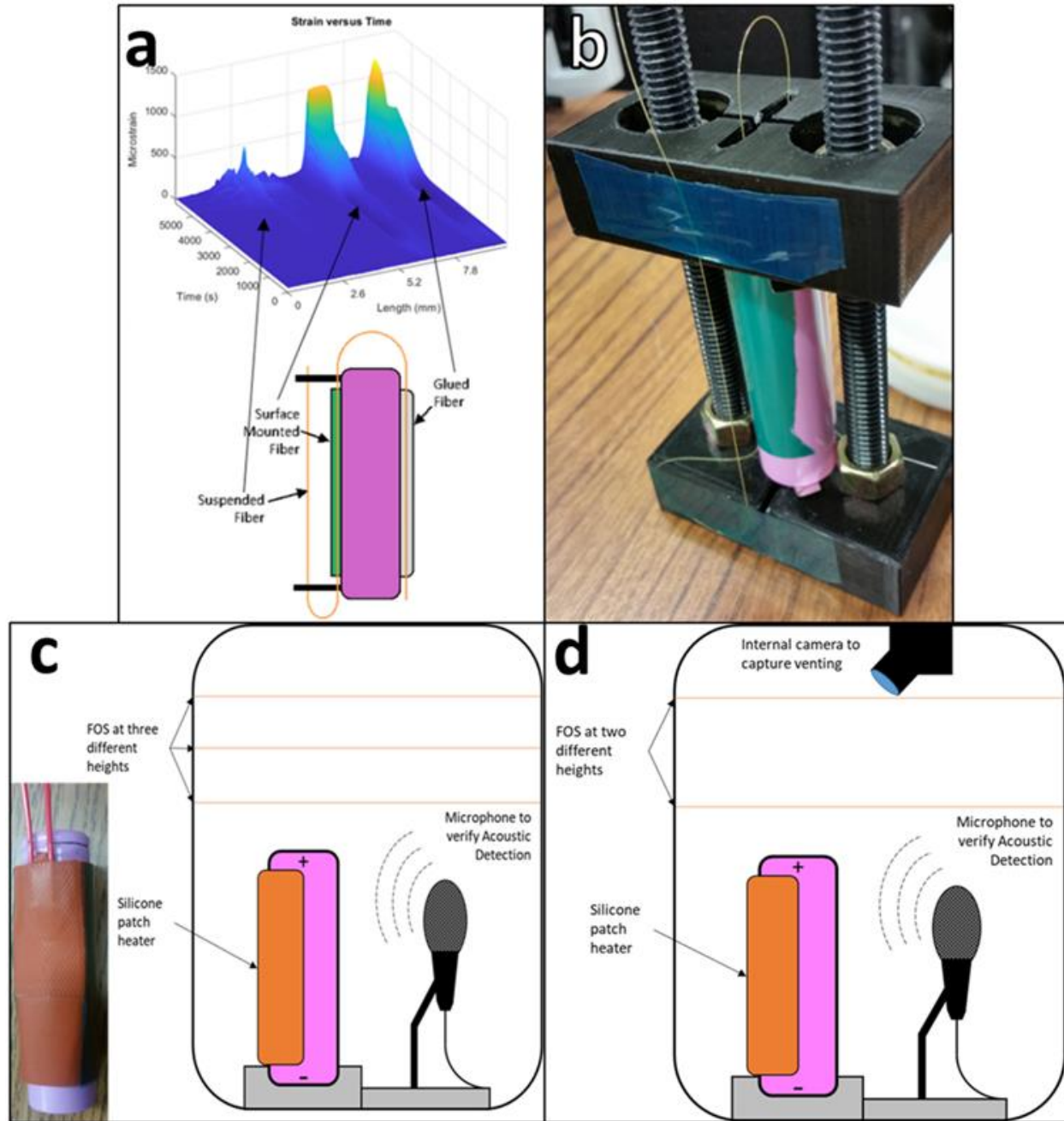
Figure 4.6. Acoustic Detection with a FOS. (a) Experimental design reflecting the placement of

an FOS in relation to a cell and the expected strain measurements when the fiber is taped or

glued to the cell or suspended away from the cell body. (b) This cell is placed in a custom-built

3-D printed case and placed in a (c) container designed for destructive testing. (d) Test is

conducted with a FOS suspended in the container along with a microphone and camera to verify

and correlate vibrations detected by the fiber to an acoustic signature or visual confirmation of cell failure.

Destructive overcharging experimentation was also extended to study a 6S/1P module of 18650 cells, similar to the module design shown previously in Figure 4.1 (c). For this experiment, the module was also heated during the overcharge process. A USB webcam was used to capture video data and a microphone was used to capture audio data during the destructive test. Experimental data and images from the video recording will be discussed in the results section.

4.5 RESULTS AND DISCUSSION

4.5.1 TEMPERATURE MEASUREMENT DURING NORMAL OPERATION

An expanded presentation of the thermocouple and FOS plotted in Figure 4.3 is presented in Figure 4.7. The data collected from each respective module of six cells is plotted in its own sub-plot and each discharge and recharge phase of the experiment are bounded with dashed lines. Comparison of the temperatures measured by the thermocouples and the FOS is shown. The FOS data deviates around 5℃, with a larger deviation between thermocouple and FOS data. This is expected when considering the different thermal masses of the thermocouple versus the FOS and the different placements on the cell. The thermocouple, whose tolerance is ±2℃, is placed near the cell terminal which is the hottest location, and the FOS is an average temperature measured along the full length of the cell. The spread among cells is within the tolerance of the FOS and expected with the varying air flow around the cells in an open-air environment. The temperature variation measured is a good justification for why an FOS is advantageous over single point

measurements made. The FOS allows for hot spots to be identified and abnormal operation to be quickly observed anywhere in the multi-cell battery.
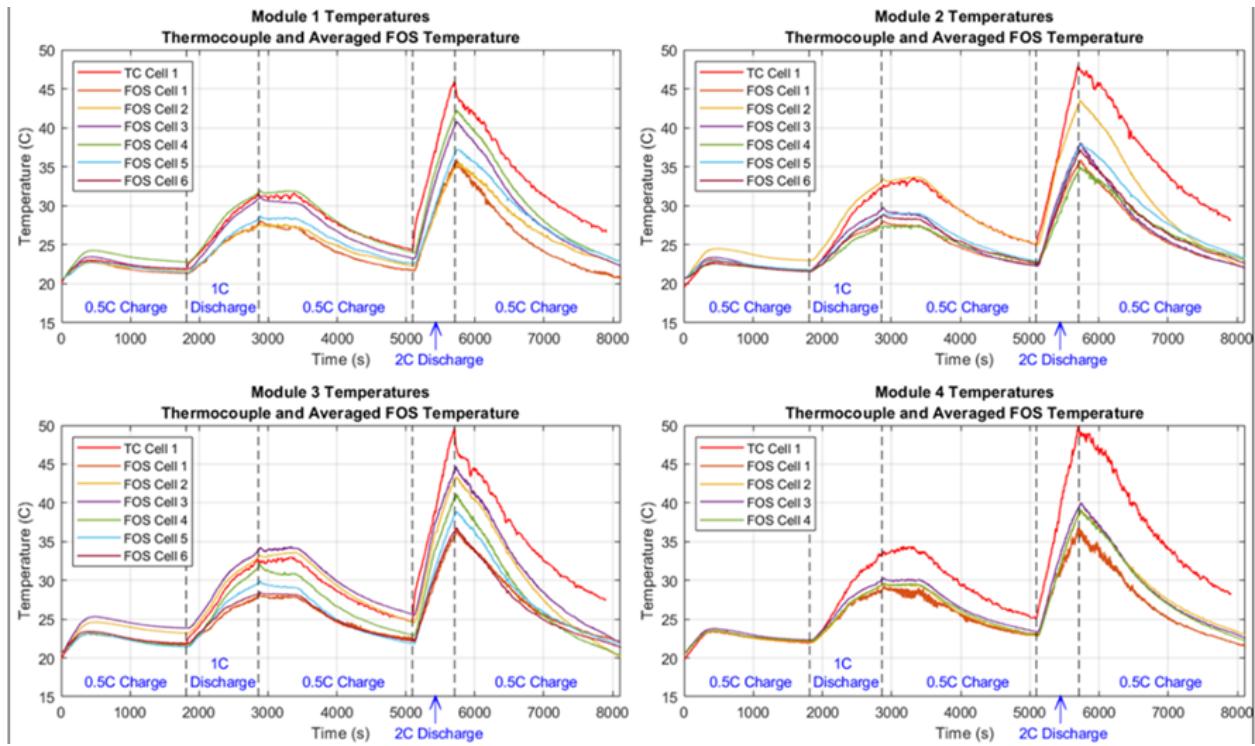
Figure 4.7. Normal Operation of a Four Module System. The temperature data acquired during cycling is plotted as a function of time, with a comparison of Thermocouple and FOS data for each cell. The last two cells in module 4 are missing due to an issue with the sensor file not reading the full fiber.

Expanded FOS and thermocouple data collected from the 10S/6P module during normal operation, shown earlier in Figure 4.4, is plotted in Figure 4.8. As in Figure 4.6, there is expected variance in data, again limited to around 5°C. It should be noted that additional noise was observed on the thermocouples on modules 2 and 5. It is unclear why this occurs and again highlights the advantages of non-conductive, noise immune FOS diagnostics. Similar to the four-module setup, thermocouple temperatures were higher due to placement on the cell terminal, versus averaged

temperature along the length of the cell. Though there is some disagreement, this shows a good correlation between thermocouple data and FOS data, similar to previous experimentation [15, 16].
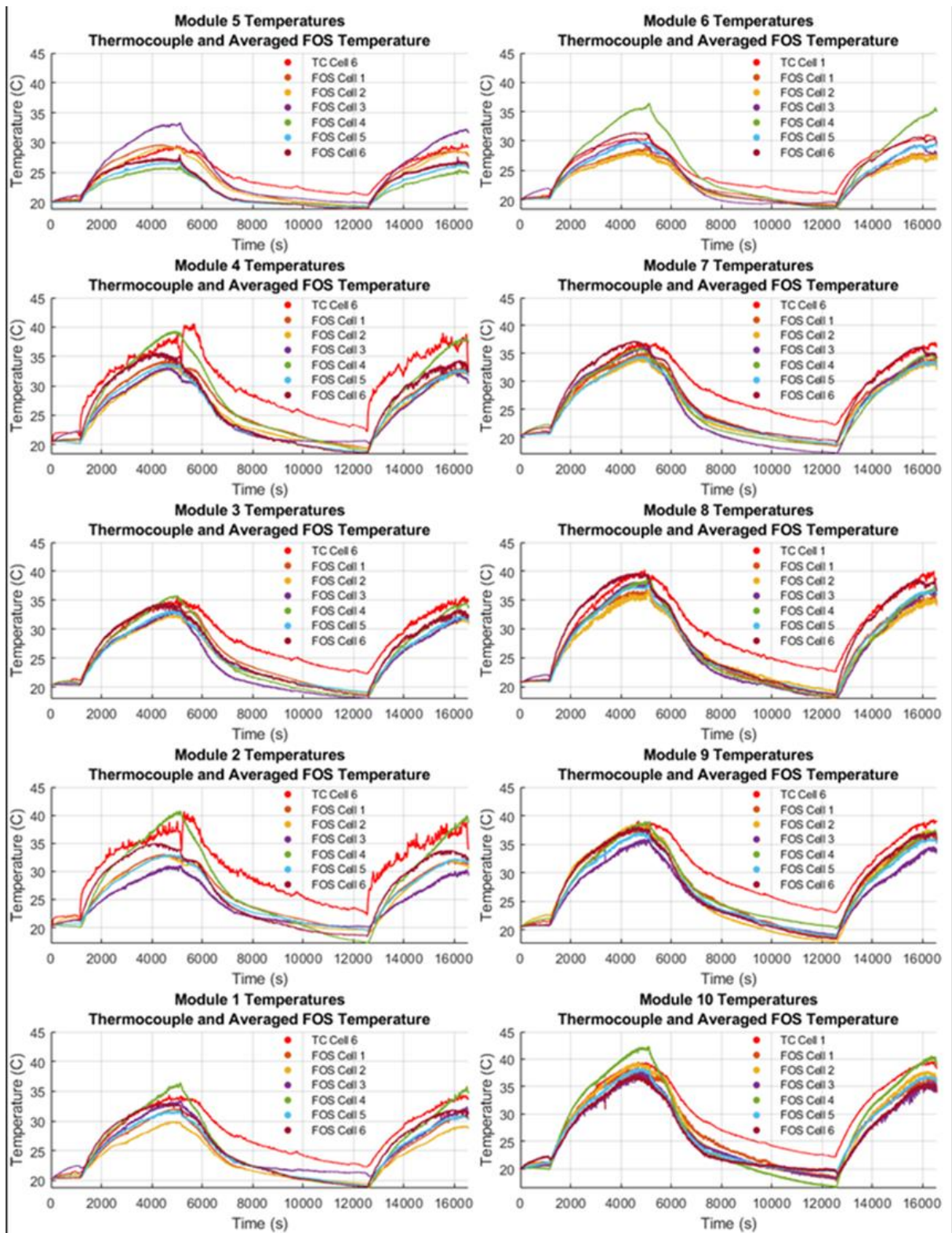
Figure 4.8. Normal Operation of a Ten Module System. Measured temperatures from both the

FOS and thermocouple during normal operation of the 10S6P module. The figure is oriented in

such a way that the bottom left plot is the first module, and the bottom right plot is the tenth module, which is identical to the electrical connection shown in Figure 4.1 (e).

To provide a baseline for abnormal operating conditions, the change in temperature over change in time (dT/dt) was calculated using both the thermocouple and averaged FOS data on each module. Figure 4.9 (a) shows the dT/dt measurement (orange) for each thermocouple (blue) on the 10S/6P battery, while Figure 4.9 (b) shows the dT/dt measured (orange) using the averaged FOS data (blue) from each six-cell module. For both Figure 4.9 (a, b), the red plot represents a flag that can be sent to a BMS if the rate of temperature change exceeds a preset limit. For normal operation, the trigger level was set at 0.1°C/s. This value was chosen to ensure no flags were generated during normal operation, while still generating flags during abnormal operation, shown in later in Figure 4.11.
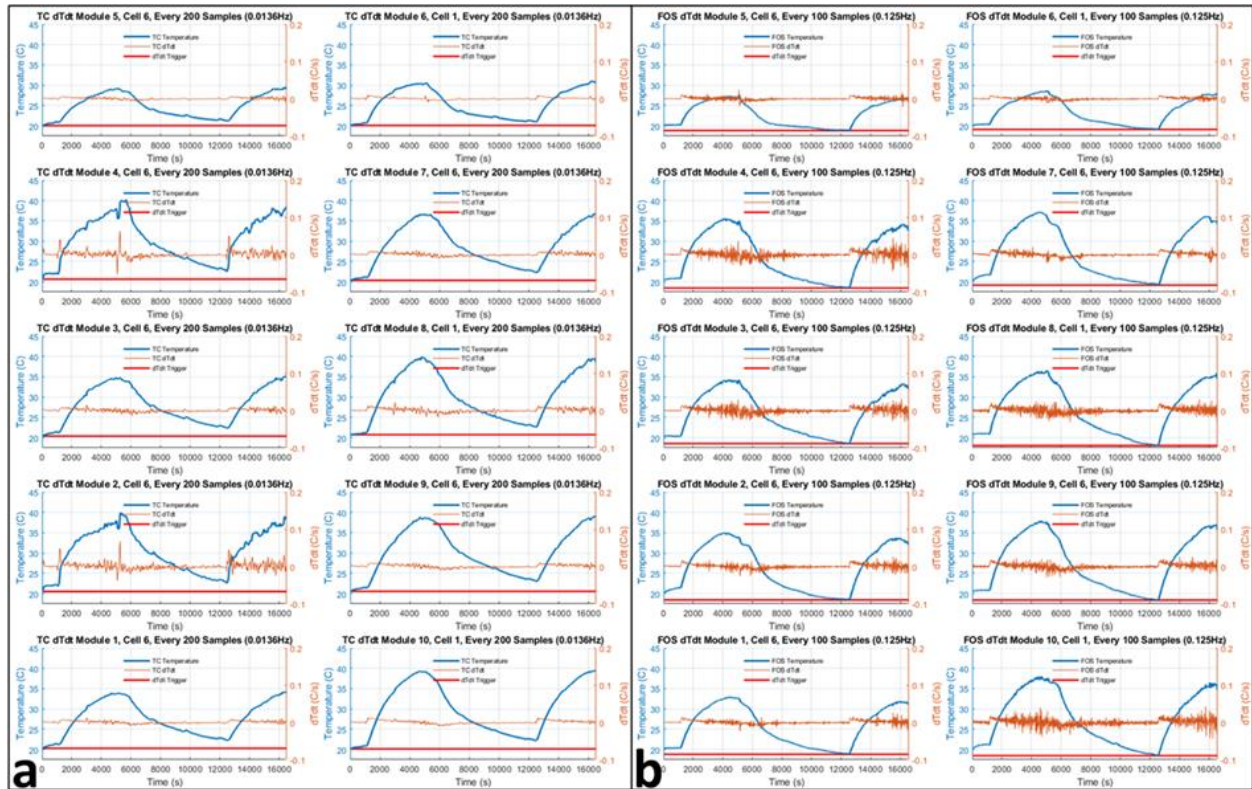
Figure 4.9. Thermocouple and FOS dT/dt During Normal Operation. (a) Thermocouple dT/dt during normal operation of the 10S6P module. (b) FOS dT/dt during normal operation of the 10S6P module.

4.5.2 FOS USE DURING ABNORMAL OPERATING CONDITIONS

Abnormal or failure conditions within battery operation are preempted by a sudden rise in temperature or increase in dT/dt. The 10S/6P module was subjected to a 0.5C discharge, and similar to normal operation, a single thermocouple was attached to each module. To emulate an abnormal event, a Ross relay was connected to Module 6, so that this module could be manually shorted in a controlled manner. This short-circuit should also correspond to a large increase in temperature, which would show a rapid change in dT/dt, independent of temperatures measured from the other nine modules during the 0.5C discharge. FOS data along each module, in addition

90

to cell voltages and short-circuit current, was previously shown in Figure 4.5. The measured temperatures for both the FOS and thermocouples are shown in Figure 4.10. Figure 4.10 (a) shows averaged FOS data for each cell in addition to thermocouple data and Figure 4.10 (b) shows only averaged FOS data for the cell the thermocouple is on. Exceptionally good correlation of FOS and thermocouple temperatures is observed in modules 1, 3, 5 and 6 while there is expected deviation shown in the remaining modules. Individual change in cell thermocouple temperatures, dT/dt, are shown in Figure 4.11 (a). Figure 4.11 (b) shows FOS dT/dt, also grouped by module. It should be noted that during the event, a high dT/dt was observed for both the thermocouple and FOS on Module 6. A trigger level of 0.1°C/s was used. With this trigger level, there is a clear distinction between the other nine modules undergoing a normal discharge, and the module undergoing a short-circuit. In Figure 4.11 (a, b), there are clear dT/dt flags set when module 6 is short circuited and this allows for easy detection of the unexpected event by the host controller allowing it to isolate the battery from the source and load. Though it may not prevent catastrophic failure if the short circuit is occurring local to the module, at least it is detected and action can be taken to prevent further escalation quickly.
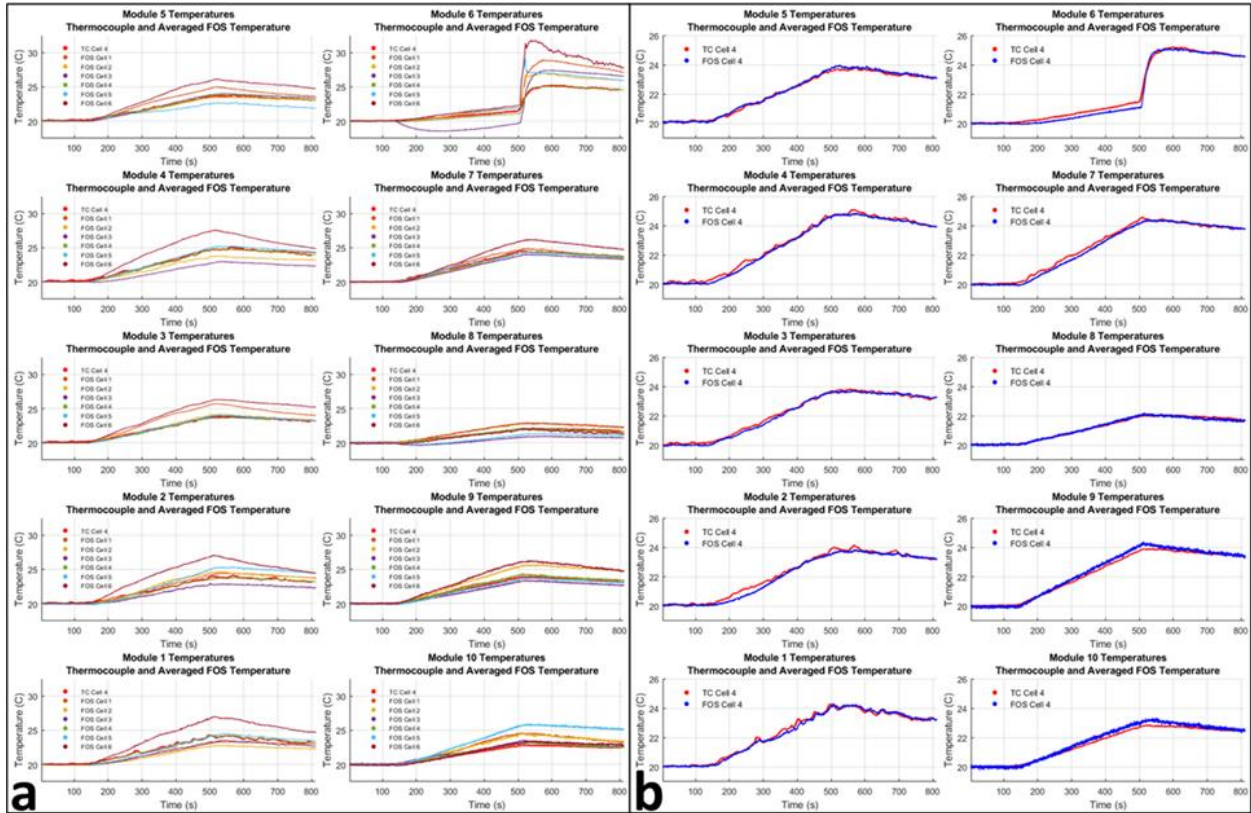
Figure 4.10. Abnormal Operation of a Ten Module System. (a) Temperature data from both thermocouples and the FOS during abnormal operation. (b) Temperature data from thermocouples and FOS data averaged along the corresponding cell.
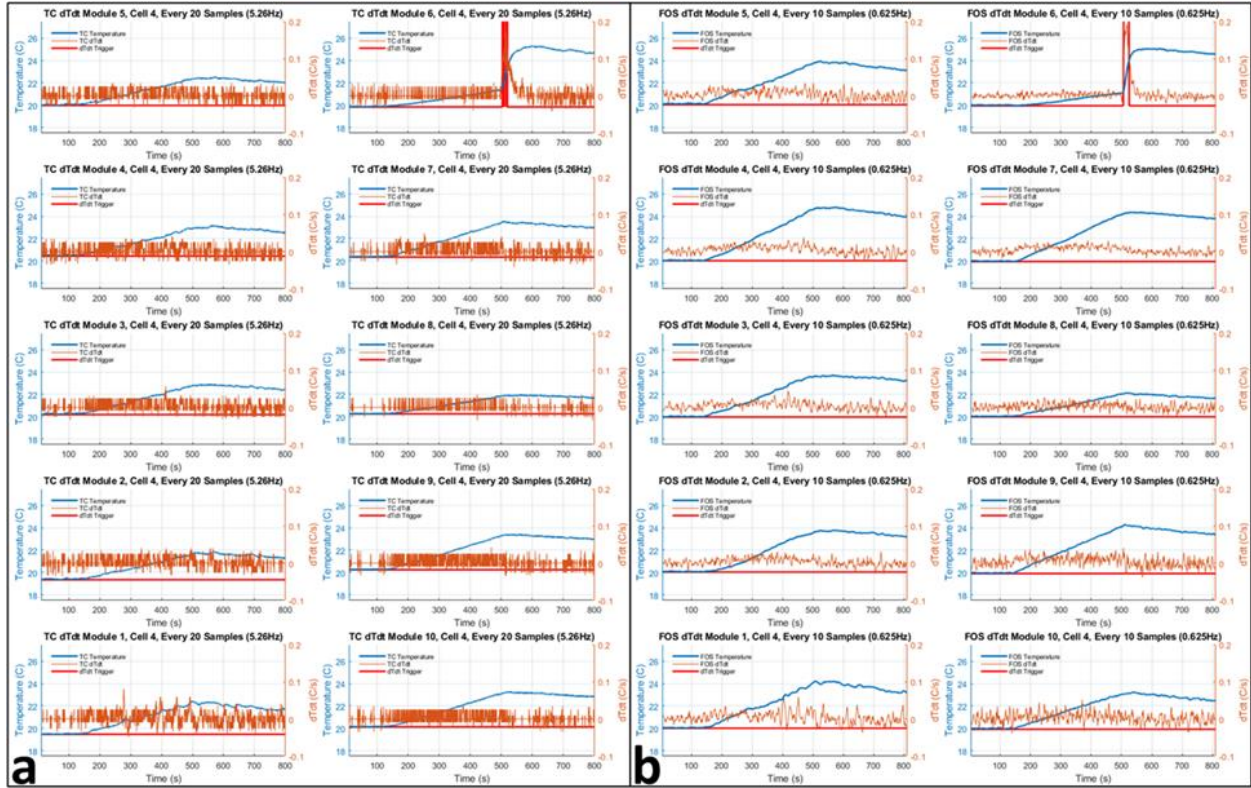
Figure 4.11. Thermocouple and FOS dT/dt During Abnormal Operation. (a) Thermocouple dT/dt from the 10S6P battery during abnormal operation. (b) FOS dT/dt from the 10S6P battery during abnormal operation.

4.5.3 FOS USE DURING FAILURE CONDITIONS

As described earlier in Figure 4.6, a single 18650 cell is outfitted with a patch heater, with the FOS suspended away from the cell at multiple locations. The cell cap is injected with JB Weld to prevent the CID from engaging, wrapped with a silicone heater, and charged at 3.2 A until the cell reaches overcharge conditions and destructively fails. This experiment was set up as shown previously in Figure 4.6 (d). Strain measurements are recorded throughout the test, shown in Figure 4.12 (a). The sharp rise in strain in the data correlates with the time at which failure occurs. At the point of failure, there are three separate increases in strain in the FOS data, which correlate with

93

the cell venting, the first ejection of ignition material, and the point when the cell was engulfed in

flames. These three points of interest are shown in Figure 4.12 (b) along with a photograph of the

thermal runaway in Figure 4.12 (c) taken during the experiment by the camera placed inside the

destructive testing container.
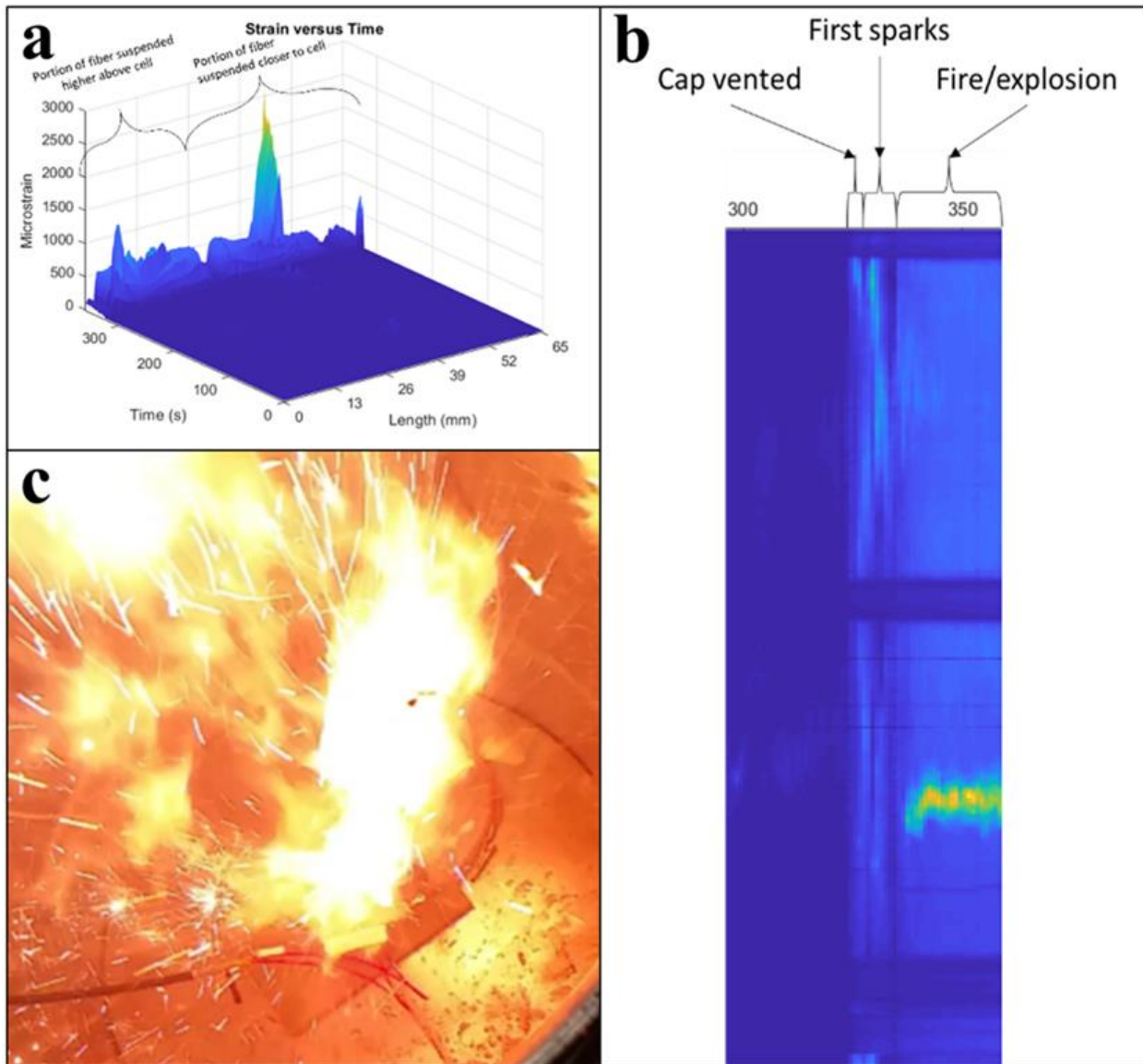
Figure 4.12. FOS Strain During Acoustic Detection. (a) Strain data from an FOS located at

two distances from the cell indicating the point at which failure occurred within the cell and the

accompanying rise in strain that occurs at this moment. (b) This point of failure has three distinct

94

regions attributed to the point when the cap vented, the first ignition sparks are observed, and the

final destruction of the cell. (c) This point of destructive failure was captured by the camera

included inside the test chamber.

Further analysis of the audio recordings and the strain detected by a suspended FOS is

shown in Figure 4.13 (a) and (b), where the portion of the data in yellow indicates a high strain

caused by flames and hot gasses passing the FOS after the cell vented. This experiment was set up

as shown previously in Figure 4.6 (c). The FOS is divided into three portions placed at different

heights and, due to the height offset, the FOS shows a change in strain occurring at different times,

which is shown in Figure 4.13 (d). The offset shows that the strain measured by the FOS is due to

the time delay associated with high temperature venting fumes or flames transiting each of these

separate portions of the FOS, which can then be correlated to an audible 'pop' detected by a

microphone inside the container. This audio recording along with the measured strain at each of

the FOS locations is shown in Figure 4.13 (b, d), with results showing a noticeable change in strain

at the same time the audio signature is detected. This can be compared to the thermocouple

temperature measurement of the cell, shown in Figure 4.13 (c) showing that the change in FOS

strain is not caused by temperature changes.
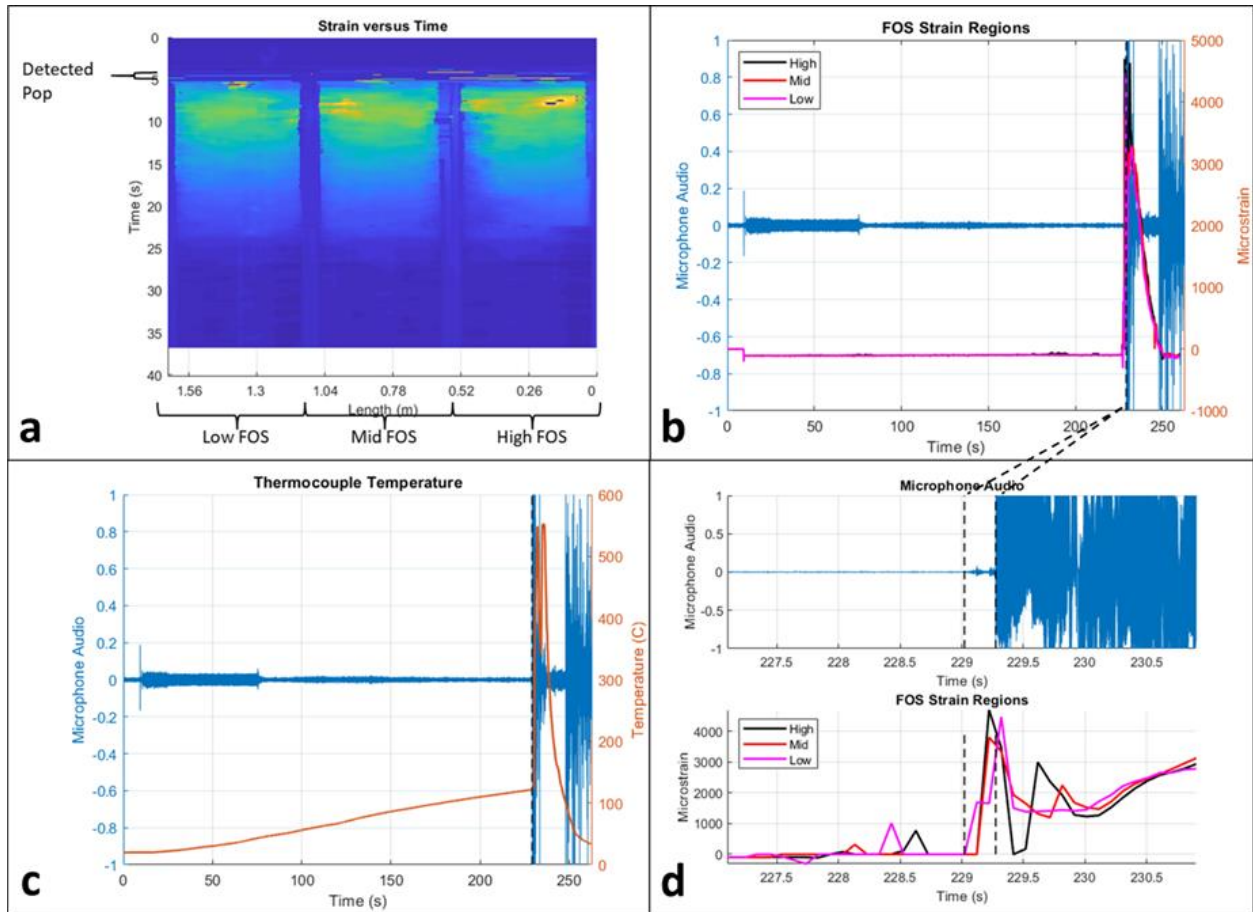
Figure 4.13. FOS Strain During Second Acoustic Detection. (a) The point of failure observed
by the strain measurement in the FOS can be correlated to an audible acoustical signature
recorded by a microphone also placed inside the destructive testing chamber. The FOS is divided
into three regions located at various heights within the containment vessel. (b) Comparison of
FOS strain for all three regions with the audio recorded by the microphone. (c) Thermocouple
temperature comparison to recorded audio. (d) Enlarged view of area of interest. It should be
noted that due to the large disparity in sampling rates between audio (44 kHz) and FOS (10 Hz),
this expanded view has a low number of data points. There is a visible change in FOS data
during venting, and this correlates to the recorded audio.

96

The same overcharge procedure is applied to a 6S/1P module of 18650 cells. All six cells vented during this procedure. The module remains are shown in Figure 4.14 (a). Figure 4.14 (b) shows an image where the FOS is in frame, boxed in red. It should be noted that this image is from a different experiment, but was appended here to show the location of the FOS. Figure 4.14 (c) shows the value of summed FOS data per sample, which has an upward trend. This is likely due to the increase in ambient temperature, as more energy and heat is added to make the module destructively fail. Figure 4.14 (d) shows the change in strain over change in time, with the intent of filtering out the gradual change in ambient temperature, and correlating audio events with large changes in FOS strain. This experiment shows the FOS data collected during this test correlated to most of the major acoustical events.
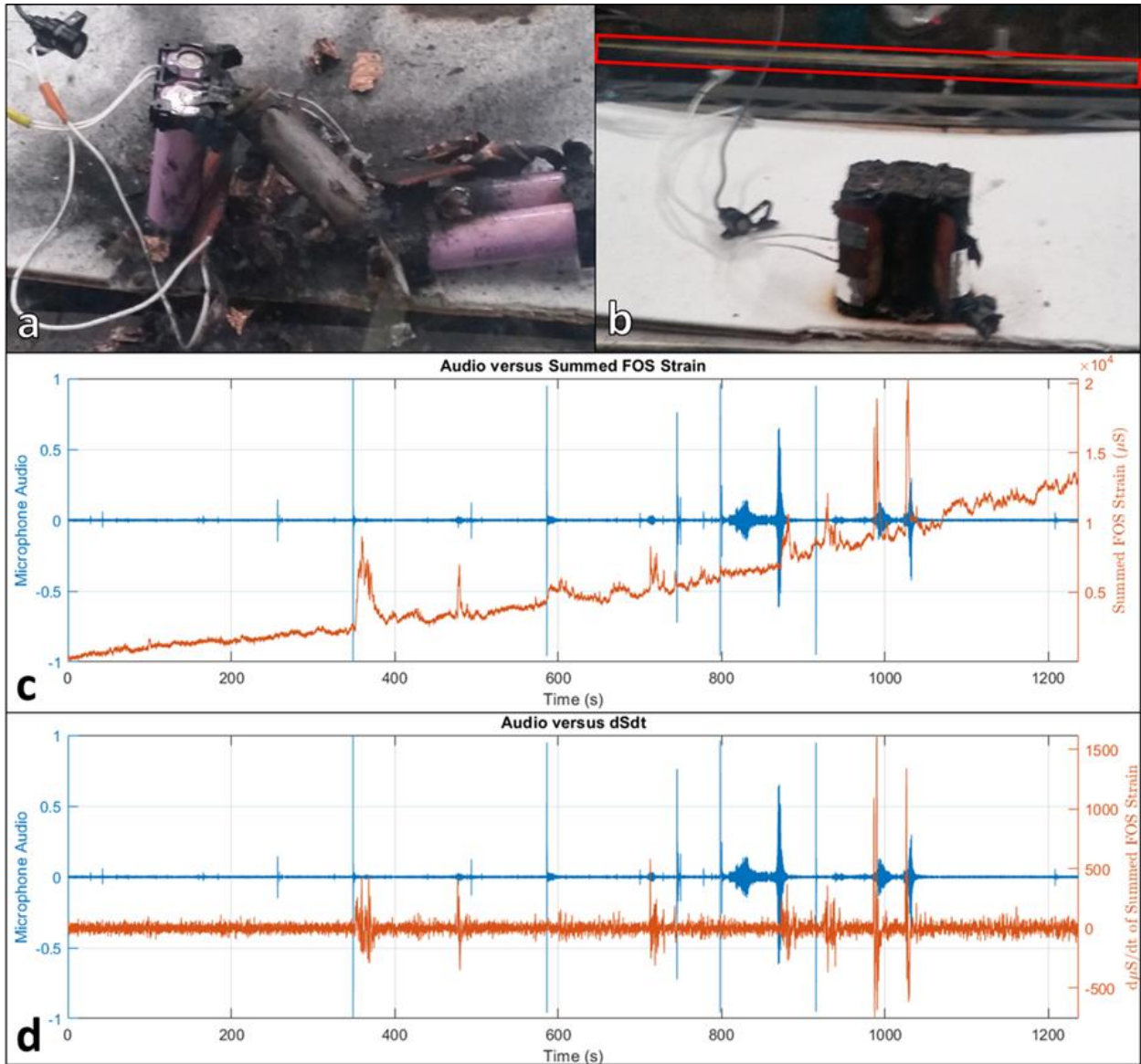
Figure 4.14. Comparison of Acoustic and FOS Data. (a) Remains of module after failure. (b) Image showing placement of FOS, boxed in red. (c) Comparison of FOS data summed across the length of the fiber per sample versus recorded audio. (d) dS/dt of FOS data which was summed across the length of the fiber per sample. Most of the prominent audio events can be correlated to large dS/dt events.

4.6 CONCLUSION

Thermocouples and thermistors are the traditional method of sensing thermal changes within materials. These devices are subject to external influences that lead to failure and are bulky in applications requiring the use of multiple temperature readings, such as battery modules. Here, an FOS is used to monitor temperature fluctuations within multiple battery modules consisting of multiple cells during normal charging/discharging cycles and abnormal operating conditions. It is shown that multiple fibers attached end-on-end using optical couplers to form essentially one long fiber can then be connected with a monitoring system with minimal coupler noise and data loss introduced into the thermal data. This end-on-end connection of fiber provides easier installation in larger battery fabrications and replacement of fiber sections if they become damaged as compared to a single FOS. Additionally, it is shown that fiber can detect sudden rise in temperature seen when a cell/module deviates from standard operating conditions.

It was also shown that a FOS may be suspended away from a cell or module and used to detect strain caused by vibrations due to ventilation fumes or other gasses that occur when a cell has sustained a catastrophic or destructive failure. The data collected by the FOS is compared with an audible acoustic signature collected by a microphone and video images captured by a camera. Taken together, a FOS is capable of sensing thermal changes, strain, and changes in the ambient environment when implemented through different means of attachment or suspension within the enclosure containing the batteries.

4.7 ACKNOWLEDGMENTS

conclusions or recommendations expressed in this material are those of the author(s) and do not necessarily reflect the views of the Naval Air Warfare Center Aircraft Division (NAVSEA).

4.8 REFERENCES

[1] Y. Nishi, Lithium ion secondary batteries; past 10 years and the future, *J. Power Sources*, 100 (2001).

[2] P.J. Bugryniec, J.N. Davidson, D.J. Cumming, S.F. Brown. Pursuing safer batteries: thermal abuse of LiFePO$_4$ cells, *J. Power Sources*, 414 (2019).

[3] M. Arhant, N. Meek, D. Penumadu, P. Davies, N. Garg, "Residual Strains using Integrated Continuous Fiber Optic Sensing in Thermoplastic Composites and Structural Health Monitoring." *Experimental Mechanics*, (2017).

[4] S.T. Kreger, N.A.A. Rahim, N. Garg, S. Klute, D. Metrey, N. Beaty, J.W. Jeans, R. Gamber, "Optical frequency domain reflectometry: principles and applications in fiber optic sensing." *Proceedings of SPIE*, (2016).

[5] S.T. Kreger, D.K. Gifford, M.E. Froggatt, A.K. Sang, R.G. Duncan, M.S. Wolfe, B.J. Soller, "High-resolution extended distance distributed fiber-optic sensing using Rayleigh backscatter." *Proceedings of SPIE*, (2007).

[6] M. Sheikh, A. Elmarakbi, S. Rehman, "A combined experimental and simulation approach for short circuit prediction of 18650 lithium-ion battery under mechanical abuse conditions." *Journal of Energy Storage*, 32 (2020).

[7] H. Popp, M. Koller, M. Jahn, A. Bergmann, "Mechanical methods for state determination of Lithium-Ion secondary batteries: A review." *Journal of Energy Storage*, 32 (2020).

[8] M. Nascimento, S. Novais, M.S. Ding, M.S. Ferreira, S. Koch, S. Passerini, J.L. Pinto. "Internal strain and temperature discrimination with optical fiber hybrid sensors in Li-ion batteries." *J. Power Sources*, 410-411 (2019) 1-9.

[9] E. Vergori, Y. Yu, "Monitoring of Li-ion cells with distributed fibre optic sensors." *Procedia Structural Integrity*, 24 (2019).

[10] B. Gu, M. Yin, A.P. Zhang, J. Qian, S. He, "Optical fiber relative humidity sensor based on FBG incorporated thin-core fiber modal interferometer." *Optics Express*, 19 (2011).

[11] K. Feng, J. Cui, Y. Jin, X. Sun, D. Jiang, H. Dang, Y. Niu, J. Tan, "Enhancement of the Performance and Data Processing Rate of an Optical Frequency Domain Reflectometer Distributed Sensing System Using a Limited Swept Wavelength Range." *Sensors*, 18 (2018).

[12] S.Young, D. Penumadu, D. Foster, H. Maeser, B. Balijepalli, J. Reese, D. Bank, J. Dahl, P. Blanchard, "Smart Adhesive Joint with High-Definition Fiber-Optic Sensing for Automotive Applications." *Sensors*, 20 (2020).

[13] T. Matsuo, M. Uchida, H. Cho, "Development of Acoustic Emission Clustering Method to Detect Degradation of Lithium Ion Batteries." *Journal of Solid Mechanics and Materials Engineering*, 5 (2011).

[14] C-Y. Choe, W-S. Jung, J-W. Byeon, "Damage Evaluation in Lithium Cobalt Oxide/Carbon Electrodes of Secondary Battery by Acoustic Emission Monitoring." *Materials Transactions*, 56 (2015).

[15] H.L. Atchison, Z.R. Bailey, D.A. Wetz, M. Davis, J.M. Heinzel, "Fiber Optic Based Thermal and Strain Sensing of Lithium-Ion Batteries at the Individual Cell Level," *Journal of The Electrochemical Society*, 168 (2021) 4.

[16] H.L. Atchison, Z.R. Bailey, D.A. Wetz, M. Davis, J.M. Heinzel, "Fiber Optic Based Thermal Sensing of Lithium-Ion Cells at the Module Level," Manuscript submitted for publication, Journal of The Electrochemical Society, review pending (2022).

[17] V. Raman, M. Drissi-Habti, P. Limje, A. Khadour. "Finber SHM-Coverage of Inter-Plies and Bondings in Smart Composite by Dual Sinusoidal Placed Distributed Optical Fiber Sensors." *Sensors*, 742 (2019).

CHAPTER 5: ENERGY STORAGE SIZING TOOL

5.1 MOTIVATION

There are several civilian and defense applications actively investigating intelligent power system architectures that incorporate multiple power generation sources, energy storage units, and power electronic voltage regulation mechanisms. These architectures are designed to cater to both conventional and advanced electrical loads. Particularly, advanced loads pose a challenge due to their transient profiles and high-rate energy demands, complicating the optimal sizing of energy storage solutions. The reliance on manufacturer datasheets, which often contain misleading information and a restricted set of empirically derived voltage versus capacity curves [1], further complicating the data extraction process. While energy storage sizing tools exist [2, 3], none are documented that use empirically collected data within the MATLAB software environment. To address these issues, a comprehensive energy storage sizing tool has been developed within MATLAB that grants users a high degree of flexibility, allowing them to optimize and validate multiple solutions. The subsequent sections will delve into the details of this tool and the design process employed to bring it to fruition.

5.2 BACKGROUND

The growing energy demands across civilian and defense domains have underscored the need for intelligent power system architectures capable of accommodating energy storage as an autonomous source or a buffer for transient loads. To fulfill these evolving load requirements, the sizing of energy storage remains a challenge. This task is further complicated by the variability in impedance and usable capacity, which is contingent upon rate and operating temperature. To address these complexities, a novel MATLAB-based energy storage sizing tool has been designed,

developed, and validated. The tool harnesses empirically amassed data from wide range of energy storage solutions, with compiled data covering a wide range of usable C-rates, operating temperatures and chemistries to establish an all-encompassing database. Through an analysis of the user's voltage and load inputs, the tool optimally sizes energy storage solutions for each cell in the database. This documentation describes the methodology behind the tool's design and presents validation results for various modules.

5.2.1 ENERGY STORAGE

Energy storage technologies play a pivotal role in addressing the ever-growing demands for power across various domains, both civilian and defense. These technologies serve as essential components within power system architectures [4], fulfilling dual roles as autonomous energy sources and transient load buffers. The task of sizing energy storage to meet evolving load requirements is a core challenge in such systems.

Lead acid batteries are the stalwart of energy storage, boasting a proven historical track record of reliability and stability [5]. Their availability as commercial-off-the-shelf (COTS) products enhances their appeal for various applications. Despite their longevity, they do exhibit limitations in terms of power and energy density, lagging alternative energy storage methods. Nonetheless, their enduring presence in the market make it a testament to their continued relevance in scenarios that prioritize safety and dependability.

Lithium-ion batteries represent a significant leap forward in energy storage technology, offering substantially improved power and energy densities when compared to lead acid counterparts [6]. This elevated performance, however, comes hand in hand with safety concerns, particularly when subjected to harsh conditions or mechanical stresses [7, 8]. Additionally, their

cycle life can be compromised by high-rate operations [9]. Despite these challenges, their prevalence in portable electronics, electric vehicles, and renewable energy systems underscores their practicality and utility in addressing modern energy storage needs.

Supercapacitors, or ulracapacitors, which are known for their remarkable power density and extended lifespan, present a unique energy storage solution [10, 11]. They excel at buffering short term transient events when compared to batteries, making them more suitable for applications demanding rapid bursts of power. Additionally, they have an improved ability to handle frequent charge and discharge cycles without significantly degrading their performance. Supercapacitors find relevance in scenarios where their rapid response and durability are of importance.

Nickel Zinc batteries are emerging as a potential alternative that balances safety considerations with energy storage performance [12]. These batteries offer a compromise between power and energy density, with the added advantage of enhanced safety features. However, their cycle life, despite improvements, remains relatively low compared to other established technologies. Their evolution and further research could potentially position them as a safer and more efficient energy storage solution.

Sizing energy storage solutions is heavily tied to the discharge profile of the technology. Different technologies exhibit varying discharge voltage characteristics and sustained power capabilities across their usable capacity. Lithium-ion batteries are much better at maintaining a near-constant voltage within a wider percentage of its State-of-Charge, which simplifies their integration into systems with specific voltage requirements. In contrast, supercapacitors exhibit a linear decrease in voltage as their stored energy is depleted, while being able to supply higher bursts of power. While Nickel Zinc share many characteristics with existing lead acid and lithium-ion technologies, their capacity and cycle life are heavily temperature dependent, despite the

additional safety the chemistry provides. These distinctions necessitate sizing methodologies that ensure optimal sizing of energy storage systems that take not only power and energy density into account, but also the reliability and availability of these solutions.

5.2.2 COMPILATION AND COLLECTION OF CYCLING DATA

Typically, cell data that can be obtained from manufacturers and data that is provided from datasheets is cycled in a constant-current format. This data represents various complete discharges of a cell at varying constant-currents with a comparison of the available capacity for these discharges. The creation of the sizing tool assumed that this data would be more readily available than constant-power cycling data, where a cell provides a constant power throughout a discharge while voltage and current vary. At UTA, constant-current cycling data had been collected for previous efforts that studied various lithium battery chemistries at varying constant-current discharge rates (C-rates) and at varying operating temperatures (0°C-40°C). This data was compiled into an initial database of cycling data for use with the Sizing Tool. Due to the long timespan of some of the lower C-rate discharges, this original dataset was over 2 GB. Since typical battery discharge curves are simple, we can interpolate most of this data into a more compact format for use in a database. For this process, we took any cycling data longer than 500 samples and down sampled the dataset to 500. For some of the higher C-rates, there are not enough samples before the discharge finishes due to the short timeframe of some of these higher rates. Any cycling data that is less than 500 samples was kept as-is to avoid interpolation.

The format of the cell database consists of three sections: cell name, cell datasheet parameters and cycling data. The cell datasheet parameters consist of voltage ranges, charge, and discharge current limits, and cell mass/dimensions. The empirically collected cycling data is

presented in a nested table format, with the outer table containing cycling data corresponding to different temperatures and C-rates. Each inner table contains an array that is at most, 500 rows with up to 7 columns. Each column in this inner table corresponds to a relevant column from the raw cycling data. The only necessary values are voltage, current, capacity and step time. Figure 5.1 below shows the latest version of the database and an example of how cycling data is stored.
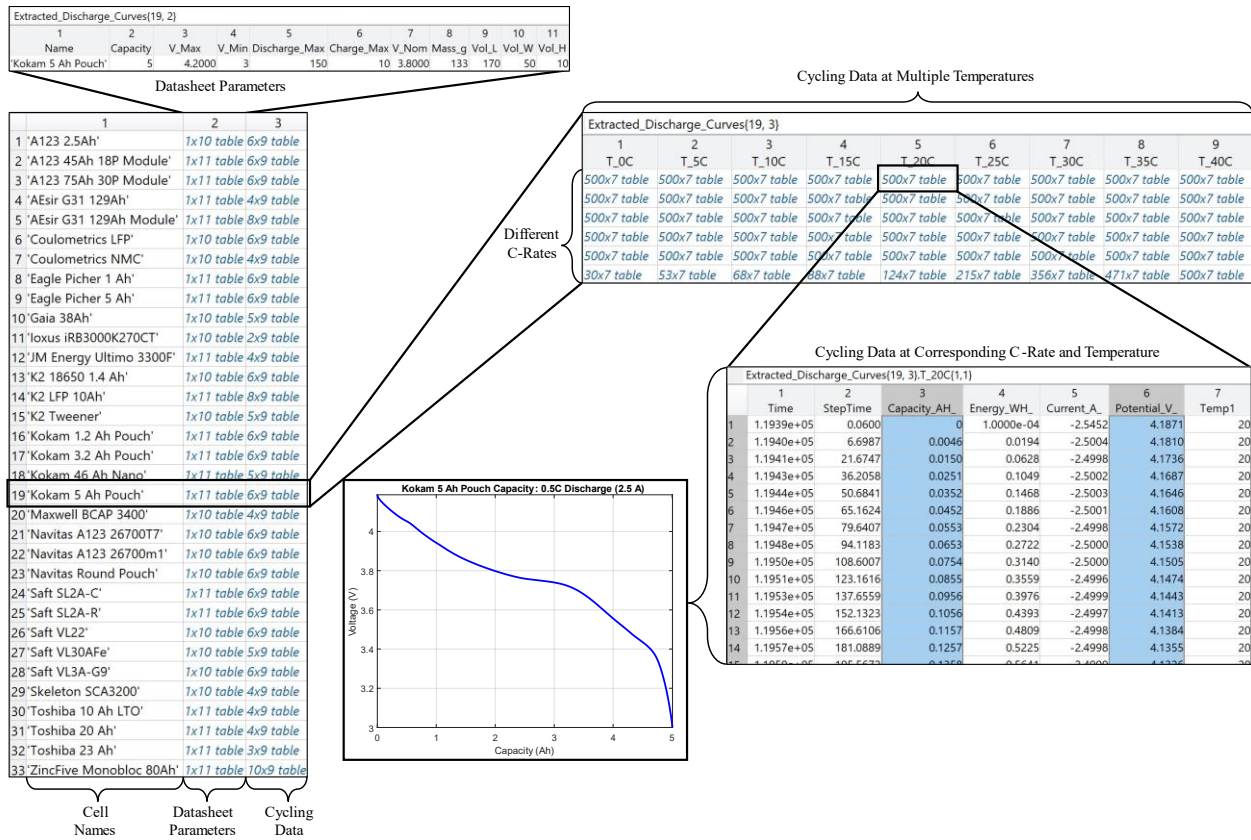
Extracted_Discharge_Curves{19, 2}

	1	2	3	4	5	6	7	8	9	10	11
	Name	Capacity	V_Max	V_Min	Discharge_Max	Charge_Max	V_Nom	Mass_g	Vol_L	Vol_W	Vol_H
	'Kokam 5 Ah Pouch'	5	4.2000	3	150	10	3.8000	133	170	50	10

Datasheet Parameters

Cycling Data at Multiple Temperatures

	1	2	3
1	'A123 2.5Ah'	1x10 table	6x9 table
2	'A123 45Ah 18P Module'	1x11 table	6x9 table
3	'A123 75Ah 30P Module'	1x11 table	6x9 table
4	'AEsir G31 129Ah'	1x11 table	4x9 table
5	'AEsir G31 129Ah Module'	1x11 table	8x9 table
6	'Coulometrics LFP'	1x10 table	6x9 table
7	'Coulometrics NMC'	1x10 table	4x9 table
8	'Eagle Picher 1 Ah'	1x11 table	6x9 table
9	'Eagle Picher 5 Ah'	1x11 table	6x9 table
10	'Gaia 38Ah'	1x10 table	5x9 table
11	'Ioxus iRB3000K270CT'	1x10 table	2x9 table
12	'JM Energy Ultimo 3300F'	1x11 table	4x9 table
13	'K2 18650 1.4 Ah'	1x10 table	6x9 table
14	'K2 LFP 10Ah'	1x11 table	8x9 table
15	'K2 Tweener'	1x10 table	5x9 table
16	'Kokam 1.2 Ah Pouch'	1x11 table	6x9 table
17	'Kokam 3.2 Ah Pouch'	1x11 table	6x9 table
18	'Kokam 46 Ah Nano'	1x11 table	5x9 table
19	'Kokam 5 Ah Pouch'	1x11 table	6x9 table
20	'Maxwell BCAP 3400'	1x10 table	4x9 table
21	'Navitas A123 26700T7'	1x10 table	6x9 table
22	'Navitas A123 26700m1'	1x10 table	6x9 table
23	'Navitas Round Pouch'	1x10 table	6x9 table
24	'Saft SL2A-C'	1x11 table	6x9 table
25	'Saft SL2A-R'	1x11 table	6x9 table
26	'Saft VL22'	1x10 table	6x9 table
27	'Saft VL30AFe'	1x10 table	5x9 table
28	'Saft VL3A-G9'	1x10 table	6x9 table
29	'Skeleton SCA3200'	1x10 table	4x9 table
30	'Toshiba 10 Ah LTO'	1x11 table	4x9 table
31	'Toshiba 20 Ah'	1x11 table	4x9 table
32	'Toshiba 23 Ah'	1x11 table	3x9 table
33	'ZincFive Monobloc 80Ah'	1x11 table	10x9 table

Cell Names — Datasheet Parameters — Cycling Data

Different C-Rates

Extracted_Discharge_Curves{19, 3}

1	2	3	4	5	6	7	8	9
T_0C	T_5C	T_10C	T_15C	T_20C	T_25C	T_30C	T_35C	T_40C
500x7 table	500x7 table	500x7 table	500x7 table	500x7 table	500x7 table	500x7 table	500x7 table	500x7 table
500x7 table	500x7 table	500x7 table	500x7 table	500x7 table	500x7 table	500x7 table	500x7 table	500x7 table
500x7 table	500x7 table	500x7 table	500x7 table	500x7 table	500x7 table	500x7 table	500x7 table	500x7 table
500x7 table	500x7 table	500x7 table	500x7 table	500x7 table	500x7 table	500x7 table	500x7 table	500x7 table
30x7 table	53x7 table	68x7 table	68x7 table	124x7 table	215x7 table	356x7 table	471x7 table	500x7 table

Cycling Data at Corresponding C-Rate and Temperature

Extracted_Discharge_Curves{19, 3}.T_20C{1,1}

	1	2	3	4	5	6	7
	Time	StepTime	Capacity_AH_	Energy_WH_	Current_A	Potential_V_	Temp1
1	1.1939e+05	0.0600	0	1.0000e-04	-2.5452	4.1871	20
2	1.1940e+05	6.6987	0.0046	0.0194	-2.5004	4.1810	20
3	1.1941e+05	21.6747	0.0150	0.0628	-2.4998	4.1736	20
4	1.1943e+05	36.2058	0.0251	0.1049	-2.5002	4.1687	20
5	1.1944e+05	50.6841	0.0352	0.1468	-2.5003	4.1646	20
6	1.1946e+05	65.1624	0.0452	0.1886	-2.5001	4.1608	20
7	1.1947e+05	79.6407	0.0553	0.2304	-2.4998	4.1572	20
8	1.1948e+05	94.1183	0.0653	0.2722	-2.5000	4.1538	20
9	1.1950e+05	108.6007	0.0754	0.3140	-2.5000	4.1505	20
10	1.1951e+05	123.1616	0.0855	0.3559	-2.4996	4.1474	20
11	1.1953e+05	137.6559	0.0956	0.3976	-2.4999	4.1443	20
12	1.1954e+05	152.1323	0.1056	0.4393	-2.4997	4.1413	20
13	1.1956e+05	166.6106	0.1157	0.4809	-2.4998	4.1384	20
14	1.1957e+05	181.0889	0.1257	0.5225	-2.4998	4.1355	20

Kokam 5 Ah Pouch Capacity : 0.5C Discharge (2.5 A)

Figure 5.1. Cell Database Example and Format. This figure shows an example of how cycling data is accessed. The example above shows a plot of a 0.5C constant-current discharge for a Kokam 5 Ah pouch cell.

The latest version of the Cell Database contains 33 cells encompassing seven different chemistries: Lithium-Ion, Lithium-Iron-Phosphate (LiPO), Nickel-Manganese-Cobalt (NMC),

Nickel-Cobalt-Aluminum (NCA), Lithium-Titanate-Oxide (LTO), Ultracapacitors, and Nickel-Zinc (NiZn). Additionally, some "cells" in the database are represented as modules. This is supported due to an additional feature where as long as the voltage range, mass and volume are properly defined, the tool will attempt to size the module as a "cell". This allows the Sizing Tool to effectively size a battery using pre-existing modules.

The database created with the Data Import Tool is a unique format developed for this application. Figure 5.1 above shows an example of how to manually access data for a specific cell. If data needs to be manually added to the database without the aid of the Data Import Tool, this formatting must be followed for the new data to work with the Sizing Tool.

5.3 MATLAB DATA IMPORT TOOL

The tool developed here is intended to be easily expanded by the user as additional empirical data is collected. The data can be collected by traditional methods using commercial or custom-made electrochemical cyclers assuming the output is some sort of spreadsheet containing time, voltage, current, capacity, and temperature data. The initial database used here has been assembled from nineteen different cells cycled using Maccor, Chroma, and Arbin cyclers respectively. Each cell in the database was discharged and recharged across a wide variety of C-Rates, typically between three and five depending on the cell, at various temperatures, ranging from 0°C to 40°C in 5°C increments. The rates studied varies for each cell since there are unique limits recommended by the manufacturer, but examples are 0.5C, 1C, 5C, 10C, 15C and maximum C-rate for each cell. In each cycle, the cell was charged and discharged symmetrically up until the maximum recommended charge rate is reached. If cycling continues at rates beyond the maximum charge rate, the discharge C rate is increased while the maximum recharge rate is maintained. Each

cell is cycled within a temperature chamber whose accuracy is ±1.5°C. The cells are rested for at least one hour after each cycle is completed to allow ambient temperature to be restored. In most cases, the data is in a single data file with columns containing the data types mentioned above as well as the type of procedure being executed, charge, discharge, rest, etc.

Typically, the data sample rate is quite high, on the order of 10 to 100 Hz, resulting in very large data files. The total raw file size for the original nineteen cells used in the database development was 10.2GB. To improve the database load time, a custom data extraction technique was developed, reducing the dataset to just over 37 MB. The import tool extracts each section and sorts each respective charge, discharge, or rest cycle, accordingly. These sections, if larger than a set length, are downsampled and reformed into a new array. With the use of this method, there is no noticeable difference in data quality. After the data is compressed, it is indexed into the Cell Database, previously discussed in Figure 5.1.

5.3.1 FILE TYPE CONSTRAINTS AND CONSIDERATIONS

This tool takes raw cycling data from a cell and processes the data to create a database entry for the cell. The following file types are compatible with the import tool:

- Excel files (.xlsx)
- Text files (.txt, .tsv, .csv)
- LabVIEW Measurement files (.lvm)

It is critical that the user has the proper formatting for the cell data, as this tool is made to create database entries with expectations on the contents of raw data files. For optimal results, the user should have one or multiple files of cycling data, with the following profiles:

- Multiple constant current discharge and charge rates, with suggested discharge/charge rates of 0.5C, 1C, 5C, 10C, 15C and max C.

- Repeats of the above at various temperatures. Suggested temperature values are between 0°C and 40°C

- If there are multiple repeats of the same C-rate within the file, only the first (unique) will be used for sizing

- Do not use lifecycle testing results or pulsed charge/discharge profiles, as these typically have the same discharge rates and will not generate any useful sizing data

5.3.2 TOOL CAPABILITIES

Screen the user is presented with upon running the tool:
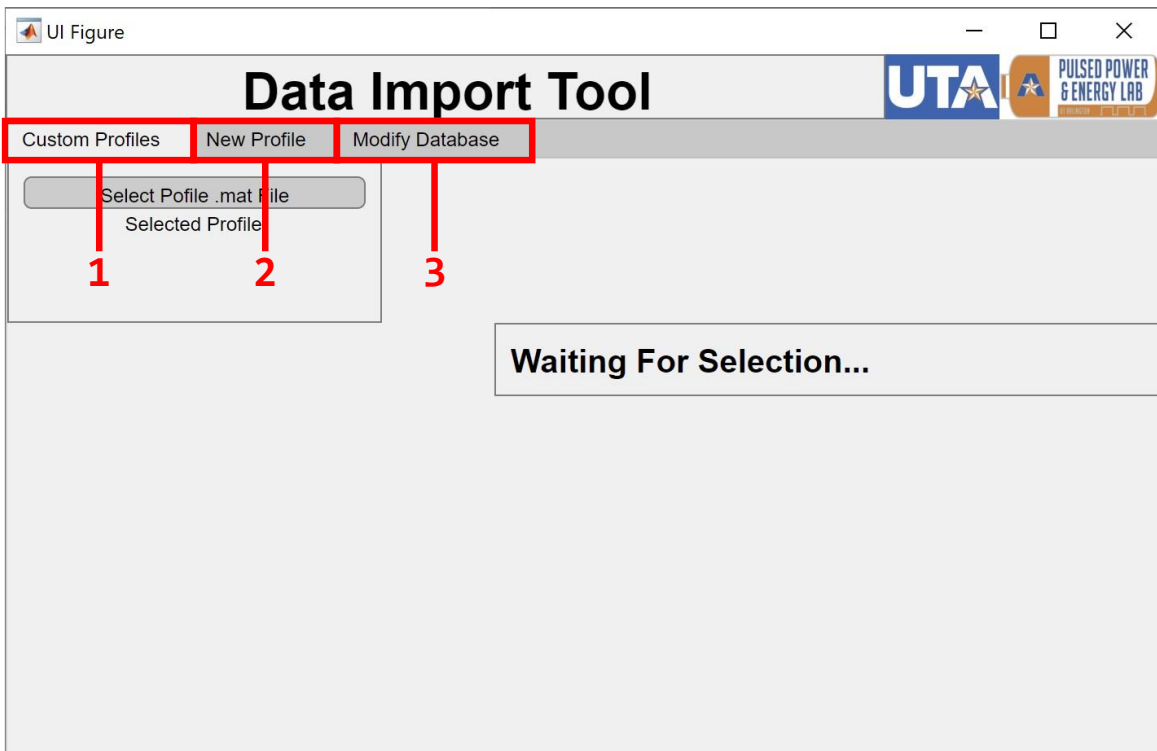
Figure 5.2. Data Import Tool. The numbered sections above represent clickable tabs.

In Figure 5.2 above, each numbered red box represents a clickable tab. Each tab presents the user with a range of capabilities for importing and manipulating data:

1. **Custom Profiles Tab.** This section allows the user to select a previously created custom profile for use in data import. This cannot be used without a previously created custom profile. See [4].

2. **New Profile Tab.** This tab allows the user to create a custom import and allows the user to load a cycling data file to preview for aid in profile creation. Once a profile is created, any raw files with the same column positions and variables will work with that profile.

3. **Modify Database Tab.** This tab allows modification of an existing database, with the following features:

   - Delete One or Multiple Cells

   - Save a Modified Copy of the Database

   - Rename Cells within Database

5.3.3 RUNNING THE TOOL

At least MATLAB R2019a is needed to run the Data Import Tool. Newer versions should be able to run it, though incompatibilities may arise. The user can double click the DataImportTool.mlapp file to open the application.
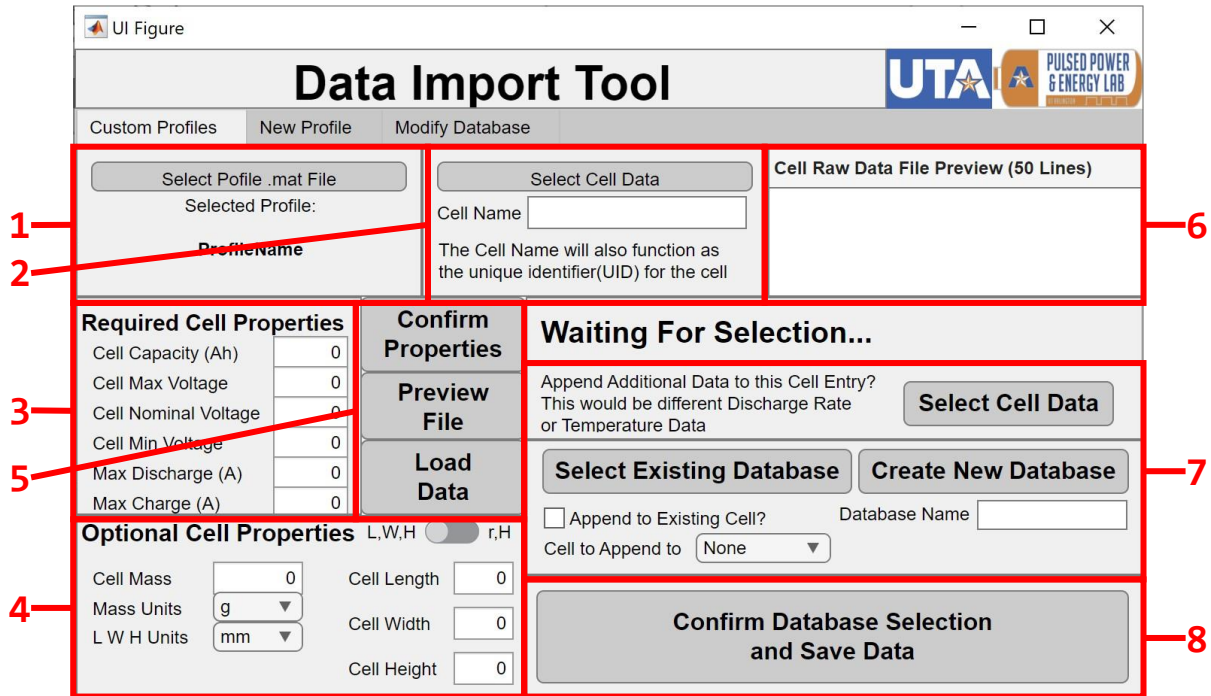
5.3.3.1 CUSTOM PROFILES TAB

Figure 5.3. Data Import Tool: Custom Profiles Tab. For this tab to be used, an existing

custom profile must be loaded from a file or created using the New Profile tab.

Figure 5.3 above shows all possible UI features when the Custom Profiles tab is selected.

These are sequentially revealed to the user as they enter more information.

1. **Select Profile button.** When clicked, this opens a File Explorer window for the user to
   select an existing profile .mat file.

2. **Select Cell Data.** When clicked, this opens a File Explorer window for the user to select
   the raw data file.

3. **Cell Datasheet Parameters.** These are parameters typically found on a datasheet, and all
   values in this section are needed for proper functioning of the tool.

4. **Mass and Volume Information.** While it is not necessary to enter mass and volume values, sizing results can be affected by volume and mass constraints. Leaving these values as zero will cause the sizing results to display as normal, with the exception of zeros for the mass and volume fields.

5. **Confirm Properties button, Preview File button and Load Data button.** These three buttons control how much of the UI is visible to the user and allow the user to preview the selected raw data file. This preview is limited to 50 lines for performance reasons but can be changed within the code if necessary. If there are any invalid parameters when one of the buttons are pushed, the user will be notified and no action will be taken until the parameter is corrected.

6. **Raw Data File Preview.** When the Preview File button is pushed, this will preview the first 50 lines of the raw data file to the user to aid in variable selection and verification of cell parameters.

7. **Appending Data, Database Creation, Append to Database.** Once the raw file is loaded and formatted, the user is given multiple options for where to put the file. If this file only has data for a few C-rates or temperatures, the user can optionally select an additional file to append as a single database entry. No parameters need to be changed, and a File Explorer window is opened once the button is clicked. This will only work if the second file has the same profile as the first. If the profiles are different, the user must either change tabs, create a new profile (see New Profile), or select an existing profile. If the user wants to append to an existing database or append the new data to a cell within an existing database, they must select the corresponding button and follow the File Explorer prompt.

8. **Confirm Selection.** Once the user has selected an option in area 7, this button will become visible. Once clicked, the cell data will be exported to the selected database, and the user can then close the Import Tool or select a new file to import.
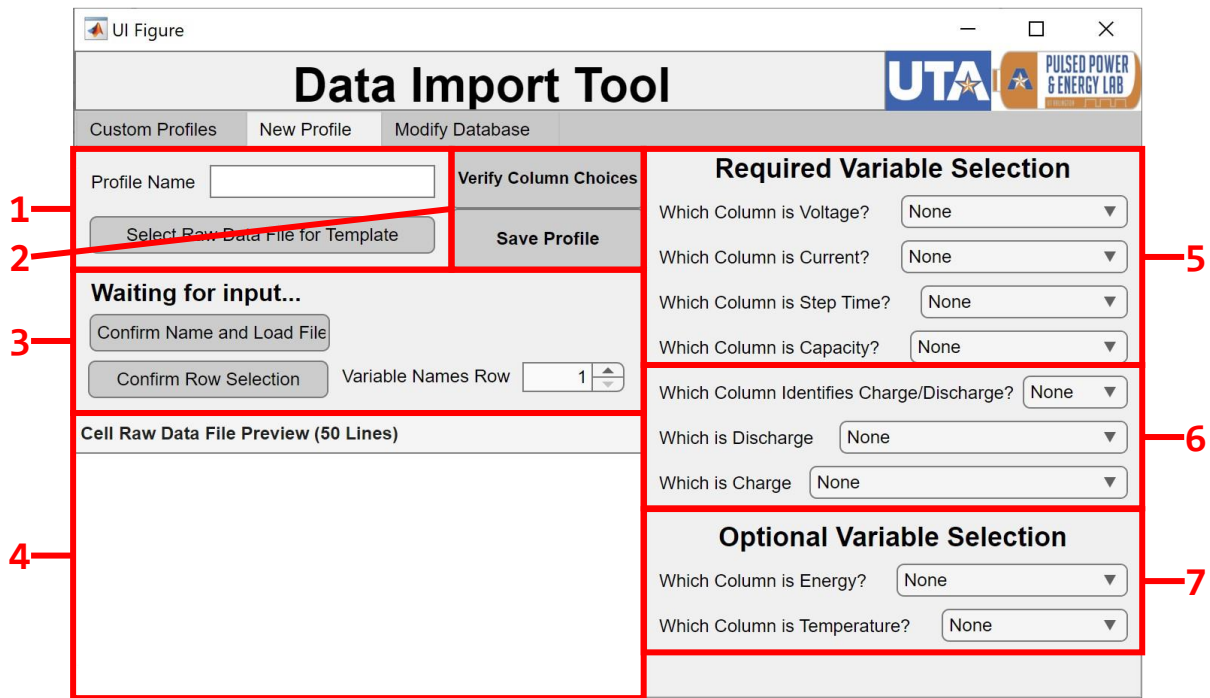
5.3.3.2 NEW PROFILE TAB

Figure 5.4. Data Import Tool: New Profile Tab.

Figure 5.4 above shows all UI features when the New Profile tab is selected. These are sequentially revealed to the user as they enter more information.

1. **Enter Profile Name and Select Template.** When clicked, this opens a File Explorer window for the user to select a raw data file to use as a template for profile creation.

2. **Verify Column Choices and Save Profile.** Once all the parameters in area 5 are entered, these buttons become visible. Once clicked, they verify the logic of each column selection and saves the profile to the selected location.

3. **Load File and Row Selection.** This is used to find the header row of the file, and to get the variable names for each column, such as voltage, current, temperature, etc. Once selected, this will populate the dropdown menus in area 5 with the variable names in the selected row to aid in selection.

4. **Raw Data File Preview.** When the Preview File button is pushed, this will preview the first 50 lines of the raw data file to the user to aid in variable selection and verification of cell parameters.

5. **Required Variable Selection.** These variables are required for the Sizing Tool to function properly, especially the variable used to separate charge and discharge data. This is typically a positive or negative current, but if that is not the case, additional selection in area 6 is required.

6. **Charge and Discharge Isolation.** If the current does not have a +/- sign to indicate charge/discharge, a secondary variable must be used to indicate a charge or discharge. Once the column containing this separator is selected, a new dropdown is populated with unique values from this column and presented to the user to identify which represents a charge or discharge.

7. **Optional Variables.** While these values are not necessary for the Sizing Tool to function, it is highly recommended that the user enter values for these parameters or conduct a charge/discharge profile that includes these results.
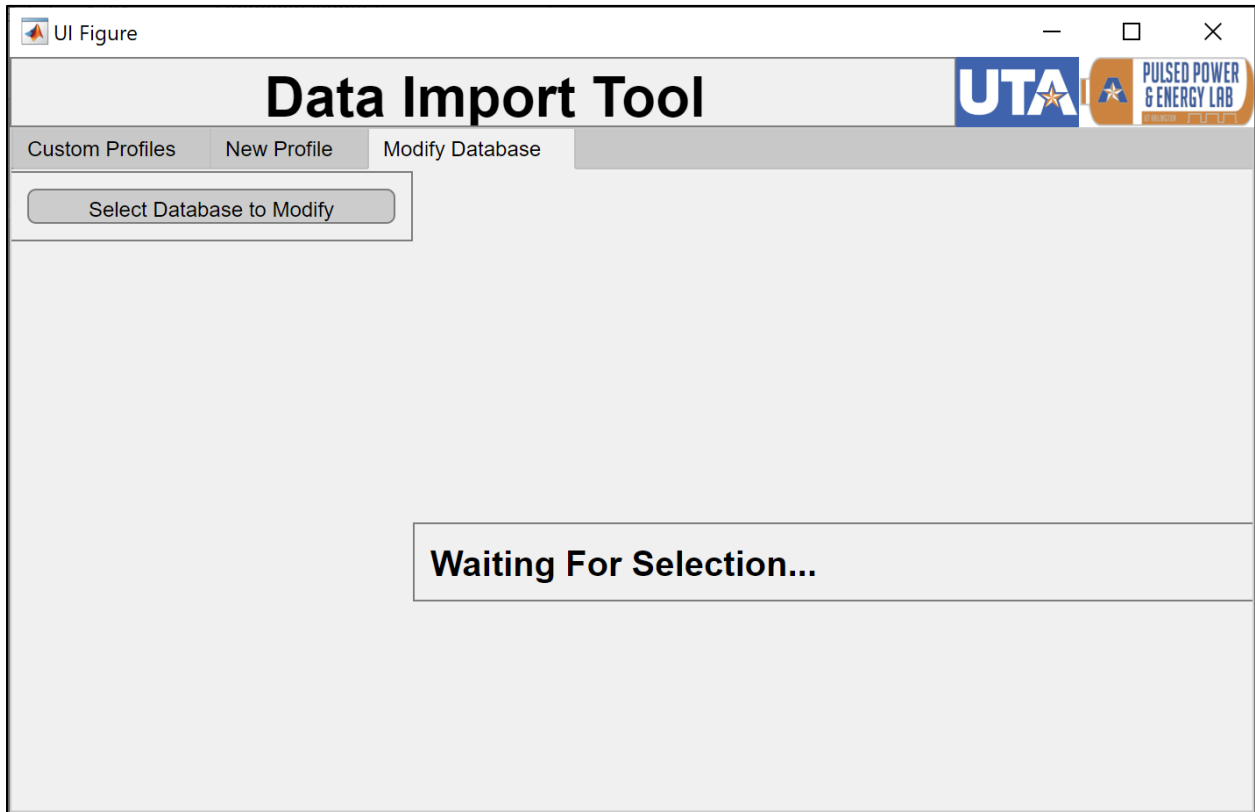
5.3.3.3 MODIFY DATABASE TAB

Figure 5.5. Data Import Tool: Modify Database Tab. Initial screen shown upon selecting the

Modify Database tab.

Figure 5.5 above shows the initial screen under the Modify Database tab. Once the 'Select

Database to Modify' button is pushed, a file explorer window will open and prompt the user for a

path to a database .mat file. Once the database is successfully loaded, the following features
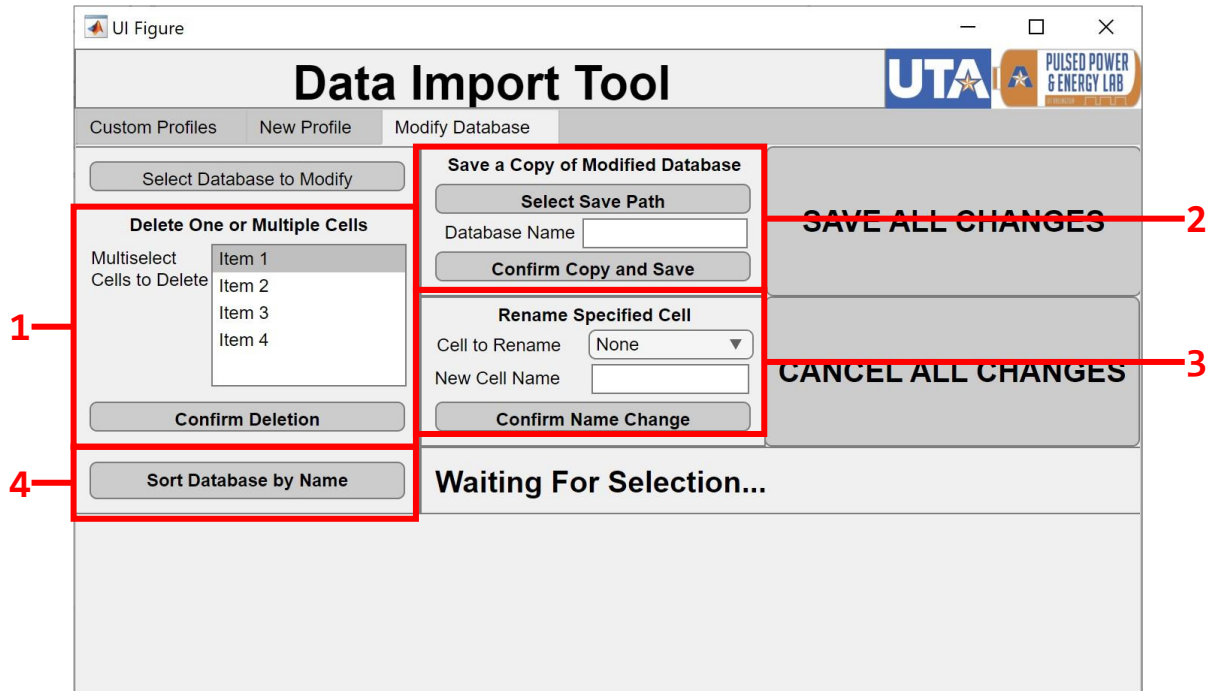
become available to the user, as shown below in Figure 5.6.

Figure 5.6. Data Import Tool: Modify Database Tab with Numbered Sections. After a database is loaded by the tool, additional parameters become available to the user.

1. **Select one or Multiple Cells for Deletion**

   This section allows for deletion of one or multiple cells. To delete more than one cell at a time, hold CTRL and click the cells to remove. Once the requested cells are selected (highlighted in gray), the user should click the confirm deletion button.

2. **Save a Copy of the Modified Database**

   This will open a new File Explorer window to prompt the user for a save location. Once selected, in addition to a new database name, the copy of the modified database is saved to this location.

3. **Rename Cells within the Database**

   This will rename the cell selected from the dropdown menu. It is suggested the user uses the Sort Database by Name button in area 4 after changing a cells name.

117

4. **Re-Sort the Cells within the Database by Name**

   Only necessary if they are out of order or if a cell name is modified. The user can then either save these changes to the loaded database ('Save All Changes' button) or cancel the changes ('Cancel All Changes' button). If a copy of the modified database is created, canceling the changes will not remove this copy. Saving the changes to the original will permanently overwrite data, so it is recommended for used to save changes to a modified copy in area 2.

5.4 ENERGY STORAGE SIZING TOOL

The MATLAB-based Energy Storage Sizing Tool allows the user to input a power requirement, minimum battery voltage, maximum battery voltage, maximum volume, maximum weight, and operational run time. The tool then optimizes the number of Series/Parallel cells required to meet those objectives considering each cell in the database. To minimize size and weight, the tool considers operating each cell at the maximum allowable C-rate such that power demand is met using the minimum number of cells. Accurate estimation of the usable capacity across all usable C-rates is achieved using a curve fitting tool that interpolates all the data within the database. Analysis of all the data considered so far has shown that it is best if there are least four to six different C-rates available for interpolation however, it is not required for the curve fitting tool to work.

5.4.1 SIZING TOOL INPUTS

Before the tool can size, multiple inputs, in addition to the Cell Database, must be provided by the user. Figure 5.7 below shows the initial screen the user is presented with.
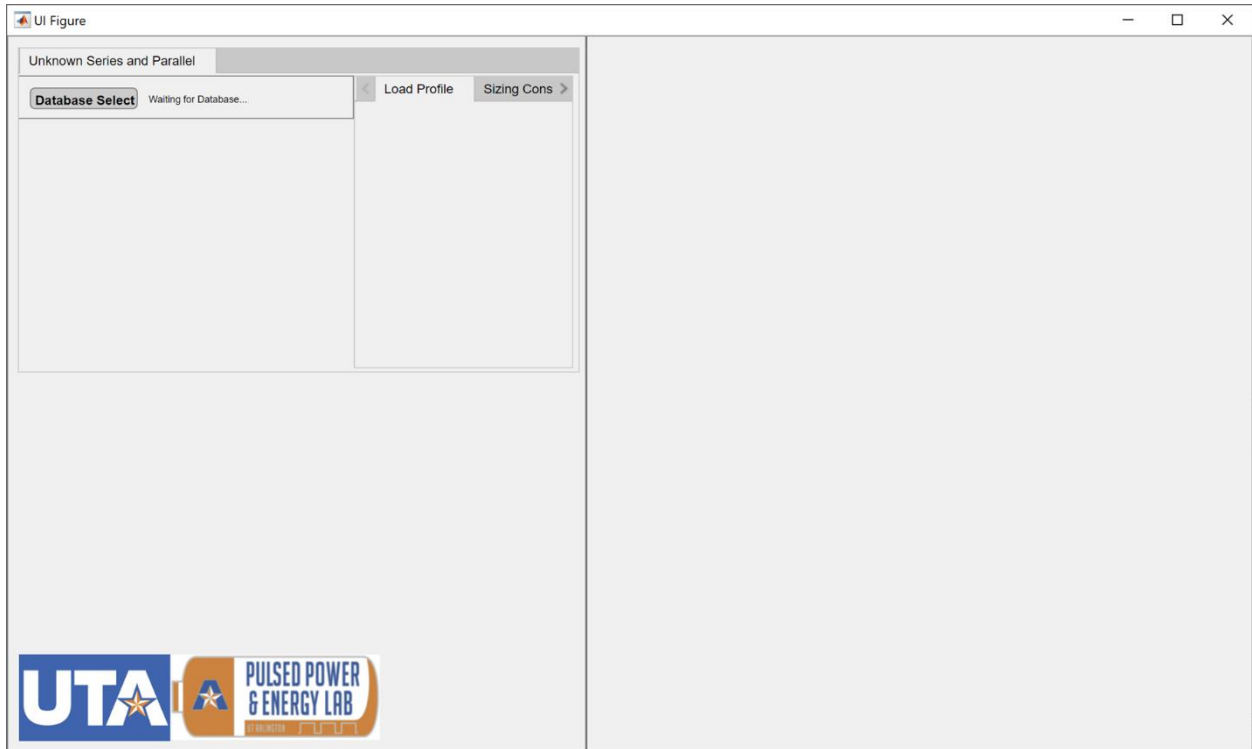
118

Figure 5.7. Sizing Tool Startup Screen. Initial screen the user is presented with upon running

the tool. Once the Database Select button is pressed and the Cell Database is loaded, additional

features become available to the user.

Figure 5.8. Sizing Tool Input Panels. Input arguments available to the user prior to sizing.

After selecting a database, multiple parameters are available to the user:

1. **User Inputs for Battery Parameters.** This section is where the core sizing parameters are entered:

   - Power Required (W)
   - Max Voltage (V)
   - Min Voltage (V)
   - Max Mass (Units Selected Below)
   - Mass Units (User Selection)
   - LWH Units (User Selection)
   - Volume Units (User Selection)

2. **Operating Temperature Slider.** This automatically rounds to the nearest 5°C, with lower temperatures negatively affecting the capacity.

   [Note] If temperature is not required, or temperature data is not available for specific cells in the database, the 'Ignore Temperature' checkbox can be selected. This will show data for cells with temperatures closest or equal to 20°C, and cells without temperature data.

3. **Load Profile and Sizing Constraints Configuration.** The first tab has load profile parameters and the second being sizing constraints. The second tab allows modification of sizing constraints, which represent portions of the nonlinear constraint function used to bound and validate Series/Parallel combinations, described later in the sizing process.

4. **Volume Constraints.** These use the previously defined units from area 1. Fudge factor represents additional 'padding' between cells, used for volume estimation and verification that the calculated series and parallel cells can actually fit within the volume constraints given the spacing between the cells.

5. **Load Profile.** This section displays a plot of the load profile using parameters from area 3. It will automatically update as parameters in area 3 are changed.

121

5.4.2 SIZING TOOL OUTPUTS

Both during and after sizing, multiple outputs are available to the user. These include a table summarizing sizing results in addition to export options for detailed results and multiple output plots. Figure 5.9 below shows the output panels visible to the user during and after sizing.
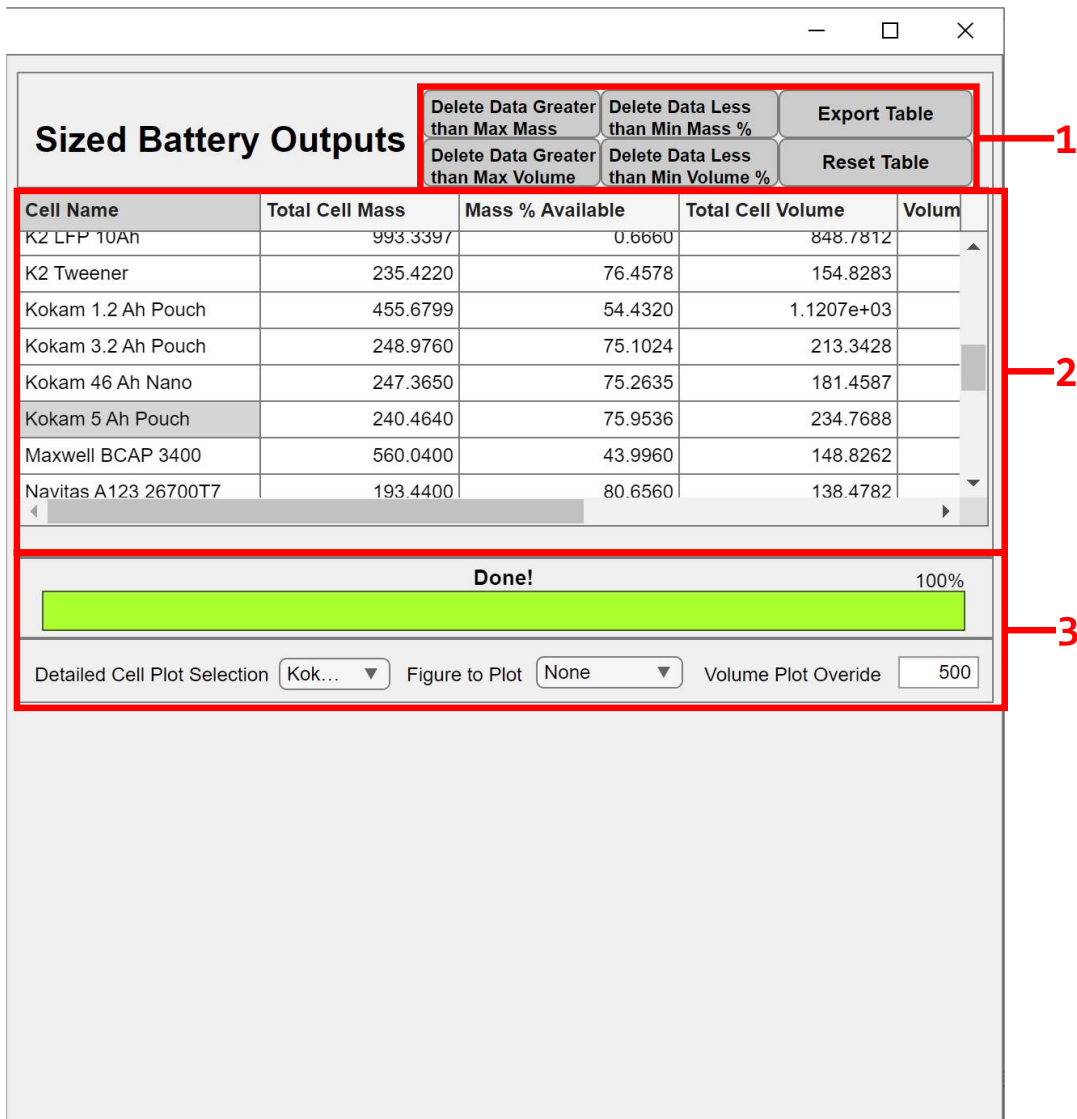

Figure 5.9. Sizing Tool Output Panels. Screen the user is presented with after sizing has completed. This screen will populate as the algorithm progresses through the database. Plots can be selected to display additional information to the user.

After sizing has completed, multiple results are available to the user:

1. **Result Table Sort/Filter Buttons.** These buttons provide basic filtering options and also allow the export of detailed sizing results in an excel sheet.

   - Power Required (W)

   - Max Voltage (V)

   - Min Voltage (V)

   - Max Mass (Units Selected Below)

   - Mass Units (User Selection)

   - LWH Units (User Selection)

   - Volume Units (User Selection)

2. **Sizing Results Table.** This table automatically populates as sizing progresses. Additional columns and comments are available in the exported table.

3. **Output Plot Selection.** This section gives a dropdown menu of cells in the database in addition to a selection of plots that can be displayed:

   - **Voltage and Current Versus Mission Time Plot**

     For a constant-power input load, this plot will display the expected voltage and current draw versus mission time.

   - **Power Versus Energy Plot**

     This plot will display the expected available energy as a function of power for the sized solution, with an additional indication of the required power and energy in relation to the available power and energy.

   - **Step-By-Step Sizing Plot**

This plot will iteratively show the optimizer searching for a global minimum by updating the plot during optimization with evaluated points and marking whether they are valid or invalid.

- **Capacity, Voltage and Discharge Current Plot**

  Using the gridfit function [13], constant-current cycling data from the Cell Database is overlaid with an interpolated fit and plotted versus capacity.

- **Estimated Volumetric Cell Locations Plot**

  This plot will run a packing algorithm dependent on cell form factor and determine the optimal orientation and spacing to fit the largest number of cells within the user defined volume constraints.

5.4.3 SIZING PROCESS

As previously mentioned, the Sizing Tool ingests the Cell Database, accepts user inputs and performs sizing using said inputs on every cell in the database. This process uses a custom optimization function to ensure that a minimum Series/Parallel combination is found that validates all constraints, in addition to a conversion function that converts constant-current data from the Cell Database to constant-power data. Figure 5.10 below shows a simplified flowchart of the sizing process. While various methods of nonlinear integer optimization were studied [14, 15], none of these performed as optimally as a custom solution.
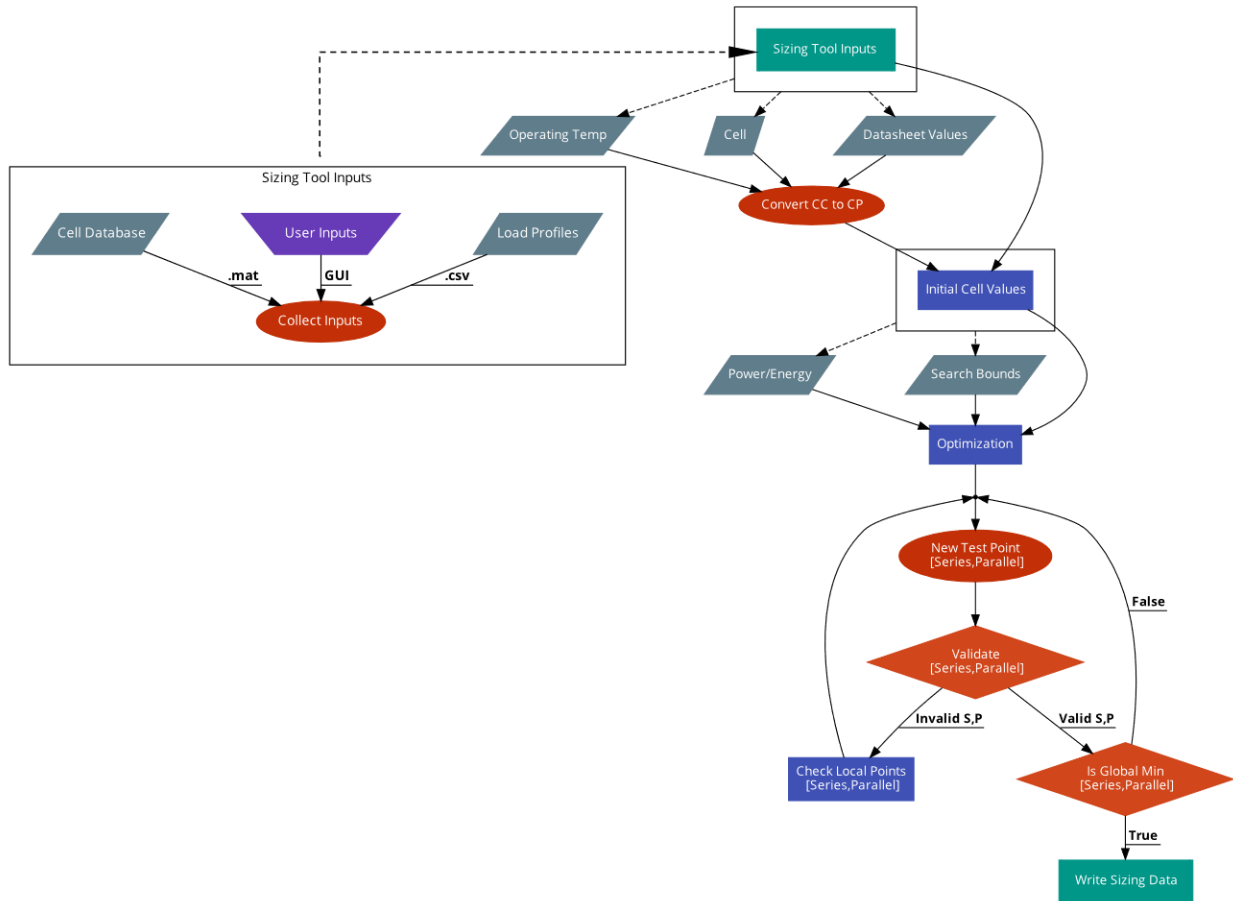
Figure 5.10. Sizing Tool Flowchart. Overview diagram of the sizing process.

To convert the constant-current data to constant-power, we must first find the value for n that minimizes the deviation of the mean of Equation (5.1) below using the method described [16].

$$V \cdot I^n \tag{5.1}$$

In the equation above, V represents all voltage curves from the Cell Database at the specified operating temperature during a constant-current discharge and I represents the constant-current corresponding to each of the constant-current discharges. Some pre-processing to cycling data must be done so the number of data points in each voltage array is the same. This can be done by down sampling or re-sampling the voltage array to be from 0 to 100% depth of discharge (DoD).

We can then further improve the calculation of n by limiting the data we perform the standard deviation on to the center region of the discharge curve, which is typically around 40% to 60% DoD. This range limitation is implemented as an index range from C_o to C_f. Equation (5.2) below shows the calculation of the mean and Equation (5.3) below shows the calculation of the standard deviation.

$$\bar{V}_i = \frac{1}{m} \cdot \sum_{j=1}^{m} V_{i,j} \cdot I_j^n \tag{5.2}$$

$$\sigma = \sqrt{\frac{1}{C_f - C_o} \cdot \sum_{i=C_o}^{C_f} (V_i - \bar{V}_i)^2} \tag{5.3}$$

Combining the above equations, we can determine the minimum value for n such that the standard deviation is minimized. This is shown below in Equation (5.4).

$$n = \min_{n \in \mathbb{R}} \sqrt{\frac{1}{C_f - C_o} \cdot \sum_{i=C_o}^{C_f} \left(V_i - \left(\frac{1}{m} \cdot \sum_{j=1}^{m} V_{i,j} \cdot I_j^n \right) \right)^2} \tag{5.4}$$

In Equations (5.2)-(5.4), m represents the number of constant-current discharge curves and $[C_o, C_f]$ represent the range of values to average over (typically between 40% and 60% of DoD). The variables i and j correspond to the specific indices of discharge curve voltage and discharge current, respectively. In this context, i denotes the index of the discharge curve voltage corresponding to the jth discharge current value. Figure 5.11 below shows an example for the optimal value of n with both discharge curves and collapsed curves.
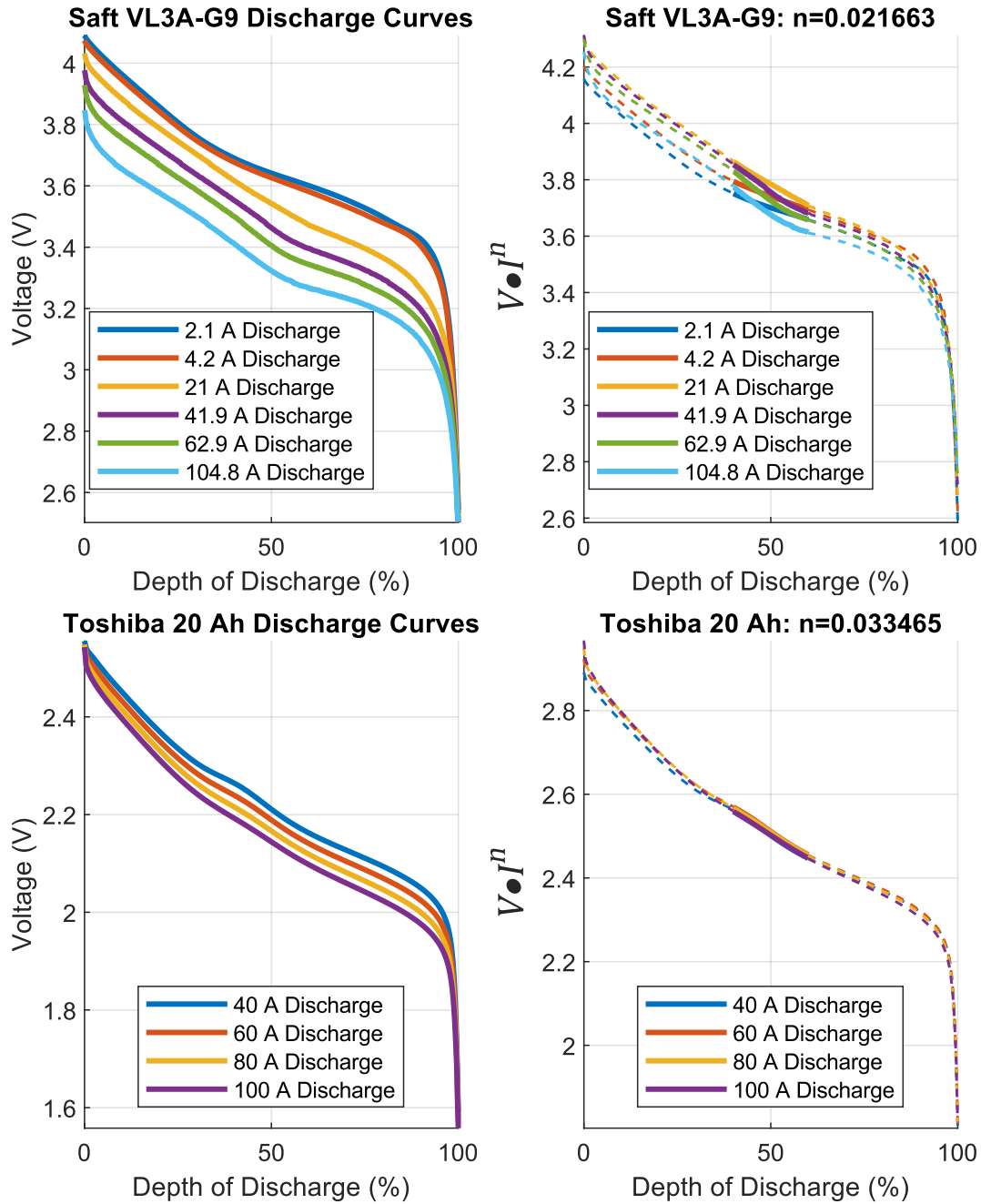
Figure 5.11. Calculation of n. (top) Discharge curves and collapsed curves after a minimized n is found for the Saft VL3A-G9 cell in the database. (bottom) Discharge curves and collapsed curves after a minimized n is found for the Toshiba 20Ah cell.

After finding the minimum value of n, we can then calculate the voltage, current and discharged capacity for a constant power P_e [1]. We must first find a fit of Equation (5.1) as a function of discharged capacity, $\widehat{D}$. The initial value for the voltage $\widehat{V}$ at a constant power discharge P_e is shown below in Equation (5.5), and is evaluated at zero discharged capacity, $\widehat{D}_1 = 0$.

$$\widehat{V}_1 = \left(\frac{I^n \cdot V(\widehat{D})_1}{P_e^n} \right)^{1/(1-n)} \tag{5.5}$$

We can then find the initial discharge current, $\hat{I}_1$, which is shown below in Equation (5.6).

$$\hat{I}_1 = \frac{P_e}{\widehat{V}_1} \tag{5.6}$$

By continually incrementing a time step Δt that is smaller than the mission time, we can effectively discharge the cell for a duration of Δt to get new values for $\widehat{V}_j$, $\hat{I}_j$ and $\widehat{D}_j$. This is repeated until $\widehat{D}_j$ reaches the expected capacity of the cell. Additional validation must be performed to make sure that the current $\hat{I}$ does not exceed the datasheet maximum current of the cell. Equation (5.7) below shows the calculation of the current, $\hat{I}_j$.

$$\hat{I}_j = \frac{P_e}{\widehat{V}_j} \tag{5.7}$$

Equation (5.8) below shows the calculation of the discharged capacity $\widehat{D}_j$, and Equation (5.9) shows the calculation of the elapsed time, t.

$$\widehat{D}_j = \hat{I}_j \cdot \Delta t + \widehat{D}_{j-1} \tag{5.8}$$

$$t_j = \sum_{m=1}^{j} \Delta t \tag{5.9}$$

This process produces curves for the voltage $\widehat{V}$, current $\hat{I}$, discharged capacity $\widehat{D}$ and elapsed time t for a requested constant power P_e. These curves are used to determine the simulated voltage and current for constraint validation. The downside to this conversion method is that the

number of elements in $\hat{V}$ and $\hat{I}$ are nondeterministic and highly dependent on the value of Δt. Values of Δt that are too small cause the size of the arrays to increase and adds computational time, so it is suggested that a method of limiting this growth is implemented by selecting a good value of Δt. Additionally, small values for P_e cause the conversion to take longer as smaller powers increase the effective capacity and the speed at which the cell is discharged, which increases the size of the output arrays.

Using the above method, we can determine a power versus energy profile for a cell by applying a range of values to P_e with the max value representing the maximum sustained power the cell can provide until it reaches datasheet limits ($Vmin_{Datasheet} \cdot Imax_{Datasheet}$). Equation (5.10) below shows the calculation of energy using previously calculated $\hat{V}$ and $\hat{D}$. Each value of E_{Cell} is calculated using one of the range of values of P_e such that the size of E_{Cell} is the same as P_e.

$$E_{Cell} = \int \hat{V} \, d\hat{D} \tag{5.10}$$

These values for energy and power are later used in the optimization algorithm to speed up the sizing process, as these values only need to be calculated once per cell. The expected energy of the cell is recalculated as a function of cell power by fitting the energy and power values calculated above. For Equation (5.10) to be valid, Equation (5.11) below also needs to be valid. If Equation (5.11) determines $P_{Cell} > (Vmin_{Datasheet} \cdot Imax_{Datasheet})$, the evaluation of the specific Series/Parallel combination is skipped and marked as an invalid configuration. If the user wants to draw more power than the max current and min voltage, this can be adjusted.

$$P_{Cell} = \frac{P_{Required}}{S \cdot P} \tag{5.11}$$

5.4.4 OPTIMIZATION ALGORITHM

Regardless of the optimization method, a constant-power load requires conversion if constant-current data is used. The evaluation of this conversion method is necessary for each distinct Series/Parallel combination. For optimizers that evaluate multiple combinations, this process can lead to an increase in calculation time. To combat this increased calculation time, efforts were made to create a custom optimization function that could handle integer inputs and multiple nonlinear constraints, while keeping a history of valid Series/Parallel combinations and dynamically reducing the search space by re-bounding when valid combinations are found.

5.4.4.1 BOUNDING POSSIBLE SERIES AND PARALLEL COMBINATIONS

To reduce the number of Series/Parallel combinations evaluated, good choices for lower and upper bounds on the possible values of Series and Parallel cells were needed. We can find an initial lower and upper bound for Series cells by dividing the voltage requirements by the voltage range of the cell, as shown below in Equation (5.12) and Equation (5.13).

$$lb(S) = \left\lceil \frac{Vmin}{Vmin_{Datasheet}} \right\rceil \tag{5.12}$$

$$ub(S) = \left\lfloor \frac{Vmax}{Vmax_{Datasheet}} \right\rfloor \tag{5.13}$$

An interesting thing to note is that the above method will not work in some scenarios, as it will identify invalid cell choices for user constraints that are not compatible with cell datasheet properties. An example of this would be a cell with $Vmax_{Cell} = 3V$ and $Vmin_{Cell} = 1V$. The user requests a battery with $Vmax = 60V$ and $Vmin = 48V$, which results in Series bounds of $ub(S) = 20$ and $lb(S) = 48$. Though the initial lower bound is larger than the upper bound, this does not immediately mean that this cell cannot be sized with these voltage constraints, but it does

require a simulation of the minimum voltage at the end of the mission. This cell would be valid if the battery is not discharged below 48 V while still supplying enough power and energy throughout the mission. Using this scenario to determine proper bounds requires a new calculation for the lower bound to account for possible scenarios where the battery may not be fully utilized.

We can get an initial lower bound by finding the min of the two methods earlier, in addition to a minimum of 1, which is shown below in Equation (5.14).

$$lb(S) = \left\lceil \min \left(\left[\frac{Vmin}{Vmin_{Datasheet}}, \frac{Vmax}{Vmax_{Datasheet}}, 1 \right] \right) \right\rceil \quad (5.14)$$

While we can determine the number of Parallel strings necessary to reduce the current draw of individual cells below their rated current, this method doesn't provide a means to establish an upper limit for the number of Parallel cells. This is because changes in individual cell current draw is linked to the constant power of each cell, which is determined by the combination of Series and Parallel cells.

We can create a lower bound for Parallel cells by determining how many parallel strings need to be added if the number of series cells is at the upper bound $ub(S)$. Equation (5.15) below shows the calculation for the number of parallel strings needed to meet the power requirement at the series upper bound, and Equation (5.16) shows the calculation for the number of parallel strings needed to meet the energy requirement. It should be noted that the individual cell power and energy in these equations represent the maximum capabilities of the cell, previously determined using Equation (5.10).

$$\rho_{Energy} = \left\lceil \frac{P_{Required}}{ub(S) \cdot \max(P_{Cell})} \right\rceil \quad (5.15)$$

$$\rho_{Energy} = \left\lceil \frac{E_{Required}}{ub(S) \cdot \max(E_{Cell})} \right\rceil \tag{5.16}$$

Combining the above equations, we can determine the lower bound for parallel cells, $lb(P)$, shown below in Equation (5.17).

$$lb(P) = \max\left(\left[\rho_{Power}, \rho_{Energy}, 1\right]\right) \tag{5.17}$$

Using a similar method, we can determine the upper bound for parallel cells by calculating the number of parallel strings needed to meet the power and energy requirements at the lower bound of series cells. Equations (5.18) and (5.19) below show the calculation of the number of strings, while Equation (5.20) shows the calculation of the upper bound of parallel cells.

$$\rho_{Power} = \left\lceil \frac{P_{Required}}{lb(S) \cdot \max(P_{Cell})} \right\rceil \tag{5.18}$$

$$\rho_{Energy} = \left\lceil \frac{E_{Required}}{lb(S) \cdot \max(E_{Cell})} \right\rceil \tag{5.19}$$

$$ub(P) = \max\left(\left[\rho_{Power}, \rho_{Energy}, lb(P), 1\right]\right) \tag{5.20}$$

5.4.4.2 EVALUATING CONSTRAINTS BEFORE OPTIMIZATION

There are nine optional constraints that the sizing tool considers, with two omitted by default. Some of these constraints need simple math to compute, while others require the constant-current to constant-power conversion.

1. Available Power can go below Required Power

2. Available Energy can go below Required Energy

3. Series · Rated Cell Vmax can go above Vmax

4. Series · Rated Cell Vmin can go below Vmin

5. Series · Simulated Cell Vmax can go above Vmax

6. Series ⋅ Simulated Cell Vmin can go below Vmin

7. Simulated Cell Vmax can go above Cell Vmax

8. Simulated Cell Vmin can go below Cell Vmin

9. Simulated Cell Imax can go above Cell Rated Imax

Constraints 1-4 can be calculated independently from the constant-current to constant-power conversion function at each new Series/Parallel combination, while constraints 5-9 need updated voltage and current due to the change in power draw in each cell for new combinations. By calculating constraints 1-4 before evaluating the constant-power conversion function, we can check if a Series/Parallel combination is valid without evaluating additional constraints and reduce the search space.

Estimated single-cell maximum constant power is found by multiplying the datasheet Vmin with the greater value between the maximum discharge current stated in the datasheet and the maximum discharge current observed in cycling data, which can be used to evaluate constraint 1. This evaluation is shown below in Equation (5.21), where values less than or equal to zero are valid constraints and where S is the number of series cells and P is the number of parallel cells.

$$P_{Required} - P_{Cell} \cdot S \cdot P \leq 0 \text{ [Constraint 1]} \tag{5.21}$$

Estimated single-cell energy is obtained by evaluating the constant-current to constant-power conversion function at P_{Cell} by integrating voltage and discharged capacity obtained from said function, shown below in Equation (5.22), where Q is in amp-hours. This can be used to evaluate constraint 2, which is shown below in Equation (5.23).

$$E_{Cell} = \int V \, dQ \tag{5.22}$$

$$E_{Required} - E_{Cell} \cdot S \cdot P \leq 0 \text{ [Constraint 2]} \tag{5.23}$$

Constraints 3 and 4 only depend on the number of series cells and the rated voltages of the cell being sized. Equation (5.24) below shows constraint 3, and Equation (5.25) shows constraint 4. It should be noted that constraint 4 may be ignored if the simulated Vmin times series cells is higher than the system Vmin. This is due to scenarios where the battery may not need to be fully discharged to complete a mission. For example, the battery voltage after the mission may be above the system Vmin and the cell datasheet Vmin, but if the battery were fully discharged it would drop below the system Vmin.

$$S \cdot Vmax_{Cell} - Vmax \leq 0 \text{ [Constraint 3]} \tag{5.24}$$

$$Vmin - S \cdot Vmin_{Cell} \leq 0 \text{ [Constraint 4]} \tag{5.25}$$

Using the constant-power conversion function, simulated values of Cell Vmax, Vmin and Imax are obtained. These values are derived by utilizing the input power calculated by dividing the required power by the total number of cells corresponding to the Series/Parallel combination being evaluated. Equations (5.26)-(5.30) below show constraints 5-9. It should be noted that constraint 7 may be disabled if the battery is not fully charged, as this scenario is also considered with constraint 2.

$$S \cdot Vmax_{Sim} - Vmax \leq 0 \text{ [Constraint 5]} \tag{5.26}$$

$$Vmin - S * Vmin_{Sim} \leq 0 \text{ [Constraint 6]} \tag{5.27}$$

$$Vmax_{Sim} - Vmax_{Datasheet} \leq 0 \text{ [Constraint 7]} \tag{5.28}$$

$$Vmin_{Datasheet} - Vmin_{Sim} \leq 0 \text{ [Constraint 8]} \tag{5.29}$$

$$Imax_{Sim} - Imax_{Datasheet} \leq 0 \text{ [Constraint 9]} \tag{5.30}$$

Figure 5.12 below emphasizes the difficulty of locating a global minimum combination of Series/Parallel cells while considering multiple constraints. The regions in yellow represent the combinations that meet all selected constraints, with this region being below all solid lines and

above all dashed lines. The area where constraints are valid varies with the cell being sized and with the input requirements, as can be seen in the comparison with the two cells. This figure was created by analyzing each possible Series/Parallel combination and finding the boundaries where constraints are valid. This is a time-consuming process for large batteries, and a justification for why optimization is necessary.
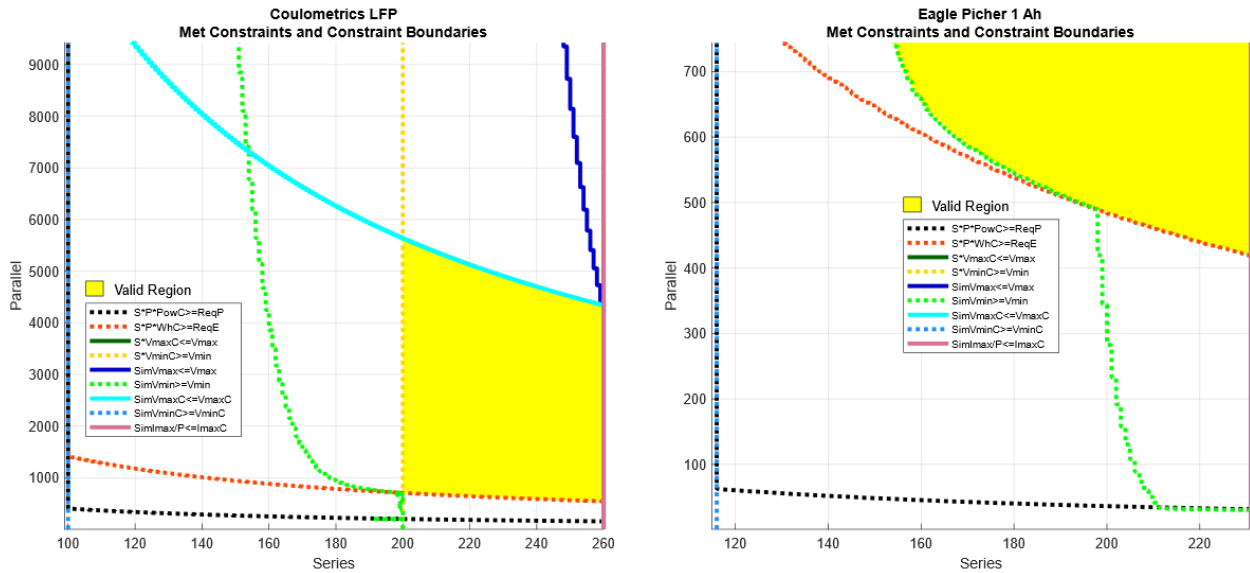

Figure 5.12. Visualization of Constraint Boundaries. (left) Constraint boundaries for the Coulometrics LFP cell, with area of valid combinations shaded in yellow. (right) Constraint boundaries for the Eagle Picher 1 Ah cell, with area of valid combinations shaded in yellow.

5.4.4.3 SEARCH SPACE REDUCTION

The search space is defined as the range of possible Series/Parallel combinations between the upper and lower bounds determined previously. By storing evaluated Series/Parallel combinations in a sparse matrix and evaluating certain parameters beforehand, the overall computation time is reduced. An initial array of Series cells (S_{bnd}) is created by taking the possible values from $lb(S)$ to $ub(S)$, which is then used to calculate the corresponding number of Parallel

cells to meet both power and energy, shown below in Equation (5.31). We then remove values of P_{bnd} that are larger than $ub(P)$ and the corresponding values of S_{bnd}. This yields initial values that meet both constraints 1 and 2

$$P_{bnd} = \left\lceil \max\left(\left[\frac{P_{Required}}{S_{bnd} \cdot P_{Cell}}, \frac{E_{Required}}{S_{bnd} \cdot E_{Cell}}\right]\right)\right\rceil \tag{5.31}$$

This array of initial combinations is evaluated to find valid combinations, if any. If no valid combinations are found in this initial array, the number of parallel cells is incremented by 1 with combinations that have parallel counts outside the upper bound being removed. We can apply additional logic to further reduce the search space during optimization. We can assume for some constraints that if the new test combination of cells is between two previously evaluated combinations, it may be skipped and assumed valid or invalid based off simple logic. For example, if the Series/Parallel combinations (220,10) and (240,10) are found to be valid, we can assume all series combinations from 221 to 239 are also valid. This process can also apply for invalid combinations and allows a further reduction in the number of unique Series/Parallel combinations evaluated. This process continues until a global minimum Series/Parallel combination is found that satisfies all constraints. Additional validation is performed around factors of the global minimum to ensure that other valid factors are not local minima, such as 20S/10P versus 10S/20P.

5.4.5 VOLUME CALCULATION

As mentioned, the user inputs a volume and weight requirement into the tool. When cells are assembled into modules, there is always some additional size and weight overhead that comes along with the interconnection hardware and clearances. Since the tool is sizing using cells only, it provides the user with the option to enter a volume and weight fudge factor that is considered to

ensure that the solution will fit the requirements with the overhead included. The values are simply entered on the front panel by the user.

Once the sizing is completed, it provides the user with a graphical rendering of the cells required to meet the objectives. The configuration is not necessarily optimized but it provides the user with a visual of how much of the volume limit is taken up by the cells alone. To ensure that cells of various shapes and sizes, whether they are cylindrical or rectangular, can fit within the user-defined volume and spacing, a custom MATLAB function was developed to use volumetric estimates of cells and 'fit' them within the given volume bounding box. There are two versions of this function: one for cells with a rectangular form factor, and one for those with a cylindrical form factor. With the complexities introduced from packing shapes with a circular base, additional checks are added to verify how many cells can fit within different orientations. Figure 5.13 shows an example of how changing the layout of cells within a bounding box can allow more to fit.
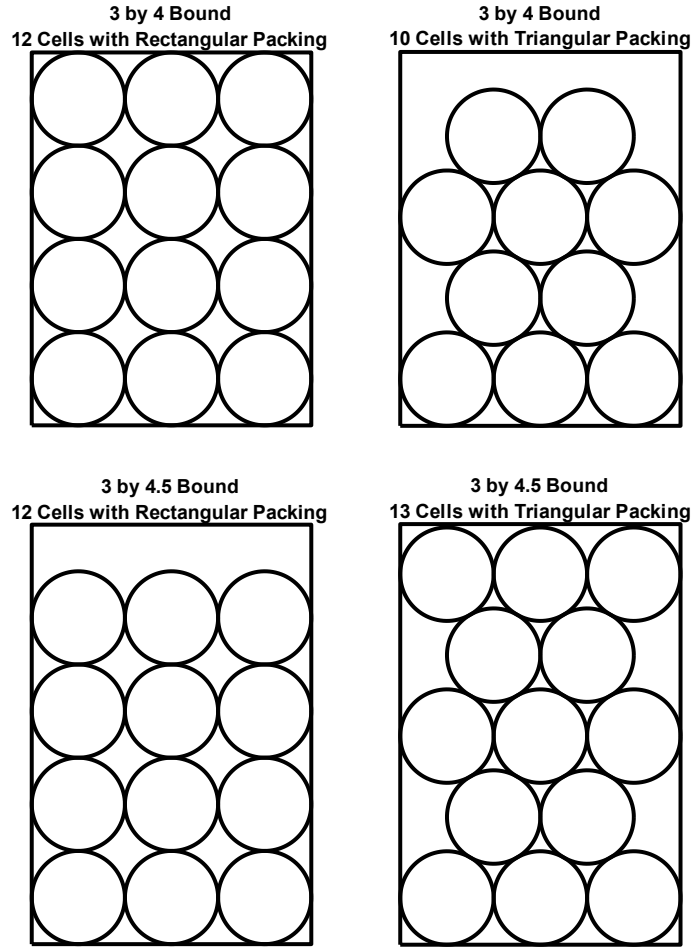
Figure 5.13. Example of Cell Volume Packing. (top) Width of 3 and length of 4. 12 cells can fit in the left bounding box but only 10 can fit in the right. (bottom) Width of 3 and length of 4.5. Only 12 cells can fit in the left bounding box but 13 can fit in the right.

A toggle option to display estimated cell locations within the bounding volume was added, but it takes decent computation time, especially for arrangements with more than 500 cells. Sample results from a problem when square form factor and cylindrical form factor cells are considered, respectively, are shown below in Figure 5.14.

Cells that can fit: 45   **Cells that can fit: 78**
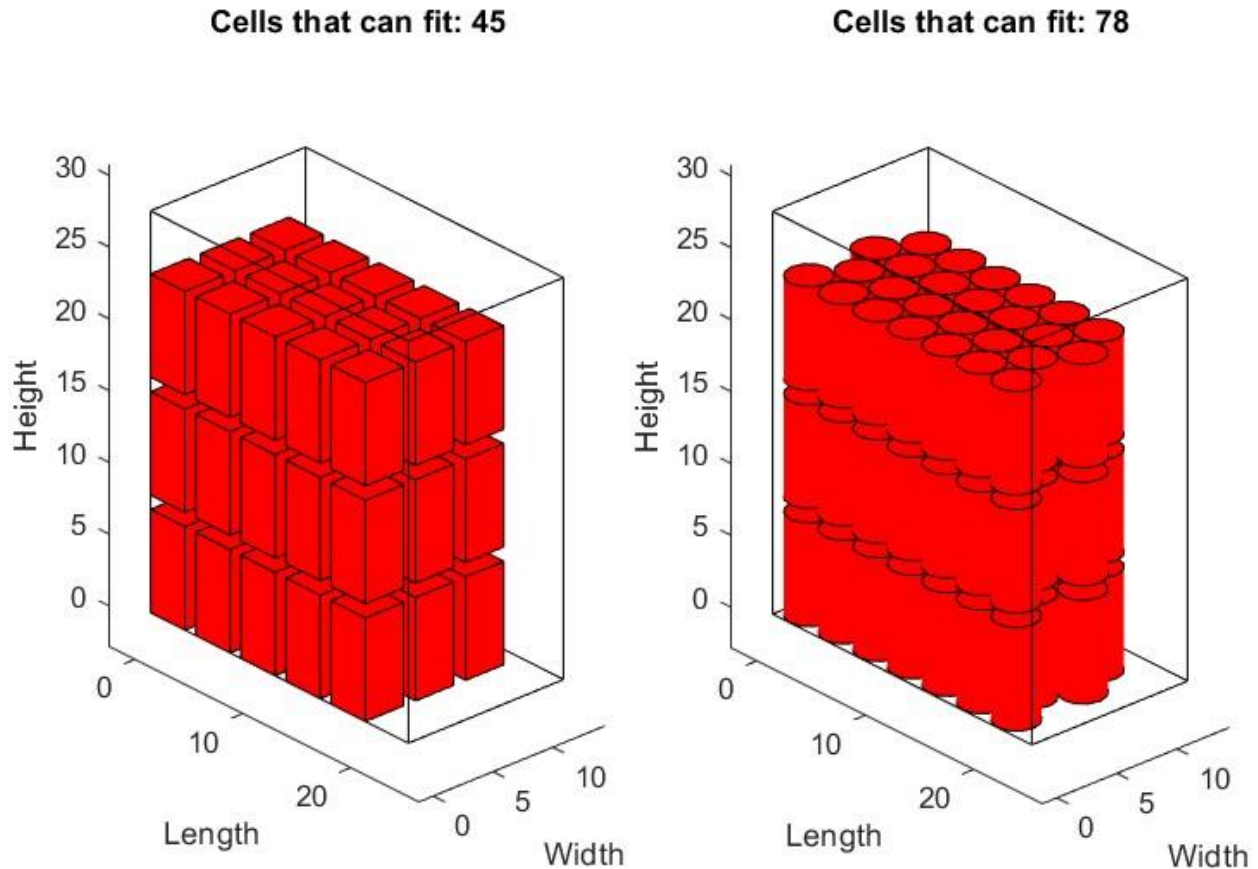
Figure 5.14. Cell Packing in the Sizing Tool. (left) Packing of cells with a rectangular form
factor. (right) Packing of cells with a cylindrical form factor.

5.5 VALIDATION OF RESULTS WITH EXISTING BATTERY MODULES

In order to validate sizing results, existing module configurations of three cells present in
the Cell Database were discharged at multiple constant powers and compared with results from
the Sizing Tool, given the same input. These results consist of a low, medium and maximum power
discharge which corresponds to the cell being validated. The resulting time taken for the constant-
power discharge to deplete the cell was used as the mission time in the Sizing Tool. The three
modules validated were as follows:

- Saft VL30 10S1P module:
  - 200W, 14250s
  - 2000W, 1350s
  - 7600W, 335s

- Toshiba 10Ah 9S1P module:
  - 200W, 4500s
  - 500W, 1750s
  - 1400W, 600s

- Ultimo 3300F Ultracapacitor 5S1P module:
  - 200W, 190s
  - 500W, 95s
  - 1000W, 47s

The voltage and current data from the constant-power discharges is then compared with the Voltage and Current versus Time plot from the Sizing Tool, and the measured capacity is compared with the simulated capacity from the sizing results.

5.5.1 SAFT VL30AFE

For the Saft VL30AFe, the results from the Sizing Tool slightly underestimated the capacity of the module. This means that there is some remaining energy past what the Sizing Tool estimated. When compared to the final capacity of the measured results for the 200 W discharge, there is only a difference of 0.257 Ah, or 0.8%. For the 2 kW discharge, the module had an additional 0.431 Ah, or 1.35% more than calculated. For the 7.6 kW discharge, the module had an additional 0.05 Ah, or 0.16% more than calculated.
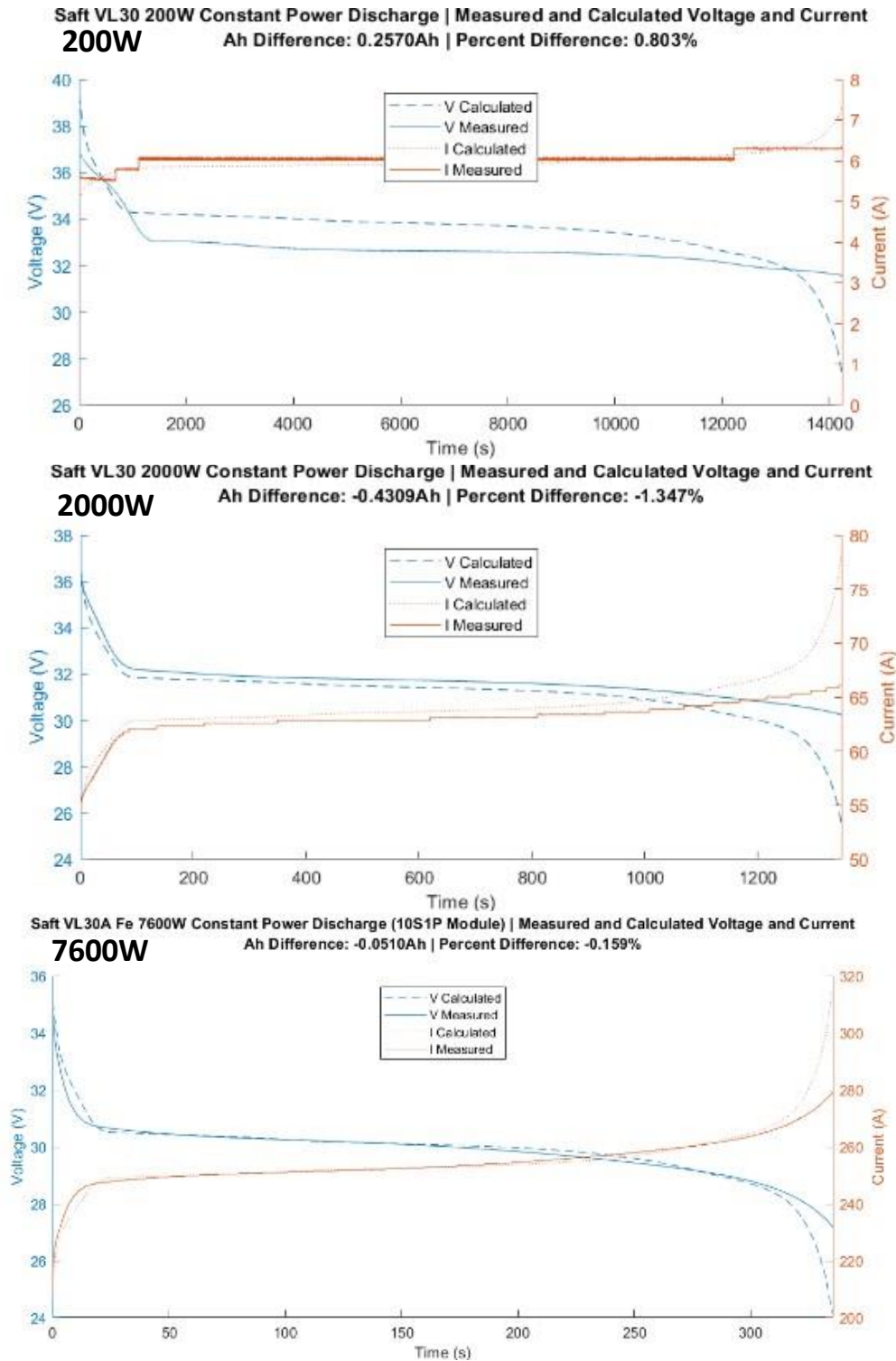
Figure 5.15. Saft VL30 Sizing Validation. (top) 200 W Constant-Power discharge for 14250 seconds with a max voltage of 39 V. (middle) 2 kW CP discharge for 1350 seconds with a max voltage of 39 V. (bottom) 7.6 kW CP discharge for 335 seconds with a max voltage of 39 V.
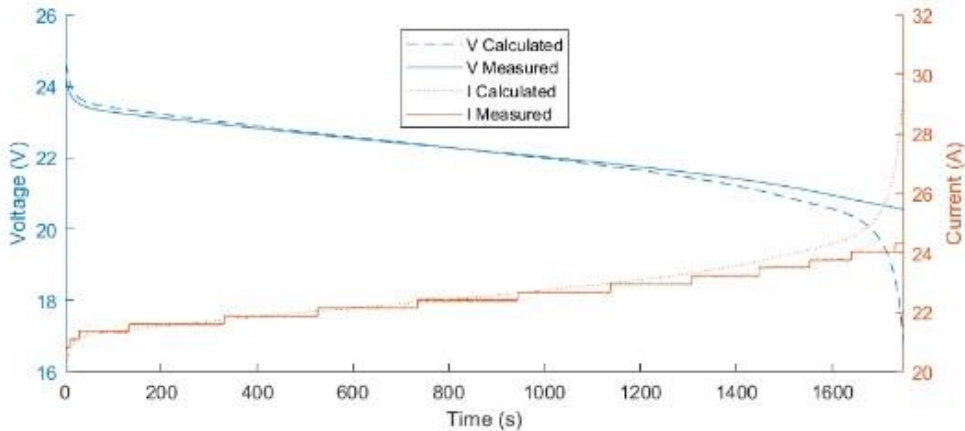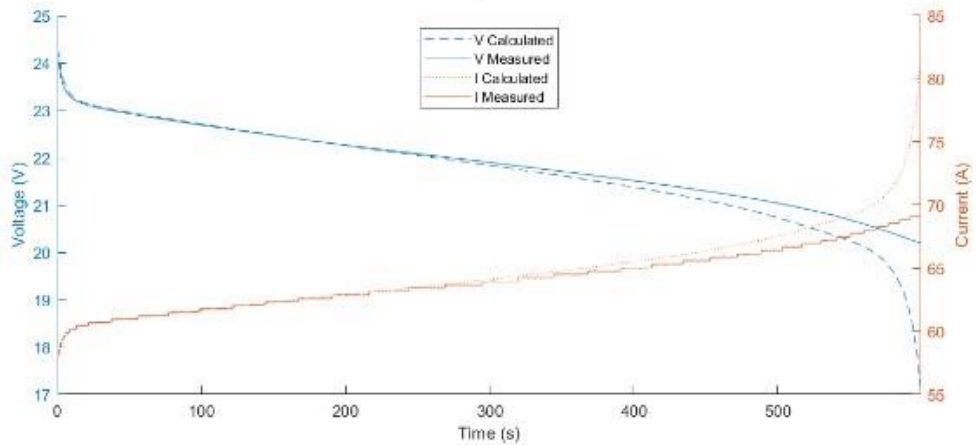
141

5.5.2 TOSHIBA 10AH MODULE

For the Toshiba module, the results from the Sizing Tool slightly underestimated the capacity of the module. This means that there is some remaining energy past what the Sizing Tool estimated. When compared to the final capacity of the measured results for the 200 W discharge, there is only a difference of 0.051 Ah, or 0.51%. For the 500 W discharge, the module had an additional 0.102 Ah, or 1.02% more than calculated. For the 1.4 kW discharge, the module had an additional 0.085 Ah, or 0.85% more than calculated.
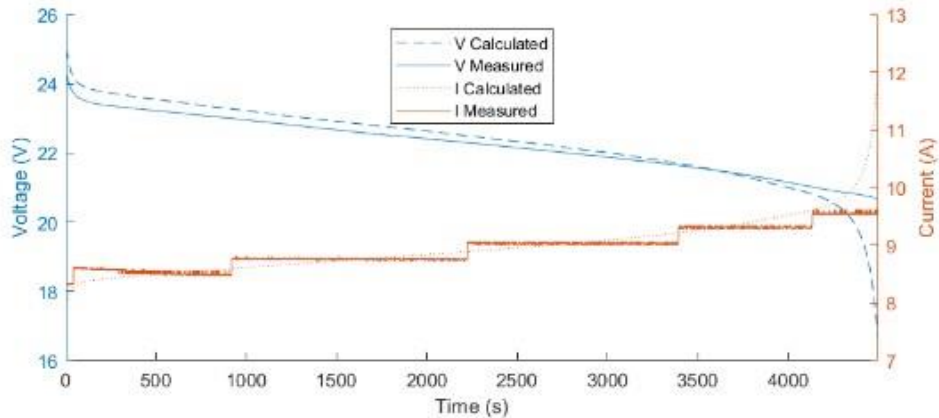
Figure 5.16. Toshiba 10Ah Sizing Validation. (top) 200 W Constant-Power discharge for 4500

seconds with a max voltage of 29 V. (middle) 500 W CP discharge for 1750 seconds with a max

voltage of 29 V. (bottom) 1.4 kW CP discharge for 600 seconds with a max voltage of 29 V.
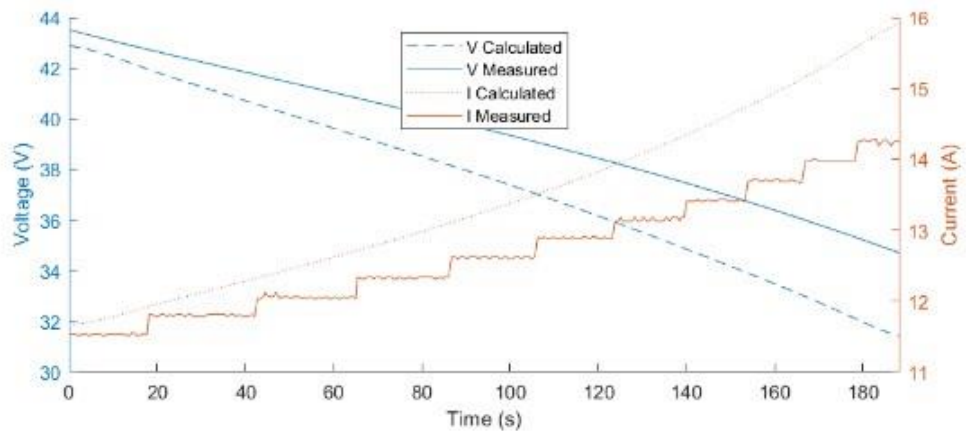
5.5.3 JM ENERGY ULTIMO 3300F ULTRACAPACITOR

For the Ultimo Ultracapacitor module, the results from the Sizing Tool slightly underestimated the capacity of the module. This means that there is some remaining energy past what the Sizing Tool estimated. When compared to the final capacity of the measured results for the 200 W discharge, there is only a difference of 0.022 Ah, or 0.86%. For the 500 W discharge, the module had an additional 0.04 Ah, or 1.581% more than calculated. For the 1 kW discharge, the module had an additional 0.042 Ah, or 1.676% more than calculated. In contrast to the LFP and LTO cells, the ultracapacitor exhibited larger differences between simulated and measured capacity. This can be attributed to the constant-current to constant-power conversion algorithm, which was not intended for ultracapacitors, though it should be noted that this underestimation is still a very good result, and modifications to the conversion algorithm may improve the estimate.
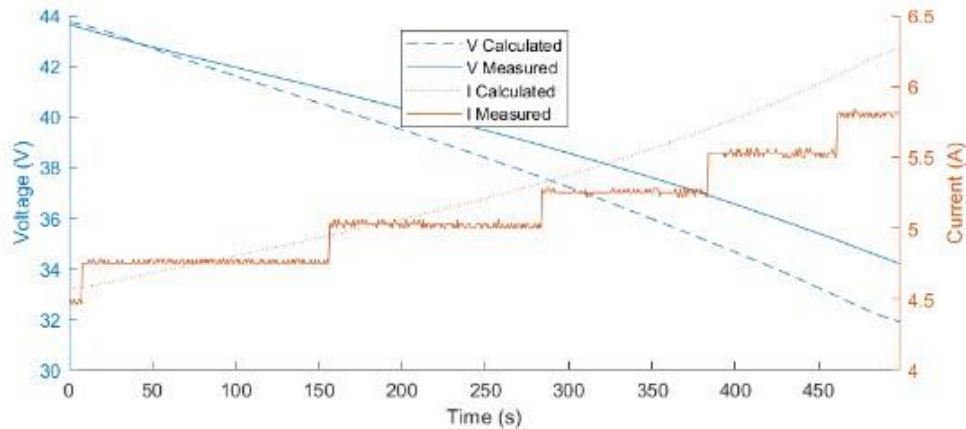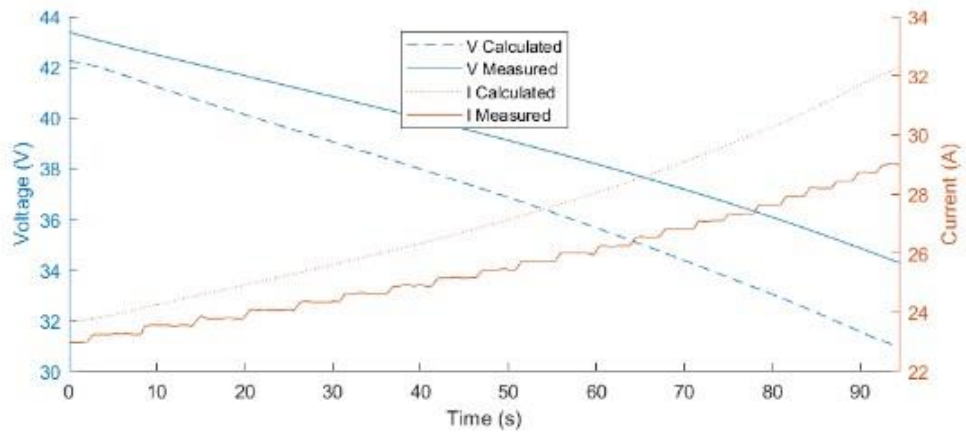
Figure 5.17. Ultimo Ultracap Sizing Validation. (top) 200 W Constant-Power discharge for

190 seconds with a max voltage of 43.8 V. (middle) 500 W CP discharge for 95 seconds with a

max voltage of 43.8 V. (bottom) 1 kW CP discharge for 47 seconds with a max voltage of 43.8 V.

5.6 SIZING TOOL LIMITATIONS

While the Sizing Tool was designed to be usable for many different chemistries and module configurations, there are some inherent limitations from the way sizing is performed and the way the Cell Database is structured. The first and most obvious limitation is the use of constant-current data to generate constant-power data instead of just using constant-power data. The reason for using constant-current data was to represent what battery manufacturers typically have available, and also to represent data that we had previously collected. It would be easier to interpolate with pre-existing constant-power data, but this would require cycling all of the cells in the database and modifying the sizing algorithm. While this may provide more accurate sizing results, the required effort to recharacterize the entire database and the accompanying modifications to the algorithm present an obstacle.

Something else that would need to be taken into consideration is the way individual cells and pre-constructed modules are categorized in the Cell Database. Single-cell parameters, especially mass and volume, can greatly underrepresent what a larger system would require with additional buswork and cooling systems. For modules that are added to the Cell Database, this protection, buswork and cooling are already factored into the overall dimensions and mass. A good illustration of this is shown in Figure 5.18 below.
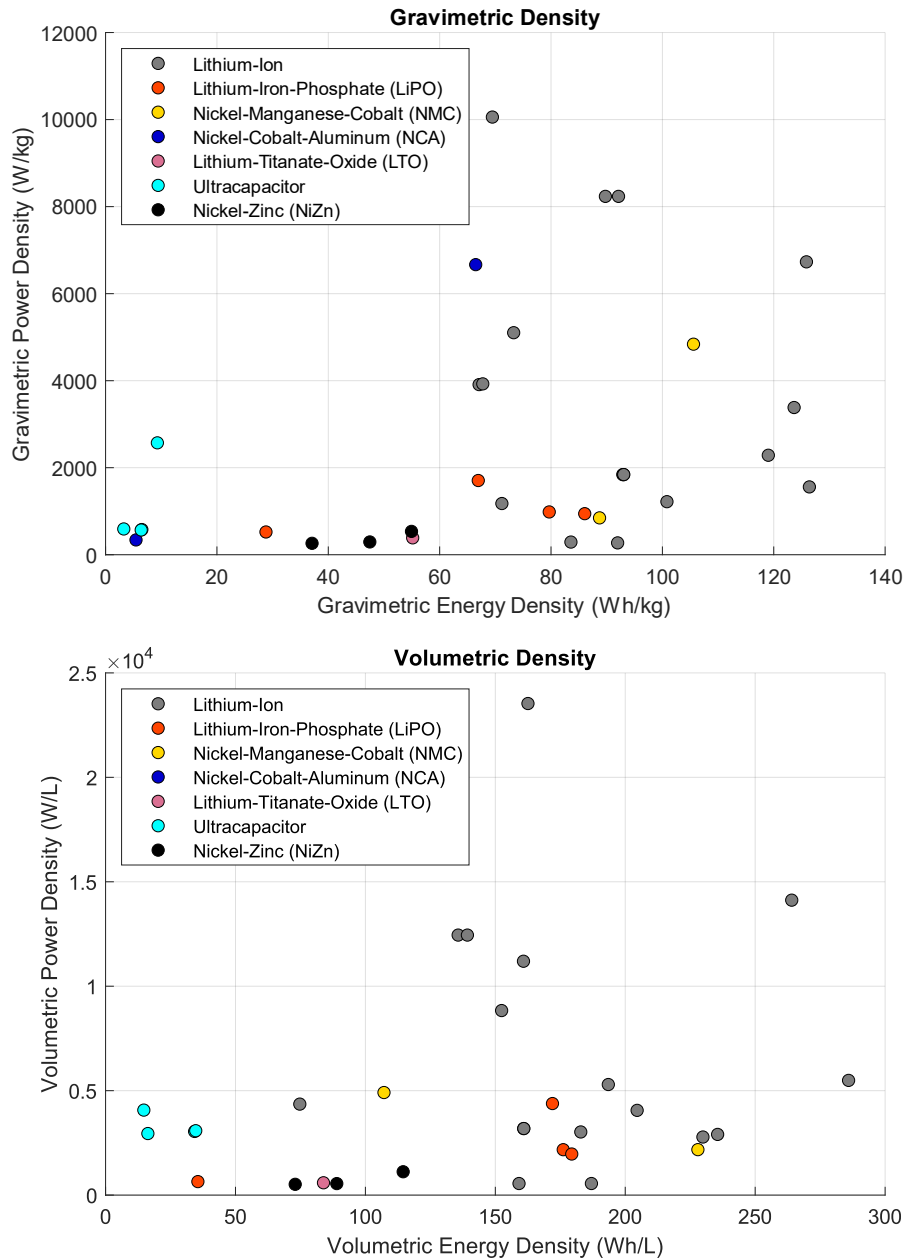
Figure 5.18. Gravimetric and Volumetric Density. (top) Gravimetric Density of all cells in the

Cell Database, grouped by chemistry. (bottom) Volumetric Density of all cells in the Cell

Database, grouped by chemistry.

This figure illustrates the Gravimetric and Volumetric densities for all cells in the Cell

Database, grouped by chemistry. Lithium-Ion greatly outperforms what is expected when

147

compared to existing power and energy densities [17]. This is due to the mass and volume of single cells within the database not accounting for additional requirements from buswork and cooling systems. This has the side effect of power and energy density for sizing results that use single cells being greatly overestimated compared to that of self-contained modules. Some studies have shown that as much as double the initial mass or volume of cells may be required for cooling and protection, but this is also highly dependent on chemistry [18]. Future improvements to the sizing tool would include a way to account for expected cooling and buswork, implemented as a per-cell fudge factor that adds additional mass and augments the cell volume.

5.7 CONCLUSION

The development of a new MATLAB based energy storage sizing tool has been presented. that utilizes empirical data to properly capture the conduction voltage and usable capacity of a cell across its full range of usable C-rates. A custom MATLAB based data import tool has also been developed to allow the user to import new empirical data into the database considered in the sizing process. As the database grows, the number of cells considered grows along with the options available to the user. Significant additional functionality is planned for this tool including a redesign of the input variables to give the user an option to enter a dynamically changing load profile rather than just a pulse width modulated input. Simulink modeling may be integrated in the future to further expand the tools capability for predicting the operational curves throughout operation for the user.

5.9 REFERENCES

[1] W. Diao, C. Kulkarni, and M. Pecht, "Development of an Informative Lithium-Ion Battery Datasheet," Energies, vol. 14, no. 17, Art. no. 17, Jan. 2021, doi: 10.3390/en14175434.

[2] A. Ostadi and M. Kazerani, "A Comparative Analysis of Optimal Sizing of Battery-Only, Ultracapacitor-Only, and Battery–Ultracapacitor Hybrid Energy Storage Systems for a City Bus," IEEE Trans. Veh. Technol., vol. 64, no. 10, pp. 4449–4460, Oct. 2015, doi: 10.1109/TVT.2014.2371912.

[3] T. M. John and S. T. Wara, "A Tutorial on the Development of a Smart Calculator to Determine the Installed Solar Requirements for Households and Small Businesses," in 2018 IEEE PES/IAS PowerAfrica, Jun. 2018, pp. 319–323. doi: 10.1109/PowerAfrica.2018.8521000.

[4] D. Wetz, "Energy Storage Devices as Prime Power Supplies for Low Energy, High Voltage Marx Generators".

[5] G. J. May, A. Davidson, and B. Monahov, "Lead batteries for utility energy storage: A review," J. Energy Storage, vol. 15, pp. 145–157, Feb. 2018, doi: 10.1016/j.est.2017.11.008.

[6] J. B. Goodenough and K.-S. Park, "The Li-Ion Rechargeable Battery: A Perspective," J. Am. Chem. Soc., vol. 135, no. 4, pp. 1167–1176, Jan. 2013, doi: 10.1021/ja3091438.

[7] J. Wen, Y. Yu, and C. Chen, "A Review on Lithium-Ion Batteries Safety Issues: Existing Problems and Possible Solutions," Mater. Express, vol. 2, no. 3, pp. 197–212, Sep. 2012, doi: 10.1166/mex.2012.1075.

[8] M. Ghiji et al., "A Review of Lithium-Ion Battery Fire Suppression," Energies, vol. 13, no. 19, Art. no. 19, Jan. 2020, doi: 10.3390/en13195117.

[9] B. Shrestha, "Capacity Fading Induced On Electrochemical Energy Storage Cells As A Result Of High C Discharge," Mar. 2014. Available:

https://rc.library.uta.edu/uta-ir/handle/10106/24130

[10] "JM Energy Introducing Lithium Ion Capacitors - New Industry Products."

https://eepower.com/new-industry-products/jm-energy-introducing-lithium-ion-capacitors/

[11] R. B. Sepe, A. Steyerl, and S. P. Bastien, "Lithium-ion supercapacitors for pulsed power applications," in 2011 IEEE Energy Conversion Congress and Exposition, Sep. 2011, pp. 1813–1818. doi: 10.1109/ECCE.2011.6064005.

[12] N. Borchers, S. Clark, B. Horstmann, K. Jayasayee, M. Juel, and P. Stevens, "Innovative zinc-based batteries," J. Power Sources, vol. 484, p. 229309, Feb. 2021, doi: 10.1016/j.jpowsour.2020.229309.

[13] J. D'Errico, "Surface Fitting using gridfit,"

https://www.mathworks.com/matlabcentral/fileexchange/8998-surface-fitting-using-gridfit

[14] "Numerical Methods in Engineering and Science: C, C++, and MATLAB."

https://www.mathworks.com/academia/books/numerical-methods-in-engineering-and-science-grewal.html

[15] R. Hemmecke, M. Köppe, J. Lee, and R. Weismantel, "Nonlinear Integer Programming," 2010, pp. 561–618. doi: 10.1007/978-3-540-68279-0_15.

[16] L. W. Traub, "Calculation of Constant Power Lithium Battery Discharge Curves," Batteries, vol. 2, no. 2, Art. no. 2, Jun. 2016, doi: 10.3390/batteries2020017.

[17] A. A. Kebede, T. Kalogiannis, J. Van Mierlo, and M. Berecibar, "A comprehensive review of stationary energy storage devices for large scale renewable energy sources grid integration," Renew. Sustain. Energy Rev., vol. 159, p. 112213, May 2022

doi: 10.1016/j.rser.2022.112213.

[18] C. L. Williams, M. J. Martin, D. A. Wetz, K. Mckinzie, and J. M. Heinzel, "High rate comparison of lithium-ion, valve regulated lead acid, and nickel metal hydride batteries for use in pulsed power applications," in 2015 IEEE Pulsed Power Conference (PPC), May 2015, pp. 1–6. doi: 10.1109/PPC.2015.7297026.

CHAPTER 6: CONCLUSION

6.1 FIBER OPTIC SENSING AND INSTRUMENTATION

Lithium-ion batteries are everywhere, and their use is only predicted to grow in the future. As batteries are constructed with more cells interconnected in series/parallel to meet the growing power and energy demands, the need for reliable monitoring and safety methods increases as well. Historically only a few strategic thermal measurements are made, and the assumption is that those will be sufficient but that may not always be the case. There are limitations to how many thermocouples and thermistors can be effectively introduced into large cell arrays. In the work presented here, a Luna Optical Distributed Sensor Interrogator (ODiSI) that utilizes high density fiber optic sensors (FOSs) has been shown to be very effective at monitoring either the thermal or strain properties of individual cells within multiple-cell arrays during normal and abnormal operating conditions. Demonstrations have shown that the dielectrically insulated fiber is effective for monitoring cells within batteries operating at voltages more than 1 kVDC. Custom data acquisition software has been developed using the LabVIEW programming language to collect data from the Luna ODiSI and relay that to either the BMS or the real-time controller over the entire system. Though the ODiSI is an expensive measurement solution, it offers unique capability that is difficult, if not impossible for other diagnostic techniques to match. This is certain to find broader application and it hoped that this dissertation will serve as a springboard for its employment in the energy storage industry.

6.2 ENERGY STORAGE SIZING TOOL

The power and energy density of batteries is growing every day. The applications and use cases they will find their way into are limitless and in applications where size and weight are

152

crucial, it is important to be able to properly size batteries such that they are not larger than they must be but also not so small as to leave a user without the power they need. Manufacturer's datasheets lack the full suite of information needed to properly size batteries, especially under high rates. This work has demonstrated the design of a energy storage sizing tool that employs empirically collected data to ensure that the available power and energy is properly calculated. The tool has been developed using the MATLAB programming environment and has a data import tool that allows a user to seamlessly increase the database that the tool considers. It has been demonstrated and validated against several different use cases.

Efforts to expand the utility of the energy storage sizing tool are planned. First, the incorporation of dynamic load profiles would expand the tool's capability by replicating real-world operational loads. Additional profile analysis could be conducted using probability to determine an effective energy storage that is not oversized due to transient events. Additionally, the integration of Simulink modeling to further augment the tool's capabilities would improve power and energy estimation for the various chemistries in the database. By implementing empirical data in a Simulink environment, this will allow the tool to better simulate battery discharge characteristics. In the future, kinetic energy storage solutions, such as flywheel energy storage (FES) may be introduced into the sizing tool.

COMPILATION OF REFERENCES

A.A. Andreev, A.G. Vozmilov, V.A. Kalmakov, "Simulation of lithium battery operation under severe temperature conditions." *Procedia Engineering*, 129 (2015).

A. A. Kebede, T. Kalogiannis, J. Van Mierlo, and M. Berecibar, "A comprehensive review of stationary energy storage devices for large scale renewable energy sources grid integration," Renew. Sustain. Energy Rev., vol. 159, p. 112213, May 2022,

doi: 10.1016/j.rser.2022.112213.

A. Ostadi and M. Kazerani, "A Comparative Analysis of Optimal Sizing of Battery-Only, Ultracapacitor-Only, and Battery–Ultracapacitor Hybrid Energy Storage Systems for a City Bus," IEEE Trans. Veh. Technol., vol. 64, no. 10, pp. 4449–4460, Oct. 2015,

doi: 10.1109/TVT.2014.2371912.

Arhant, M., Meek, N., Penumadu, D., Davies, P., Garg, N. "Residual Strains using Integrated Continuous Fiber Optic Sensing in Thermoplastic Composites and Structural Health Monitoring." Experimental Mechanics, pp. 167-176, September 14, 2017.

B. Gu, M. Yin, A.P. Zhang, J. Qian, S. He, "Optical fiber relative humidity sensor based on FBG incorporated thin-core fiber modal interferometer." *Optics Express*, 19 (2011).

B. Shrestha, "Capacity Fading Induced On Electrochemical Energy Storage Cells As A Result Of High C Discharge," Mar. 2014, Available: https://rc.library.uta.edu/uta-ir/handle/10106/24130

C. Campestrini, T. Heil, S. Kosch, A. Jossen, "A comparative study and review of different Kalman filters by applying an enhanced validation method." *Journal of Energy Storage*, 8 (2016).

C. L. Williams, M. J. Martin, D. A. Wetz, K. Mckinzie, and J. M. Heinzel, "High rate comparison of lithium-ion, valve regulated lead acid, and nickel metal hydride batteries for use in pulsed power applications," in 2015 IEEE Pulsed Power Conference (PPC), May 2015, pp. 1–6. doi: 10.1109/PPC.2015.7297026.

C-Y. Choe, W-S. Jung, J-W. Byeon, "Damage Evaluation in Lithium Cobalt Oxide/Carbon Electrodes of Secondary Battery by Acoustic Emission Monitoring." *Materials Transactions*, 56 (2015).

D. Bernardi, E. Pawlikowski, J. Newman, "A General Energy Balance for Battery Systems." *Journal of the Electrochemical Society*, 132 (1985).

Duncan, R., Childers, B., Gifford, D., Petit, D., Hickson, A., Jackson, A., Duke, J., Brown, T., "Use of a Fiber-Optic Distributed Sensing System for Nondestructive testing of Aerospace Structures," *Materials Evaluation* 61, 838 (2003).

D. Wetz, "Energy Storage Devices as Prime Power Supplies for Low Energy, High Voltage Marx Generators".

E. Vergori, Y. Yu, "Monitoring of Li-ion cells with distributed fibre optic sensors." *Procedia Structural Integrity*, 24 (2019).

G-H. Kim, A. Pesaran, "Battery Thermal Management Design Modeling." *The World Electric Vehicle Association Journal*, 1 (2007).

G. J. May, A. Davidson, and B. Monahov, "Lead batteries for utility energy storage: A review," J. Energy Storage, vol. 15, pp. 145–157, Feb. 2018, doi: 10.1016/j.est.2017.11.008.

H. L. Atchison, Z. R. Bailey, D. A. Wetz, M. Davis, and J. M. Heinzel, "Fiber Optic Based Thermal and Strain Sensing of Lithium-Ion Batteries at the Individual Cell Level," J. Electrochem. Soc., vol. 168, no. 4, p. 040535, Apr. 2021, doi: 10.1149/1945-7111/abf7e4.

H. Atchison, Z. Bailey, D. Wetz, M. Davis, and J. Heinzel, "Fiber Optic Based Thermal Sensing of Lithium-Ion Cells at the Module Level," J. Electrochem. Soc., vol. 169, no. 9, p. 097503, Sep. 2022, doi: 10.1149/1945-7111/ac8bab.

H. Atchison, Z. Bailey, D. Wetz, M. Davis, and J. Heinzel, "Thermal Monitoring of Series and Parallel Connected Lithium-ion Battery Modules Using Fiber Optic Sensors," ECS Sens. Plus, vol. 1, no. 2, p. 025401, Jun. 2022, doi: 10.1149/2754-2726/ac7abd.

H. Popp, M. Koller, M. Jahn, A. Bergmann, "Mechanical methods for state determination of Lithium-Ion secondary batteries: A review." *Journal of Energy Storage*, 32 (2020).

J. B. Goodenough and K.-S. Park, "The Li-Ion Rechargeable Battery: A Perspective," J. Am. Chem. Soc., vol. 135, no. 4, pp. 1167–1176, Jan. 2013, doi: 10.1021/ja3091438.

J. D'Errico, "Surface Fitting using gridfit,"

https://www.mathworks.com/matlabcentral/fileexchange/8998-surface-fitting-using-gridfit

"JM Energy Introducing Lithium Ion Capacitors - New Industry Products."

https://eepower.com/new-industry-products/jm-energy-introducing-lithium-ion-capacitors/

J. Meyer, A. Nedjalkov, A. Doering, M. Angelmahr, W. Schade, "Fiber optical sensors for enhanced battery safety." *Proceedings of SPIE, Fiber Optic Sensors and Applications XII*, 2015.

J. Wen, Y. Yu, and C. Chen, "A Review on Lithium-Ion Batteries Safety Issues: Existing Problems and Possible Solutions," Mater. Express, vol. 2, no. 3, pp. 197–212, Sep. 2012, doi: 10.1166/mex.2012.1075.

J. Yi, U.S. Kim, C.B. Shin, T. Han, S. Park, "Modeling the temperature dependence of the discharge behavior of a lithium-ion battery in low environmental temperature." *Journal of Power Sources*, 244 (2013).

K. Feng, J. Cui, Y. Jin, X. Sun, D. Jiang, H. Dang, Y. Niu, J. Tan, "Enhancement of the Performance and Data Processing Rate of an Optical Frequency Domain Reflectometer Distributed Sensing System Using a Limited Swept Wavelength Range." *Sensors*, 18 (2018).

Kreger, S. T., Gifford, D. K., Froggatt, M. E., Soller, B. J., & Wolfe, M. S., "High resolution distributed strain or temperature measurements in single-and multi-mode fiber using swept-wavelength interferometry". In Optical Fiber Sensors p. ThE42 (2006).

Kreger, S., Gifford, D., Froggatt, M., Sang, A., Duncan, R., et al. "High-resolution extended distance distributed fiber-optic sensing using Rayleigh backscatter." *Proceedings of SPIE*, pp. 1-12, April 10, 2007.

Kreger, S., Rahim, N., Garg, N., Klute, S., Metrey, D., et al. "Optical frequency domain reflectometry: principles and applications in fiber optic sensing." *Proceedings of SPIE*, pp. 83-84. May 12, 2016.

L. Palmieri, L. Schenato, "Distributed Optical Fiber Sensing Based on Rayleigh Scattering." *The Open Optics Journal*, 7 (2013).

L.W. Sommer, P. Kiesel, A. Ganguli, A. Lochbaum, B. Saha, J. Schwartz, C-J. Bae, M. Alamgir, A. Raghavan, "Fast and slow ion diffusion processes in lithium ion pouch cells during cycling observed with fiber optic strain sensors." *Journal of Power Sources*, 296 (2015).

L. W. Traub, "Calculation of Constant Power Lithium Battery Discharge Curves," Batteries, vol. 2, no. 2, Art. no. 2, Jun. 2016, doi: 10.3390/batteries2020017.

M. Arhant, N. Meek, D. Penumadu, P. Davies, N. Garg, "Residual Strains using Integrated Continuous Fiber Optic Sensing in Thermoplastic Composites and Structural Health Monitoring." *Experimental Mechanics*, pp. 167-176, September 14, 2017.

M. Ghiji et al., "A Review of Lithium-Ion Battery Fire Suppression," Energies, vol. 13, no. 19, Art. no. 19, Jan. 2020, doi: 10.3390/en13195117.

M. Nascimento, S. Novais, M.S. Ding, M.S. Ferreira, S. Koch, S. Passerini, J.L. Pinto. "Internal strain and temperature discrimination with optical fiber hybrid sensors in Li-ion batteries." *J. Power Sources*, 410-411 (2019) 1-9.

M. Nascimento, M.S. Ferreira, J.L. Pinto, "Real time thermal monitoring of lithium batteries with fiber sensors and thermocouples: A comparative study." *Measurement*, 111 (2017).

M. Nascimento, M.S. Ferreira, J.L. Pinto, "Temperature fiber sensing of Li-ion batteries under different environmental and operating conditions." *Applied Thermal Engineering*, 149 (2019).

M. Sheikh, A. Elmarakbi, S. Rehman, "A combined experimental and simulation approach for short circuit prediction of 18650 lithium-ion battery under mechanical abuse conditions." *Journal of Energy Storage*, 32 (2020).

M. Yildiz, H. Karakoc, I. Dincer, "Modeling and validation of temperature changes in a pouch lithium-ion battery at various discharge rates." *International Communications in Heat and Mass Transfer*, 75 (2016).

N.A.A. Rahim, M.A. Davis, L. Routhier, B. Chang, J. Chevalier, J.J. Bos, S.T. Kreger, E.E. Sanborn. "Accuracy and Survivability of Distributed Fiber Optic Temperature Sensors." *AIAA SciTech Forum*, 53rd AIAA Aerospace Sciences Meeting, January 5-9, 2015.

N. Borchers, S. Clark, B. Horstmann, K. Jayasayee, M. Juel, and P. Stevens, "Innovative zinc-based batteries," J. Power Sources, vol. 484, p. 229309, Feb. 2021, doi: 10.1016/j.jpowsour.2020.229309.

"Numerical Methods in Engineering and Science: C, C++, and MATLAB." https://www.mathworks.com/academia/books/numerical-methods-in-engineering-and-science-grewal.html

Osgar John Ohanian III, Naman Garg, and Matthew A. Castellucci "Integrated fiber optic structural health sensors for inflatable space habitats", Proc. SPIE 10172, A Tribute Conference Honoring Daniel Inman, 101720B (10 April 2017); https://doi.org/10.1117/12.2260106.

Pedrazzani, J.R., Klute, S. M., Gifford, D. K., Sang, A. K., and Froggatt, M. K., "Embedded and surface mounted fiber optic sensors detect manufacturing defects and accumulated damage as a wind turbine blade is cycled to failure," Proc. 2012 SAMPE Technical Conference, Baltimore, MD, May 21-24, (2012).

P.J. Bugrynieca, J.N. Davidson, D.J. Cumming, et al., Pursuing safer batteries: thermal abuse of LiFePO$_4$ cells, J. Power Sources 414 (2019) 557-568.

P. Wang, X. Zhang, L. Yang, X. Zhang, M. Yang, H. Chen, D. Fang, "Real-time monitoring of internal temperature evolution of the lithium-ion coin cell battery during the charge and discharge process." *Extreme Mechanics Letters*, 9 (2016).

R. B. Sepe, A. Steyerl, and S. P. Bastien, "Lithium-ion supercapacitors for pulsed power applications," in 2011 IEEE Energy Conversion Congress and Exposition, Sep. 2011, pp. 1813–1818. doi: 10.1109/ECCE.2011.6064005.

R. Fitzgerald, V. Karanassios, "The Internet of Things (IoT) for a Smartphone-enabled Optical Spectrometer and its use On-site and (potentially) for Industry 4.0." *Proceedings of SPIE, Next-Generation Spectroscopic Technologies XI*, 2018.

R. Hemmecke, M. Köppe, J. Lee, and R. Weismantel, "Nonlinear Integer Programming," 2010, pp. 561–618. doi: 10.1007/978-3-540-68279-0_15.

S. Novais, M. Nascimento, L. Grande, M.F. Domingues, P. Antunes, N. Alberto, C. Leitao, R. Oliveira, S. Koch, G.T. Kim, S. Passerini, J. Pinto, "Internal and External Temperature Monitoring of a Li-Ion Battery with Fiber Bragg Grating Sensors." *Sensors*, 16 (2016).

S. Panchal, I. Dincer, M. Agelin-Chaab, R. Fraser, M. Fowler, "Experimental temperature distributions in a prismatic lithium-ion battery at varying conditions." *International Communications in Heat and Mass Transfer*, 71 (2016).

Stephen T. Kreger, Nur Aida Abdul Rahim, Naman Garg, Sandra M. Klute, Daniel R. Metrey, Noah Beaty, James W. Jeans, Robert Gamber, "Optical frequency domain reflectometry: principles and applications in fiber optic sensing," Proc. SPIE 9852, Fiber Optic Sensors and Applications XIII, 98520T (12 May 2016); https://doi.org/10.1117/12.2229057.

S.Young, D. Penumadu, D. Foster, H. Maeser, B. Balijepalli, J. Reese, D. Bank, J. Dahl, P. Blanchard, "Smart Adhesive Joint with High-Definition Fiber-Optic Sensing for Automotive Applications." *Sensors*, 20 (2020).

S. Zhang, X. Guo, X. Zhang, "An improved adaptive unscented kalman filtering for state of charge online estimation of lithium-ion battery." *Journal of Energy Storage*, 32 (2020).

T. Bandhauer, S. Garimella, T.F. Fuller, "A Critical Review of Thermal Issues in Lithium-Ion Batteries." *Journal of The Electrochemical Society*, 158 (2011).

T. M. John and S. T. Wara, "A Tutorial on the Development of a Smart Calculator to Determine the Installed Solar Requirements for Households and Small Businesses," in 2018 IEEE PES/IAS PowerAfrica, Jun. 2018, pp. 319–323. doi: 10.1109/PowerAfrica.2018.8521000.

T. Matsuo, M. Uchida, H. Cho, "Development of Acoustic Emission Clustering Method to Detect Degradation of Lithium Ion Batteries." *Journal of Solid Mechanics and Materials Engineering*, 5 (2011).

V. Raman, M. Drissi-Habti, P. Limje, A. Khadour. "Finber SHM-Coverage of Inter-Plies and Bondings in Smart Composite by Dual Sinusoidal Placed Distributed Optical Fiber Sensors." *Sensors*, 742 (2019).

W. Diao, C. Kulkarni, and M. Pecht, "Development of an Informative Lithium-Ion Battery Datasheet," Energies, vol. 14, no. 17, Art. no. 17, Jan. 2021, doi: 10.3390/en14175434.

Y. Gang, C. Leitao, Y. Li, J. Pinto, X. Jiang. "Real-time temperature measurement with fiber Bragg sensors in lithium batteries for safety usage." *Measurement*, pp. 3166-3172. May 14, 2013.

Y. Nishi, Lithium-ion secondary batteries; past 10 years and the future, J. Power Sources 100 (2001) 101-106.

Y. Xu, M. Hu, A. Zhou, Y. Li, S. Li, C. Fu, C. Gong, "State of charge estimation for lithium-ion batteries based on adaptive dual Kalman filter." *Applied Mathematical Modelling*, 77 (2020).

Z. Zhang, P. Ramadass, W. Fang, "Safety of Lithium-ion Batteries." *Lithium-Ion Batteries: Advances and Applications*, 2014.

APPENDIX

COPYRIGHT APPROVAL FOR MANUSCRIPT 1

COPYRIGHT APPROVAL FOR MANUSCRIPT 2

COPYRIGHT APPROVAL FOR MANUSCRIPT 3